Aus der Klinik und Poliklinik für Anästhesiologie und Intensivtherapie
Direktorin: Frau Prof. Dr. med. Thea Koch

# Assessment of the distribution of aeration, perfusion, and inflammation using PET/CT in an animal model of acute lung injury

D i s s e r t a t i o n s s c h r i f t

zur Erlangung des akademischen Grades

Doctor rerum medicinalium (Dr. rer. medic.)

vorgelegt

der Medizinischen Fakultät Carl Gustav Carus

der Technischen Universität Dresden

von

Dipl.-Ing. Anja Braune

aus Dresden

Dresden, 2017

1. Gutachter: Univ.-Prof. Dr.med.habil. Marcelo Gama de Abreu

2. Gutachter: Prof. Dr. med. Jörg Kotzerke

Tag der mündlichen Prüfung: 14.09.2017

PD Dr. med. Martin Kolditz

Vorsitzender der Promotionskommission

# Acknowledgement

I would like to express my sincere gratitude to the several people who have helped and supported me in carrying out this research.

First and foremost, I would like to express my gratitude to my supervisor, Univ.-Prof. Dr. med. habil. Marcelo Gama de Abreu, for giving me the opportunity to work in his research group and for supporting me in every possible way over the past several years. His help, unwavering support, and encouragement were fundamental for this research work, and for important professional and personal achievements during the last years.

I also would like to thank Prof. Dr. med. Thea Koch for giving me the opportunity to work as research associate at the University Hospital Carl Gustav Carus at the Technische Universität Dresden.

Furthermore, I would like to thank all the members of the Pulmonary Engineering Group for sharing with me their knowledge, experience, and ideas, for their valuable medical explanations and discussions as well as for making the group a stimulating and promoting working environment. I am very grateful for the opportunity to have worked with such a gifted and congenial group of people.

Also, I would like to thank Prof. Dr. med. Jörg Kotzerke and the employees of the Nuclear Medicine Department of the University Hospital Carl Gustav Carus at the Technische Universität Dresden for sharing their knowledge with me, the permanent readiness to help, unlimited support, and stimulating discussions.

Lastly and most importantly, I would like to thank my family, especially my parents, and Kai, for the unending support, interest in my work, continuous motivation, and encouragement.

# Table of Contents

# List of Abbreviations

| | |
|---|---|
| ACCT | attenuation corrected computed tomography |
| ARDS | acute respiratory distress syndrome |
| BIPAP/APRV | biphasic positive airway pressure/ airway pressure release ventilation |
| BIPAP/APRV 0% | BIPAP/APRV superposed with 0 % of spontaneous breathing |
| BIPAP/APRV >60% | BIPAP/APRV superposed with >60 % of spontaneous breathing |
| $C_{PET}$ | activity of $^{18}$F-FDG in a region of interest |
| $C_{Plasma}$ | activity of $^{18}$F-FDG in blood plasma |
| CO | cardiac output |
| $CO_2$ | carbon dioxide |
| CPAP | continuous positive airway pressure |
| CT | computed tomography |
| $CV^2$ | coefficient of variation squared |
| $E_{rs}$ | elastance of the respiratory system |
| $\%E_2$ | distension index |
| $F_{Blood}$ | fractional volume of pulmonary blood |
| $F_{Gas}$ | fractional gas content |
| $F_{Tissue}$ | fractional tissue content |
| $FiO_2$ | fraction of inspired oxygen |
| FRC | functional residual capacity |
| HU | Hounsfield unit |
| $I_{FM,net}$ | net fluorescence intensity |
| ICU | intensive care unit |
| I:E | time ratio of inspiration to exspiration |
| IL-6 | interleukin-6 |
| IL-8 | interleukin-8 |
| $K_i$ | net uptake rate of $^{18}$F-FDG |
| $K_{iS}$ | specific net uptake rate of $^{18}$F-FDG |
| MV | minute ventilation |
| $P_{aw}$ | airway pressure |
| $P_{aw,mean}$ | mean airway pressure |

| | |
|---|---|
| $P_{aw,peak}$ | peak airway pressure |
| $P_L$ | transpulmonary pressure |
| $P_{L,mean}$ | mean transpulmonary pressure |
| $P_{L,peak}$ | peak transpulmonary pressure |
| $PaCO_2$ | arterial partial pressure of carbondioxid |
| $PaO_2$ | arterial partial pressure of oxygen |
| $PaO_2/FiO_2$ | Horovitz Index |
| PBW | predicted body weight |
| PEEP | positive end-expiratory pressure |
| PET | positron emission tomography |
| PTP | pressure time product |
| $\dot{Q}_{abs}$ | absolute lung perfusion |
| $Q_{RM}$ | mass-normalized, relative radioactive intensity |
| $Q_{RM,downscaled}$ | downscaled mass-normalized, relative radioactive intensity |
| $Q_{FM,Mass}$ | mass-normalized, relative fluorescence intensity |
| $Q_{FM,Volume}$ | volume-normalized, relative fluorescence intensity |
| $Q_{FM,Mass,Volume}$ | mass- and volume-normalized, relative fluorescence intensity |
| $R_{rs}$ | resistance of the respiratory system |
| ROI | region of interest |
| RR | respiratory rate |
| SB | spontaneous breathing |
| SUV | standard uptake value |
| TNF-α | tumor necrosis factor-alpha |
| $V_{Tissue}$ | lung tissue volume |
| VILI | ventilator induced lung injury |
| $V_T$ | tidal volume |
| $^{18}F$ | fluorine-18 |
| $^{18}F$-FDG | 2-deoxy-2-[$^{18}F$]fluoro-D-glucose |
| $^{68}Ga$ | gallium-68 |
| $^{68}Ga$-$PET_{net}$ | $^{68}Ga$ net activity |
| $^{68}Ga$-$PET_{before}$ | activity emitted by $^{68}Ga$-labeled microspheres injected for $^{68}Ga$-PET scans at previous time points |
| $^{68}Ga$-$PET_{after}$ | activity emitted by $^{68}Ga$-labeled microspheres injected at actual time point |
| ΔP | driving pressure |

# 1 Introduction

## 1.1 Overview

Since the first clinical description of acute respiratory distress in adults was published in 1967 (Ashbaugh et al., 1967), the development of new lung imaging techniques and the rapidly increasing availability of imaging technology have greatly contributed to the current understanding of the pathophysiology of the acute respiratory distress syndrome (ARDS). The latest definition of ARDS, the Berlin definition, emphasized the crucial role of imaging for the detection of the syndrome (Ferguson et al., 2012). Accordingly, besides hypoxemia, an important hallmark of the clinical syndrome of ARDS is the occurrence of reduced lung aeration, manifested by bilateral opacities on chest x-rays or computed tomography (CT) scans.

In recent years, technical innovations have allowed the development and application of several new imaging techniques. The gamut has evolved from simple chest x-ray as the technological precursor of CT, to several additional structural and functional pulmonary imaging techniques, such as positron emission tomography (PET). Only four years after the first PET scanner was developed, Wagner and Welch reported about a new procedure developed for the labeling of albumin microparticles (microspheres) with the positron-emitter gallium-68 ($^{68}$Ga). This compound allows PET-derived *in vivo* measurements of lung perfusion (Wagner & Welch, 1979a). Thus, the radiological assessment of lung aeration can be supplemented with PET-derived measurements of lung perfusion. The simultaneous acquisition of both structural and functional information is of especial interest in ARDS, where alterations in both aeration and perfusion impair gas exchange.

Because of a mismatch of aeration and perfusion in most patients suffering from ARDS, mechanical ventilation is usually required in order to maintain oxygenation and carbon dioxide ($CO_2$) removal and relieve the increased work of breathing. However, mechanical ventilation also has the potential to exacerbate existing lung injury and pulmonary neutrophilic inflammation. This phenomenon is termed **ventilator induced lung injury** (VILI). CT studies have revealed two primary potential mechanisms of VILI, which are tidal overdistension (i.e., volutrauma) and cyclic closing and reopening of small airways and alveoli (i.e., atelectrauma), (Muscedere et al., 1994). A recent study demonstrated that both volutrauma and atelectrauma can occur at the same time in different regions of the lung, despite the use of protective mechanical ventilation (Borges

et al., 2015), triggering an inflammatory response of the lung. However, to the knowledge of the author, a comparative analyzis of the individual impact of volutrauma and atelectrauma on the development and the persistence of induced lung injury has yet to be performed.

Before the *in vivo* assessment of both structural and functional abnormalities in ARDS by PET/CT became widely available in hospitals, alternative techniques were used in experimental studies to assess pulmonary aeration, perfusion, and neutrophilic inflammation. For instance, microspheres labeled with non-radioactive tracers, such as fluorescent particles, allowed the analyzis of the distribution of pulmonary blood flow (Glenny et al., 1993). The assessment of the distribution of such microspheres can be performed without the use of PET/CT scanners. However, the analyzis of perfusion measurements with fluorescence-labeled microspheres must be performed *ex vivo*, which can cause deformation of the lung and thereby affect perfusion distribution. The fluorescence-labeled microspheres derived assessment of pulmonary perfusion distribution had originally been designed to study perfusion distribution in healthy lungs (Glenny et al., 1993). So far, there is no study validating whether fluorescence-labeled microspheres derived measurements of pulmonary perfusion distribution are valid in injured lungs.

Imaging with PET/CT allows for *in vivo* and non-invasive quantification of the distribution of aeration, perfusion, and neutrophilic inflammation of almost the entire lung (Pesenti et al., 2016; Bellani et al., 2017). It is therefore an appropriate method to study the synergistic effects of both volutrauma and atelectrauma on the inflammatory response of the lung in ARDS and to validate the use of fluorescence-labeled microspheres in acutely injured lungs.

## 1.2 Background

### 1.2.1 Pulmonary Pathophysiology Of Acute Respiratory Distress Syndrome (ARDS)

ARDS is a life-threatening pulmonary condition, which is associated with relatively high morbidity and mortality in intensive care unit (ICU) patients. An international, multicenter study reported that, during an examination period of 4 weeks, 10.4 % of all patients admitted to the ICU in 50 countries of all five continents fulfilled ARDS criteria. Depending on the level of ARDS severity the mortality ranged between 34.9 % for those with mild and 46.1 % for those with severe ARDS (Bellani G et al., 2016). The mortality has not decreased significantly since 1994 despite ongoing research, which reflects the importance of further investigation on ARDS.

Ashbaugh and coworkers published for the first time a clinical description of acute respiratory distress in adults (Ashbaugh et al., 1967). They reported about 12 patients that suffered from an acute onset of tachypnea, hypoxemia, decreased lung compliance and diffuse 'bilateral alveolar infiltrates' seen in radiographs of the chest. Following this initial description of ARDS, multiple definitions have been proposed. However, a clear definition was missing. In 1994 the American-European Consensus Committee on ARDS published a new definition (Bernard et al., 1994a), which has been used for several years. According to that definition, ARDS is characterized by an acute onset of hypoxemia (arterial partial pressure of oxygen to fraction of inspired oxygen, $PaO_2/FiO_2$, i.e. Horovitz Index) ≤ 200 mmHg), bilateral, pulmonary infiltrates on frontal chest radiograph, and by no evidence of left atrial hypertension. According to the Horovitz Index they also described a new entity for patients with less severe hypoxemia, so-called acute lung injury ($PaO_2/FiO_2$ ≤ 300 mmHg). Since issues regarding the reliability and validity of this definition emerged, a panel of experts developed the Berlin Definition of ARDS in 2011. As of that, ARDS is a diffuse and acute inflammatory disease of the lung that is characterized by loss of aeration of lung tissue, increased permeability of the pulmonary-capillary membrane causing edema, increased work of breathing and impaired gas exchange (Ferguson et al., 2012). Instead of differentiating between acute lung injury and ARDS, they proposed 3 degrees of severity of ARDS, based on the level of hypoxemia: mild ARDS (200 mmHg < $PaO_2/FiO_2$ ≤ 300 mmHg), moderate ARDS (100 mmHg < $PaO_2/FiO_2$ ≤ 200 mmHg), and severe ARDS ($PaO_2/FiO_2$ ≤ 100 mmHg). Of note, higher severity of ARDS had been associated with higher mortality and increased duration of mechanical ventilation in survivors (Bernard et al., 1994b).

**Etiology**

ARDS may result from direct injury to the lungs (pulmonary causes), but also from indirect lung injury (extra-pulmonary causes). Common pulmonary causes leading to direct lung injury are pneumonia and aspiration of gastric contents. Sepsis is associated with the highest risk of indirect lung injury (Pepe et al., 1982), followed by severe trauma with shock and multiple transfusions (Ware and Matthay, 2000). The risk of developing ARDS increases with the number of primary direct and indirect lung injury factors (Pepe et al., 1982). Secondary factors, such as chronic alcohol abuse or chronic lung disease, further increase the risk (Hudson et al., 1995).

Pulmonary endothelial and epithelial injury and, as a consequence, an increased permeability of the alveolar-capillary barrier are key features of the pathophysiological mechanisms of ARDS. As a consequence of the increased permeability of the epithelial barrier, influx of protein-rich edema fluid into the air spaces causes alveolar flooding. Furthermore, the production and turnover of surfactant is reduced, leading to an impairment of the mechanical properties of the lung and the formation of large atelectatic regions (Ware and Matthay, 2000). Atelectasis together with leakage of edema fluid and inflammatory cellular infiltrates cause a mismatch of ventilation and perfusion (Wheeler and Bernard, 2007).

**Therapy**

In order to counteract gas exchange failure and to reduce the work of breathing, mechanical ventilation is usually required in patients with ARDS. The increasing understanding of the pathophysiology of ARDS has led to the development and optimization of several protective mechanical ventilation strategies, which all aim to reduce morbidity and mortality of patients with ARDS. Those concepts include reduced tidal volume ($V_T$) to limit lung stress and strain, low airway pressures ($P_{aw}$) to reduce overdistension and the application of adequate positive end-expiratory pressure (PEEP) to reduce alveolar collapse, preventing cyclic collapse and reopening.

Protective mechanical ventilation with low $V_T$ has been proven to decrease the mortality in patients with ARDS (Amato et al. 1998; Ware, 2006). Also, the use of prone position was shown to improve survival in these patients (Guérin et al., 2013). However, the therapy of ARDS remains merely supportive, and aims at gaining time until the primary disease is treated (Gattinoni and Quintel, 2016)

### 1.2.2 Ventilator Induced Lung Injury

Concerns about the harmful impact of mechanical ventilation are at least as old as the description of ARDS itself. In 1967, Nash and coworkers already expressed concerns that, in patients requiring mechanical ventilation, the pulmonary function gradually worsened and that this worsening seemed to be unrelated to the diseases requiring pulmonary function assistance (Nash et al., 1967).

While during spontaneous breathing inspiration is driven by negative inspiratory $P_{aw}$, mechanical ventilation generates positive $P_{aw}$ in order to initiate inspiration. This positive pressure can lead to abnormal distribution and amplitude of mechanical forces across the lungs. Ideally, the positive pressure is equally distributed across all alveoli. However, Gattinoni and coworkers showed that patients with ARDS feature a markedly reduced extent of normally aerated lung, which has the approximate volume of the lung of a 5 to 6 year-old child (Gattinoni et al., 1986c). In addition, alveolar edema accumulates. The overall stiffness of the lung is reduced as only the residual normally aerated lung regions feature nearly normal elastic properties (Gattinoni and Pesenti, 2005). Therefore, ARDS lungs are inhomogeneous regarding both their structure and function. Inspiratory distending pressures and associated forces acting on the pulmonary micro-structures become heterogeneously distributed. The same transpulmonary pressure, which is acting as the distending force of the lung, is applied to a smaller part. Consequently, mechanical ventilation can result in an overdistension of the remaining, already well-aerated, non-dependent lung regions (Gattinoni et al., 2003), even when $V_T$ is limited to 6 mL/kg of predicted body weight (PBW), and plateau pressure does not exceed 30 $cmH_2O$ (Terragni et al., 2007). The associated high static stress and strain can lead to disruption of airways and alveolar walls and breakage of cellular membranes (overstretching). Damage of the lung from tidal overdistension is called baro- or **volutrauma**.

When mechanical ventilation is applied to an inhomogeneous lung or PEEP is insufficient to keep the lungs open at the end of expiration, parts of the collapsed or poorly aerated lung areas reopen and collapse at the end of inspiration and expiration, respectively (tidal recruitment). This can occur even at very low $V_T$ of 5 to 6 mL/kg PBW (Muscedere et al., 1994), and can generate excessive shear stress at the boundaries between open and collapsed alveoli (Mead et al., 1970). Non-physiological changes in airway diameter and cell morphology and associated non-physiological pressure gradients around the reopening alveoli and airways can also damage pulmonary epithelial cells (Bilek et al., 2003). Injury induced by cyclic recruitment and derecruitment is usually termed **atelectrauma**.

*Ex vivo* studies have revealed that both volutrauma and atelectrauma are potential mechanisms of VILI. In a VILI model of ARDS in rats, Webb and Tierney found that 1 h of mechanical ventilation with a peak inspiratory $P_{aw}$ of 45 $cmH_2O$ and zero PEEP caused development of hypoxemia, perivascular and alveolar edema, decreased dynamic compliance, and death within one hour (Webb and Tierney, 1974). In isolated, non-perfused, lavaged rat lungs, Muscedere and coworkers found that ventilation with a $V_T$ of 5 to 6 mL/kg PBW and PEEP adjusted to remain below the lower inflection point of the pressure-volume curve caused dramatic reduction of lung compliance and the development of substantial lung injury as assessed morphologically by airway injury scores and hyaline membrane formation (Muscedere et al., 1994).

Abnormal cyclic stretching of lung tissue due to volutrauma or atelectrauma can lead to the activation of macrophages and trigger the production of cytokines, including interleukin-6 (IL-6), interleukin-8 (IL-8), and tumor necrosis factor-alpha (TNF-α), (Tremblay et al., 1997). Those cytokines attract and activate neutrophils with a consequent high and complex inflammatory response of the lung (Gattinoni et al., 2003). *In vivo* studies using lung imaging with PET and the glucose analog 2-deoxy-D-glucose labeled with fluorine-18 ($^{18}F$), ($^{18}F$-FDG) confirmed that mechanical ventilation can cause volutrauma and atelectrauma in specific, heterogeneously distributed lung regions, and that both mechanisms seem to worsen lung injury (Musch et al., 2007; de Prost et al., 2011).

However, *ex vivo* and *in vivo* studies have yielded disparate findings regarding the degree of injury induced by volutrauma and atelectrauma. In a saline lung lavage model of ARDS in rabbits, Otto and coworkers found that after ventilation with high $V_T$ of 28 mL/kg PBW, low respiratory rate (RR) of 8 breaths per minute, and low PEEP of 3 $cmH_2O$ for up to 6 h, edema formation, expression of IL-8, and alveolar neutrophil accumulation progressed more rapidly in dependent lung regions. This indicates that atelectrauma might have caused a higher inflammatory response as compared to volutrauma (Otto et al., 2008). In contrast, in a saline lung lavage model of acute lung injury in rabbits, Tsuchida and coworkers found that 90 min of injurious mechanical ventilation with $V_T$ of 25 mL/kg PBW and PEEP of 4 to 7 $cmH_2O$ was associated with higher alveolar injury (i.e., histology, myeloperoxidase protein expression, quantification, and localization of cytokine mRNA expression) in non-dependent, non-atelectatic regions associated with alveolar overdistension, as compared to dependent, atelectatic regions (Tsuchida et al., 2006).

Consistent with this, in a double hit model of ARDS in sheep, Borges and coworkers found that 27 h of protective mechanical ventilation with low $V_T$ of 6 mL/kg PBW was associated with higher neutrophilic inflammation in non-dependent lung regions associated with volutrauma as compared to the second most ventral region, which was associated with typical features of atelectrauma (Borges et al., 2015).

The differing findings about the degree of injury induced by volutrauma and atelectrauma were very likely determined by a different extent of volutrauma and atelectrauma in various ARDS models. Their relative contribution to VILI is not well established. This insight may be relevant not only to better understand the mechanisms of VILI, but also to improve protective mechanical ventilation strategies in patients with ARDS.

### 1.2.3 Animal Models of ARDS

*In vivo* studies are necessary to gain insights into the pathophysiological mechanisms and to understand the impact of new treatment strategies in ARDS. Usually, such studies cannot be performed in patients, especially when radioactive material or ionizing radiation, or both, is used. Therefore, experiments in animals are necessary. In 2010, Matute-Bello and coworkers summarized that an animal model of ARDS should reproduce at least three of the following four main features of experimental acute lung injury: (1) histological evidence of tissue injury; (2) alteration of the alveolar capillary barrier; (3) a pulmonary inflammatory response; and (4) evidence of physiological dysfunction (Matute-Bello et al., 2011). The most commonly used models of ARDS are: intravenous infusion of lipopolysaccharide, instillation of hydrochloric acid into the tracheobronchial tree, intravenous infusion of oleic acid, injurious mechanical ventilation, and repetitive bronchoalveolar lavage with saline (Rosenthal et al., 1998a). However, none of those animal models of ARDS is able to reproduce all features of human ARDS. Therefore, the model used in an experimental study of ARDS has to be chosen in respect to the particular question being studied.

The saline lavage model of ARDS developed by Lachmann and coworkers in 1980 is based on the observation that ARDS in humans is associated with the depletion of surfactant (Lachmann et al., 1980). Lung injury induced by surfactant depletion is produced by two mechanisms. The washout of alveolar surfactant increases the surface tension of the alveoli, which, as a consequence, promotes collapse of the alveolar space and small airways and increases the risk of tissue damage due to cyclic recruitment and derecruitment. In addition, the depletion of surfactant is associated with an impairment of alveolar host defenses (Matute-Bello et al., 2008a). As a consequence, gas exchange is impaired and immediate hypoxemia results (Lachmann et al., 1980), while hemodynamics remain stable (Rosenthal et al., 1998b) and the inflammatory response remains relatively mild (Matute-Bello et al., 2008a).

The double hit model of ARDS includes saline lavage as first hit, followed by injurious mechanical ventilation with high volume changes or high static volumes, or both, as second hit. Injurious mechanical ventilation can cause cyclic recruitment and derecruitment, which is associated with an injury of the alveolar wall and the accumulation of alveolar edema. A type of injury develops that is very similar to human ARDS, including the following key features: hypoxemia, presence of atelectatic regions, reduction of compliance, and increased shunt fraction associated with a mismatch of ventilation and perfusion.

### 1.2.4 Assessment of Pulmonary Aeration by Computed Tomography (CT)

In the original description of acute respiratory distress in adults in 1967, chest x-ray imaging was already used to describe typical features of the disease (Ashbaugh et al., 1967). However, due to missing criteria for the interpretation of chest radiographs, they showed poor inter-observer reproducibility. In 1983, Rommelsheim and coworkers reported for the first time about the use of CT in ARDS. The authors described a “dorso-central distribution of densities observed especially during the edematous phase of the syndrome” (Rommelsheim et al., 1983). In the two following papers published independently in April 1986, CT revealed that dense lung tissue areas are not homogeneously distributed in patients with ARDS, contrary to what chest x-rays had mostly suggested, and instead are mostly found in dependent lung regions (Gattinoni et al., 1986a; Maunder RJ et al., 1986). Maunder and coworkers also reported on the impact of PEEP on tissue density, showing responsiveness to PEEP in some patients but not in others (Maunder RJ et al., 1986). Since then, CT has had a substantial impact on the understanding of the pathophysiology of ARDS. In fact, in the Berlin definition of ARDS, CT is explicitly recommended as substitute for chest radiography for the diagnosis of bilateral opacities (Ferguson et al., 2012). In comparison to chest radiograph, CT has been proven to be more accurate for the diagnosis and the identification of the underlying causes of ARDS (Mazzei et al., 2012; Sheard et al., 2012). In addition, CT provides data with relatively high spatial resolution. Therefore, CT has become the gold standard for the diagnosis of bilateral opacities. However, the advantages of CT have to be weighed against its risks, including exposure to ionizing radiation as well as logistical aspects like the transport of critically ill patients to the imaging facility.

CT was developed by the English physicist Hounsfield in 1967, and measures the attenuation of x-ray beams passing an imaged region. In the CT scanners of today’s state of technology, 700 to 1000 detectors are stationary and assembled in a fixed circle around the field of view. Only the x-ray tube rotates around the body and emits x-rays (Hounsfield, 1980). The detectors measure the percentage of x-rays absorbed by the tissue of given volume within the scanned region. Helical rotation of the x-ray tube around the field of view and repetitive measurements of the attenuation of the x-rays at different angles of the x-ray tube allow the acquisition of a three-dimensional dataset. Solving linear equations in the course of back projection methods allows the approximate determination of attenuation coefficients for all volume elements (voxel) within the three-dimensional imaged field of view without an overlap.

Although the first CT scanners became available in the mid-1970s, the first reports about CT imaging of acute respiratory failure were reported in the mid-1980s (Rommelsheim et al., 1983; Gattinoni et al., 1986b; Maunder RJ et al., 1986). Since then, quantitative analyzes of CT data has more widely been used and has so far provided the most relevant information about ARDS (Gattinoni et al., 2001).

The relationship between the CT number and the physical density of the material being studied (grams per milliliter) is complex and depends on the incident energy, atomic number of the tissue, mass electron density, and the physical density itself. However, it has been shown experimentally that the first three mentioned factors are approximately constant and that the CT number is mainly determined by the physical density (Gattinoni et al., 1986d). Therefore, a simplified linear correlation between the CT number and the density of an imaged region, as shown in Equation (1.1), is well accepted.

$$\text{CT number} = \frac{\mu_x - \mu_{H_2O}}{\mu_{H_2O}} \times 1000 \tag{1.1}$$

The variable $\mu_x$ represents the attenuation coefficient of x-rays in a defined volume of the material being studied and $\mu_{H2O}$ is the attenuation coefficient of water. The CT number is expressed in Hounsfield units (HU).

A higher CT number therefore suggests that the density of a lung element, which is determined by the content of alveolar gas, lung tissue, blood, and water within the voxel, is increased (Gattinoni et al., 2001). The linear relationship shown in Equation (1.1) can be used to calculate the average fractional gas content ($F_{Gas}$) within a region of interest, as shown in Equation (1.2).

$$F_{Gas} = \frac{\text{CT number}}{-1000} \tag{1.2}$$

The fractional gas content (degree of aeration) of lung tissue usually decreases when the degree of severity of ARDS increases.

### 1.2.5 Principles of Positron Emission Tomography (PET)

PET is a functional imaging technique that allows quantification of physiological processes. A radiopharmaceutical, also called a tracer, is composed of a molecule that is labeled with an unstable radioisotope. This compound is usually injected intravenously and distributes throughout the body via the blood stream. The unstable radioisotope decays by the emission of positrons. Depending on the initial energy of the positron and on the tissue density, it travels a certain distance within the body until it interacts with an electron of the surrounding matter. This annihilation event leads to simultaneous emission of two photons of equal and high energy that travel in the exact opposite direction. The two photons reach the circularly arranged detectors of the PET scanner surrounding the field of view almost simultaneously, i.e. in coincidence. This allows the localization of the annihilation event along the line between these two registering detector elements (so-called line of response). Figure 1.1 illustrates one such event and the travel of the emitted photons.

The placement of several detector pair combinations in rings around the studied object allows the simultaneous detection of several million coincidences (Phelps, 2000). Reconstruction of the detected coincidences provides tomographic images of the spatial distribution of the tracer within the scanned field of view. PET-derived measurements are expressed as activity concentration, which specifies the activity originating from the tracer (expressed in Becquerel, Bq) relative to the volume in which the tracer is spread (expressed in ml). One Becquerel is equal to one radioactive decay per second. The reconstruction of the derived data includes several corrections, mainly for photon attenuation and scatter, random coincidences, and radioactive decay.

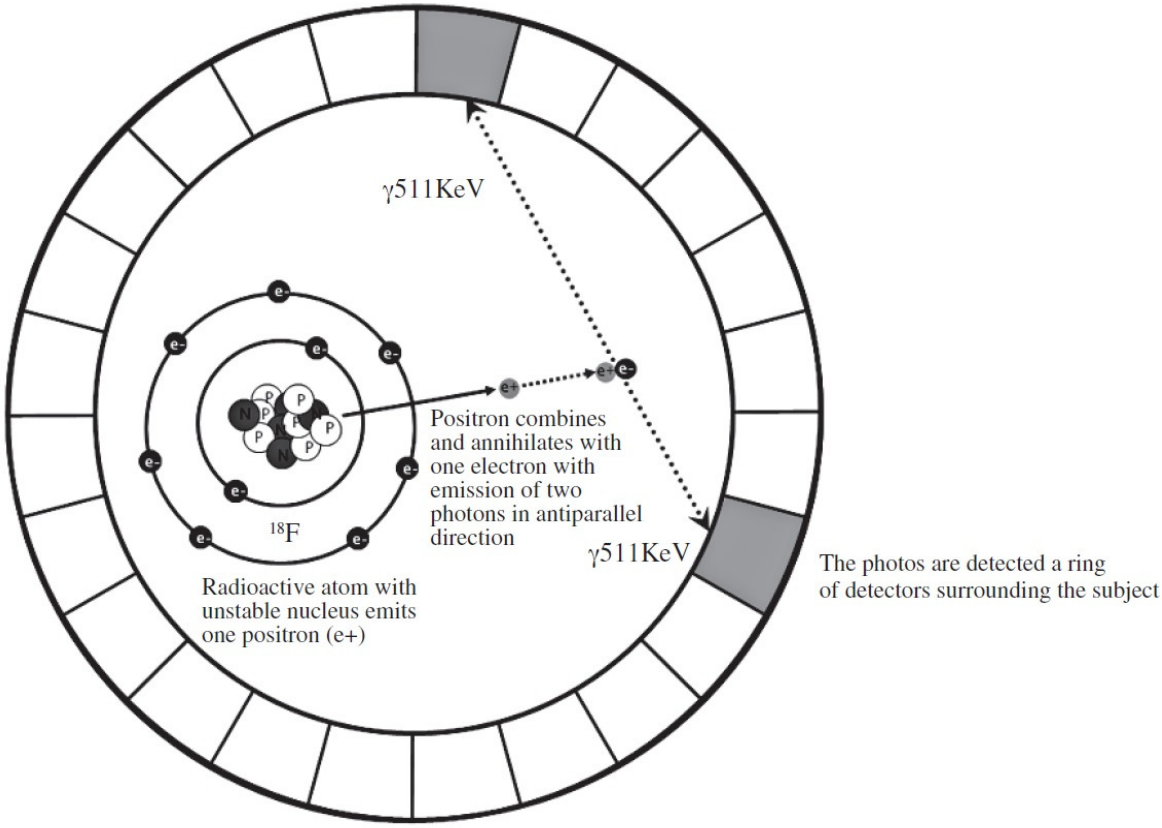


***Figure 1.1:*** *Schematic description of the principles of PET imaging. Reproduced and modified from (Bellani et al., 2011).*

Some of the advantages of PET scanning are its *in vivo* and non-invasive measurements and the fact that measurements are derived as three-dimensional datasets. This allows the detection of regional abnormalities and the correlation of PET data with data derived from other imaging techniques, such as structural information derived from CT. Among the disadvantages are limited resolution and radiation exposure. Since imaging takes several minutes for static PET scanning of the whole lung, and 60 to 75 min for dynamic PET imaging, artifacts due to cardiac and respiratory motion cannot be completely avoided. Whereas static PET scanning allows for determination of the spatial distribution of a tracer within a big field of view, dynamic PET scanning allows for tracking tracer's kinetics over time.

## 1.2.6 Assessment of Regional Pulmonary Perfusion

### 1.2.6.1 Measurement of Regional Pulmonary Perfusion with $^{68}$Ga-labeled Microspheres and PET

In 1979, and therefore only 4 years after the first PET scanner was developed, Wagner and Welch had begun to study the labeling of human serum albumin microspheres with the tracer $^{68}$Ga (Wagner and Welch, 1979), which can be used for static PET-derived *in vivo* measurements of the vascular permeability. The department of nuclear medicine of the University Hospital Carl Gustav Carus has the expertise and required facilities to label human albumin microspheres (HSA Mikrosphären B20, ROTOP Pharmaka GmbH, Dresden, Germany) with $^{68}$Ga (Kotzerke et al., 2010; Oehme et al., 2014). Briefly, $^{68}$Ga is produced using a germanium-68/gallium-68 generator (ITG Isotope Technologies Garching GmbH, Germany) and taking advantage of the decay of germanium-68 to gallium-68. Thereafter, microspheres B20 get labeled with $^{68}$Ga using a microsphere B20 kit (Rotop Pharmaka GmbH, Dresden, Germany). The human serum B20 albumin microspheres have an outer diameter of 10 to 30 µm, which is not altered upon binding of $^{68}$Ga to the microspheres. The $^{68}$Ga-labeled albumin microspheres feature a high stability, an excellent *in vivo* stability, biocompatibility, and a uniform size (Wunderlich et al., 2010; Wagner and Welch, 1979). They have also been shown to be an accurate tool to study pulmonary perfusion *in vivo* (Richter et al., 2015; Beck, 1987b; Richard et al., 2002). In view of these facts, several experimental studies used $^{68}$Ga-labeled microspheres and PET scanning for the assessment of pulmonary perfusion in ARDS animals (Richter et al., 2005; Güldner et al., 2014; Richter et al., 2015). It has been shown that following intravenous injection into the pulmonary artery, almost all $^{68}$Ga-labeled microspheres are trapped in the pulmonary capillaries and arterioles during the first pass, while other organs are practically not reached (Willmott et al., 1989). The magnitude of the regional trapping, or micro-embolism formation, is directly proportional to regional perfusion. It is estimated that 100.000 microspheres temporarily occlude approximately every millionth capillary and every thousandth arteriole, which represents about 0.5 % of all pulmonary blood vessels (ROTOP Pharmaka GmbH, 2016). It can therefore be assumed that the injection of an appropriate number of microspheres does not importantly alter the pulmonary perfusion (Glenny et al., 2000a).

Static PET scanning of the coincidences originating from the decay of $^{68}$Ga allows the detection of the trapped $^{68}$Ga-labeled microspheres right after their injection. However, especially in ARDS lungs, tissue density and thereby the extent of lung tissue per voxel is mostly heterogeneous throughout the lung. Therefore, the number of trapped $^{68}$Ga-labeled microspheres in the pulmonary capillary bed has to be corrected for the number of blood vessels the microspheres are trapped in. Assuming a linear correlation between tissue density and the number of blood vessels supplying the tissue, regional pulmonary perfusion can be determined as the ratio of the PET-derived number of trapped $^{68}$Ga-labeled microspheres relative to the CT-derived tissue density. Thus, ideally, the PET estimations of lung perfusion are independent of regional difference in lung inflation and allow quantitative analyzis of pulmonary perfusion of ARDS lungs (Richter et al., 2010).

Since one PET scan only captures a 15 cm cranio-caudal field of view, three static PET scans at different overlapping bed positions are usually required to image the whole lung of large animals or adult human beings.

#### 1.2.6.2 Measurement of Regional Pulmonary Perfusion with Fluorescence-labeled Microspheres

Compared to radioactive microspheres, the use of fluorescence-labeled albumin microspheres is a non-radioactive and cheaper alternative for measurements of regional pulmonary blood flow (Glenny et al., 1993). Fluorescence-labeled microspheres show a relatively long shelf life and do not require an expensive, radioactivity facility, which simplifies their use.

The microspheres are injected intravenously at the time point the perfusion is of interest. The use of different fluorescence colors allows perfusion measurements at different time points. Also here, and as explained in chapter 1.2.6.1, the number of trapped fluorescence-labeled microspheres is proportional to regional pulmonary perfusion (Beck, 1987b). In contrast to the $^{68}$Ga-labeled microspheres technique, the analyzis of the extent of trapped fluorescence-labeled microspheres is done *ex vivo*. Retrieving fluorescence-labeled microspheres out of solid organs requires many laboratory intensive steps. The lungs have to get extracted at the end of the experiments and get cut into pieces. By soaking the lung tissue pieces in 2-ethoxyethyl acetate, the fluorescence-labeled microspheres get dissolved out of each piece, releasing the fluorescent dye. The emitted fluorescence intensity is read using a luminescence spectrophotometer. In the course of a following analyzis of the measurements, lower fluorescence signals obtained from outermost lung pieces containing less lung tissue have to be adjusted. In studies done in healthy animals this correction is done by normalizing

the measured fluorescence intensity to the mass of the lung piece. This correction is based on the assumption that the drying of healthy lungs at high pressures fully opens all alveoli to equal volume resulting in homogeneous lung tissue density. It is further assumed that only the extent of lung tissue alters the mass of lung pieces. Consequently, the mass of a tissue sample is expected to correlate with its volume and can be used as surrogate for tissue content (Glenny et al., 1993).

So far, only a few studies with fluorescence-labeled microspheres have been performed in injured lungs (Hübler et al., 1999; Hübler et al., 2001; Carvalho et al., 2011). In contrast to healthy lungs, injured lungs behave as solid organs (Hübler et al., 1999), and typically feature a large proportion of collapsed alveoli. It is therefore questionable whether drying severely injured lungs at high pressure during the process of the analyzis of the excised lungs would be sufficient to fully open consolidated regions. In addition, inflammatory deposition, cellular infiltration due to inflammation, and hemorrhages can alter the mass of pieces of injured lungs (Robertson and Hlastala, 2007). This could explain why Hübler and coworkers noted in their study in ARDS sheep lungs that tissue pieces of severely injured lungs featured a higher mass range as compared to those of healthy lungs (Hübler et al., 1999). Whether the mass of a sample of an injured lung correlates with its volume and whether it is an appropriate surrogate for tissue content has yet to be determined.

Comparisons of pulmonary perfusion measurements performed *ex vivo* using fluorescence-labeled with those performed *in vivo* using radiolabeled microspheres have been conducted almost exclusively in healthy animals (Glenny et al., 1993; Van Oosterhout et al., 1998). To the knowledge of the author, the comparison of fluorescence-labeled and radiolabeled microspheres measurements in injured lungs was addressed in one single study (Hübler et al., 1999). However, in this study both the radio- and fluorescence-labeled microspheres measurements were conducted *ex vivo*, and did not address the effects of possible inhomogeneous lung tissue density on measurements of lung perfusion.

## 1.2.7 Assessment of Pulmonary Inflammation

### 1.2.7.1 Cellular, Molecular and Histological Methods

Different methods are available for direct or indirect quantification of different aspects of pulmonary inflammation, including:

- Inflammatory cell count, especially neutrophils;
- Quantification of the protein concentrations of the IL-6, IL-8, and TNF-α using enzyme linked immuno-sorbent assay development systems;
- Analysis of wet- to- dry ratios;
- Histologic analyzis of lung tissue samples using light microscopy for quantification of the diffuse alveolar damage;
- Immune-biochemical analyzis of bronchoalveolar lavage fluid.

However, the results are limited to certain regions of the lungs, and may not be representative for the inflammation of the whole lung. This is a crucial limitation since non-homogenous distribution of inflammation is common in ARDS (Bellani et al., 2009; Rodrigues et al., 2008; Jones et al., 2002).

### 1.2.7.2 $^{18}$F-FDG for Quantification of Pulmonary Neutrophilic Inflammation

*In vivo* imaging of pulmonary neutrophilic inflammation using $^{18}$F-FDG and dynamic PET scanning is a more recently described approach, which allows the *in vivo* assessment of a 15 cm cranio-caudal section of the lung. Its first use in patients with ARDS was reported by Jacene and coworkers (Jacene et al., 2004), who described a markedly increased and diffuse uptake of $^{18}$F-FDG in a patient with ARDS.

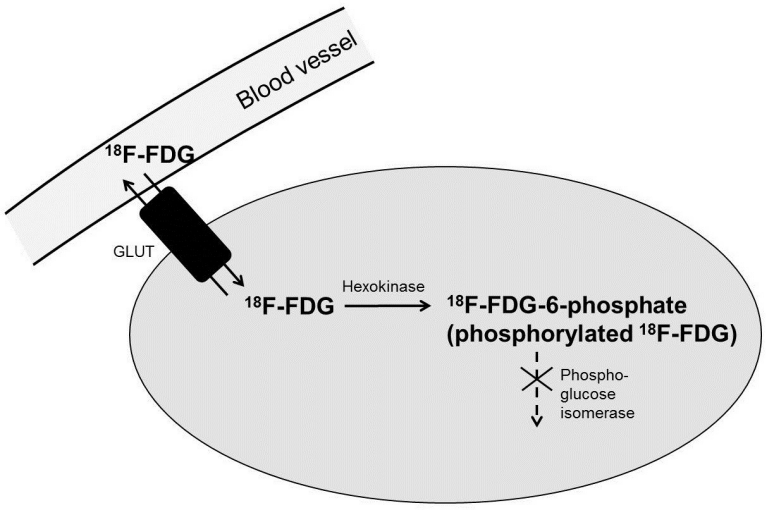


***Figure 1.2:*** *Pathway of $^{18}$F-FDG out of the blood into the cells and following phosphorylation. Arrows illustrate forward and reverse transport between blood plasma and tissue, phosphorylation and de-phosphorylation. Reproduced and modified from (Bellani et al., 2011).*

Due to the long half-life of the $^{18}$F isotope of 109 min, the $^{18}$F-labeled glucose analog $^{18}$F-FDG is currently the most widely used PET tracer (Rudroff et al., 2015). After intravenous injection of $^{18}$F-FDG, it is transported out of the blood into the cells by the same transporters and at the same rate as glucose (Bellani et al., 2011). After the transport across the cell's membrane, $^{18}$F-FDG undergoes the first step of the glucose metabolism, which is the phosphorylation to $^{18}$F-FDG-6-phosphate by the enzyme hexokinase (Figure 1.2). The chemical structure of the phosphorylated $^{18}$F-FDG differs from that of glucose-6-phosphate (glucose-6-phosphate features one more oxygen atom as compared to $^{18}$F-FDG-6-phosphate), which precludes the further metabolization of phosphorylated $^{18}$F-FDG within the glycolytic pathway. Once phosphorylated, $^{18}$F-FDG is therefore irreversible trapped within the cells (Bellani et al., 2011). In the lung, de-phosphorylation of $^{18}$F-FDG is negligible within the imaging time of up to 75 min after injection (Gallagher et al., 1978). Therefore, dynamic PET measurements of the coincidences originating from the decay of $^{18}$F provide information about the amount of $^{18}$F-FDG accumulated within the cells. Inflammatory cells and especially neutrophils feature a much higher glucose metabolism as compared to other pulmonary cells such that $^{18}$F-FDG accumulation is higher (Chen et al., 2004a; Musch et al., 2007). Therefore, the measured radioactivity originating from a local region of interest is believed to reflect the number and the metabolic activity of inflammatory cells (Musch, 2011). PET scanning after the intravenous injection of $^{18}$F-FDG is routinely used in oncology to diagnose and monitor the treatment of tumors, since tumors show increased uptake of glucose for production of energy within the containing cells. Since the uptake of $^{18}$F-FDG by tissue is mainly determined by its metabolic activity, $^{18}$F-FDG-PET has also been used to study inflammatory conditions that are not related to a tumor (Jones, 2005). However, the radiation exposure limits the use of $^{18}$F-FDG and PET in ARDS studies to research.

**Cell Types Contributing to Pulmonary $^{18}$F-FDG Uptake**

In heathy lungs, the uptake of $^{18}$F-FDG is low (Chen and Schuster, 2004), and macrophages are the main modulator of the $^{18}$F-FDG, with some contribution from type II epithelial cells (Saha et al., 2013). In VILI, among the involved inflammatory cells, neutrophils seem to be the key modulators of the increased uptake rate of $^{18}$F-FDG (Jones et al., 2002; Saha et al., 2013).

Neutrophils are the most abundant type of white blood cells. They are responsible for the non-specific immune response of the body. Upon an inflammatory insult, these cells leave the blood vessels and accumulate in the microvasculature of the lung, especially during the acute phase of ARDS (the first 1 to 6 d), (Matthay and Zemans, 2011).

The neutrophils take up foreign matter and microorganisms, and decompose and defang them. This process dramatically increases the consumption of glucose per neutrophil, and, thus, increases their $^{18}$F-FDG uptake (Hogg, 1987). As a result, the higher $^{18}$F-FDG imaging signal in VILI can be attributed to the accumulation of neutrophils (Imanaka et al., 2001; Musch et al., 2007) and their higher state of activation in response to an inflammatory stimulus (Musch et al., 2007). However, Musch and coworkers showed that an increased $^{18}$F-FDG uptake during VILI cannot be exclusively ascribed to neutrophils (Musch et al., 2007). Saha and coworkers found in a murine mouse model of VILI induced acute lung injury that $^{18}$F-FDG is majorly taken up by neutrophils, while macrophages and type 2 epithelial cells contributed less to the $^{18}$F-FDG uptake by lung tissue (Saha et al., 2013).

**Methods for Quantification of Regional Pulmonary $^{18}$F-FDG Uptake**

Different methods have been established to quantify the regional, pulmonary uptake of $^{18}$F-FDG. The simplest approach involves static PET scans of the lung acquired between 45 min and 70 min after the intravenous injection of $^{18}$F-FDG and the calculation of the standard uptake value (SUV). The SUV is defined as the average accumulation of a tracer within a region (in Bq per gram of tissue), normalized to the applied tracer dose (in Bq) per unit of body weight (in g). In case of equal distribution of the tracer within the body the SUV values are 1 for the whole body. This parameter is frequently used in the clinical routine to characterize tumors. However, SUV is affected by many technical and physiological factors. SUV calculations do, for instance, not consider the level of $^{18}$F-FDG in the blood although it can affect the $^{18}$F-FDG uptake (Hoekstra et al., 2000; Hoekstra et al., 2002).

Another simple measure of the $^{18}$F-FDG uptake is the standard uptake ratio, which is defined as the SUV of the scanned region normalized to the SUV of the arterial blood at the time of the static PET scan (van den Hoff et al., 2013). It has been shown that the tissue-to-plasma activity ratio correlates with graphically determined $^{18}$F-FDG net uptake rates in animal models of acute lung injury (Chen et al., 2004b). However, both the SUV and the standard uptake ratio measurements do not distinguish whether the measured activity originates from $^{18}$F-FDG located in the blood or from $^{18}$F-FDG that has been taken up by lung tissue. As a result, inter- and intra- subject variability of the ratio of tissue to blood volume affect these measurements. This is of special relevance in the lung, were the ratio of blood to tissue is relatively high and the activity in the blood can therefore significantly contribute to the measured $^{18}$F-FDG activity. Furthermore, especially in injured lungs, regional gas and blood volume can differ significantly, affecting regional tissue density and therefore measurements of the standard uptake ratio (Musch et al.,

2007). The interest in more accurate methods has therefore led to the development of more precise models for the quantification of the uptake of $^{18}$F-FDG by lung tissue. Three tracer kinetic models are currently used for the analyzis of the dynamic $^{18}$F-FDG-PET scans and to calculate the $^{18}$F-FDG net uptake rate ($K_i$) by lung tissue. The models differ by the number of compartments, where each compartment describes a different state of the phosphorylation of $^{18}$F-FDG (Figure 1.3).

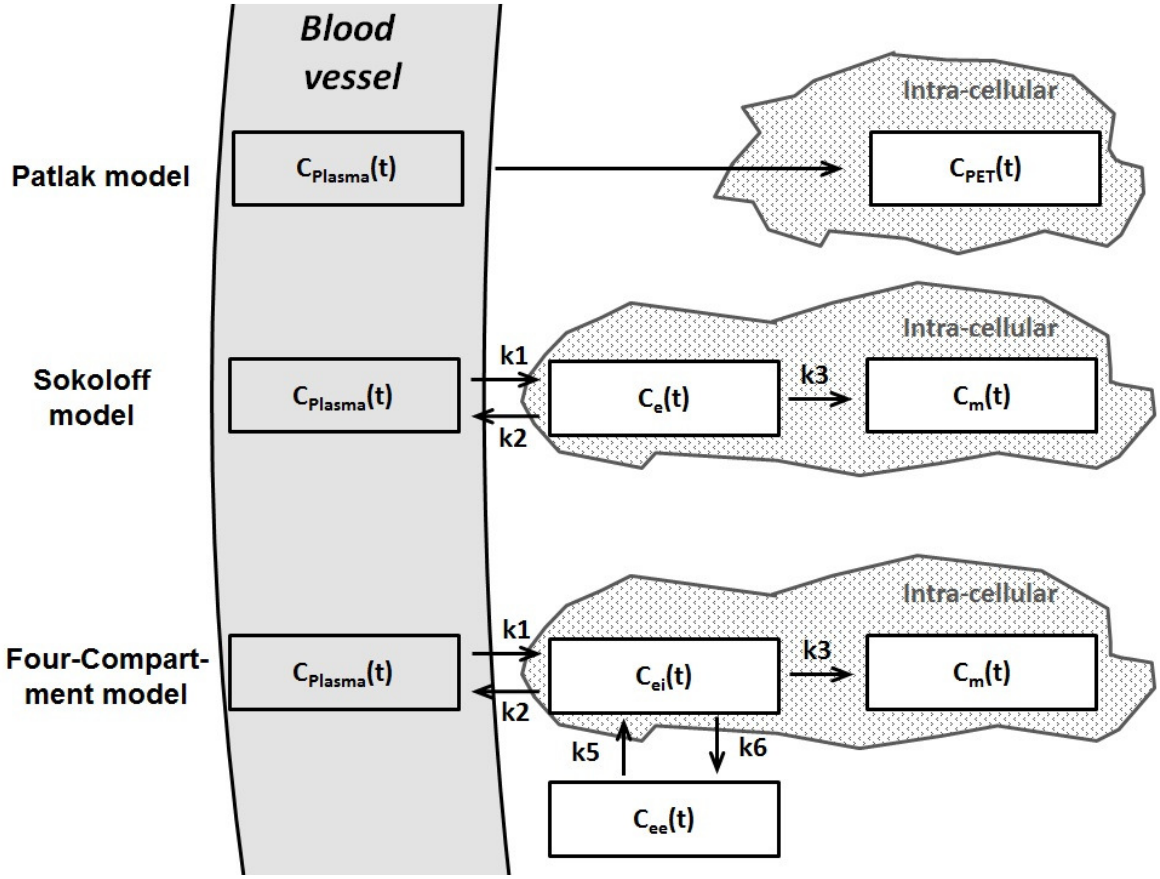


***Figure 1.3:*** *Tracer kinetic models of $^{18}$F-FDG: two-compartment (Patlak) model, three-compartment (Sokoloff) model, and lung-specific four-compartment model. Arrows indicate directions of mass transport. $C_{Plasma}(t)$ represents the activity concentration of $^{18}$F-FDG in plasma; $C_{PET}(t)$ represents the activity of $^{18}$F-FDG accessed by PET scanning; $C_m(t)$ represents the concentration of phosphorylated $^{18}$F-FDG; $C_e(t)$ and $C_{ei}(t)$ represent the $^{18}$F-FDG concentrations in extravascular compartment serving as substrate pool for hexokinase in Sokoloff ($C_e$) and in four-compartment ($C_{ei}$) models, $C_{ee}(t)$ represents the $^{18}$F-FDG concentration in extravascular or non-cellular compartment. Rate constants $k_1$ and $k_2$ account for forward and backward transport of $^{18}$F-FDG between blood and tissue and are expressed as [blood volume / (time * tissue volume)]; $k_3$ is the rate of the phosphorylation of $^{18}$F-FDG to $^{18}$F-FDG-6-phosphate irreversibly trapped in lung tissue, expressed as [1/time]; $k_5$ and $k_6$ account for forward and backward transport of $^{18}$F-FDG between substrate (intracellular) and non-substrate (extracellular) compartments. Reproduced and modified from (de Prost et al., 2010).*

**Patlak model of the $^{18}$F-FDG kinetics**

Patlak and coworkers developed a graphical model of the $^{18}$F-FDG uptake, which was originally used to study brain tissue (Patlak et al., 1983). For the evaluation of the $^{18}$F-FDG uptake, this model considers a central blood compartment and a peripheral compartment. The central compartment is in rapid equilibrium with blood plasma and describes the activity of $^{18}$F-FDG in blood plasma over time. The peripheral compartment describes the PET-derived concentration of irreversibly trapped $^{18}$F-FDG-6-phosphate in tissue over time. The activity of $^{18}$F-FDG in blood plasma over time can be measured either by continuous blood sampling coinciding with the PET frames, or by analyzing the imaging data of a blood pool such as the heart or the aorta (Schroeder et al., 2007). Solving the transfer function of $^{18}$F-FDG between both compartments yields the Patlak plot (Figure 1.4), on which the graphical analyzis is based. In this graph the activity of $^{18}$F-FDG in a region of interest ($C_{PET}$) normalized to the plasma activity ($C_{Plasma}$) is plotted against the cumulative plasma activity normalized to the plasma activity at the time point of the measurement ( $\int_{t=0}^{t} C_{Plasma}(\tau) * d\tau / C_{Plasma}(t)$ ), (Patlak et al., 1983).

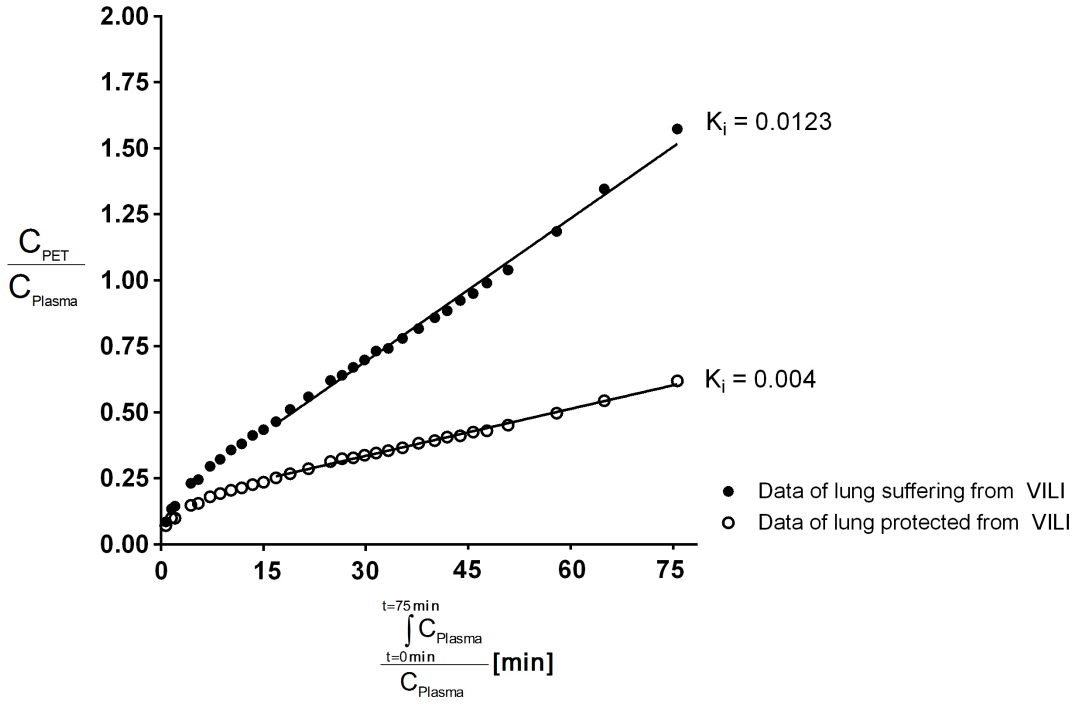


***Figure 1.4:*** *Example of the Patlak plot calculated for dynamic $^{18}$F-FDG-PET scans of a lung suffering from VILI (atelectrauma, solid circles) and of a lung protected from VILI (open circles). The plots represent the $^{18}$F-FDG activity in a region of interest ($C_{PET}$) normalized to the $^{18}$F-FDG activity in blood plasma ($C_{Plasma}$) versus the integral of plasma activity normalized to the plasma activity. Linear regression was performed for data assessed 15 min to 75 min after $^{18}$F-FDG injection. The slope of the linear regression line, a measure of $K_i$, is higher in the lung suffering from VILI compared to the lung protected from VILI. Reproduced and modified from (Musch et al., 2007).*

One assumption of the Patlak analyzis is that after an initial period of 10 to 15 min an equilibration between tracer concentration in plasma and extravascular compartment has been established. Therefore, after that initial period, the Patlak graph becomes linear and can be fitted by a linear equation depicted in Equation (1.3).

$$\frac{C_{PET}(t)}{C_{Plasma}(t)} = K_i * \frac{\int_{t=0}^{t} C_{Plasma}(\tau) * d\tau}{C_{Plasma}(t)} + V_{dist} \quad (1.3)$$

In this equation, $C_{PET}(t)$ and $C_{Plasma}(t)$ represent the $^{18}$F-FDG activity in lung tissue and blood plasma at each sample time point t, respectively, $\tau$ is the integration variable, $K_i$ represents the $^{18}$F-FDG net uptake rate calculated using the Patlak model and $V_{dist}$ represents the volume of distribution of $^{18}$F-FDG in both the extravascular compartment and in blood plasma. The volume of distribution is also called the initial distribution volume and is expressed in [ml blood / ml lung]. Consequently, in the Patlak model, the ordinate intercept at time $t = 0$ determines $V_{dist}$ and the slope of the linear regression line represents $K_i$ (de Prost et al., 2010). $K_i$ is a measure for the rate of $^{18}$F-FDG trapped per ml lung volume, including tissue and air filled alveolar space. Therefore, $K_i$ is not only affected by the regional metabolic activity, but also by differences in tissue contents, for instance due to differences in lung inflation.

The major advantages of the Patlak model are the relatively easy computational implementation and the robust estimation of the pulmonary uptake of $^{18}$F-FDG, even when edema accumulates in the lung (Dittrich et al., 2012).

**Sokoloff Three-Compartment Model**

The three compartment model analyzis developed by Sokoloff and coworkers was originally developed for the quantification of cerebral uptake of the tracer carbon-14-deoxyglucose in rats (Sokoloff et al., 1977). Later on Reivich and coworkers adapted the model for evaluation of $^{18}$F-FDG uptake in humans (Reivich et al., 1979). As compared to the Patlak analyzis, it provides more detailed information about individual steps of the $^{18}$F-FDG phosphorylation process. It includes the blood compartment, which serves as input function, and two tissue compartments. The extra-vascular substrate compartment is also called the precursor compartment and corresponds to the extra-vascular $^{18}$F-FDG available for phosphorylation. The metabolic compartment represents the amount of $^{18}$F-FDG-6-phosphate assumed to be irreversibly trapped in lung tissue. Therefore, the Sokoloff model describes the exchange of $^{18}$F-FDG between blood and tissue, as well as its phosphorylation in the tissues (Sokoloff et al., 1977).

It is assumed that the tracer rapidly equilibrates between the capillaries and the lung tissue such that the total measured tracer activity equals the total activity concentration in the tissue. Activity originating from the capillaries is negligible. Therefore, the total measured tracer activity concentration in a region of interest at time t ($C_{PET}(t)$) corresponds to the sum of the concentrations in the extravascular compartment ($C_e(t)$) and in the metabolic compartment ($C_m(t)$), (Equation (1.4)).

$$C_{PET}(t) = C_e(t) + C_m(t) \tag{1.4}$$

Rate constants $k_1$, $k_2$, and $k_3$ characterize the dynamics of the movement of $^{18}$F-FDG between the compartments (Figure 1.3) and are modeled using the linear differential equations (1.5) and (1.6).

$$\frac{dC_e(t)}{dt} = k_1 * C_{Plasma}(t) - (k_2 + k_3) * C_e(t) \tag{1.5}$$

$$\frac{dC_m(t)}{dt} = k_3 * C_e(t) \tag{1.6}$$

The net uptake rate of $^{18}$F-FDG from blood plasma to lung tissue can be computed according to Equation (1.7), using the individual transport parameters.

$$K_i = \frac{k_1 * k_3}{k_2 + k_3} \tag{1.7}$$

$K_i$ is a measure of the amount of $^{18}$F-FDG that is phosphorylated per assessed lung volume. However, the measured lung volume does not only consist of lung tissue (fractional tissue content, $F_{Tissue}$), but a certain fraction is occupied by blood vessels and air-filled alveolar space (Equation (1.8)).

$$F_{Tissue} = 1 - F_{Gas} - F_{Blood} \tag{1.8}$$

$F_{Blood}$ represents the fractional volume of pulmonary blood and can be obtained from the Sokoloff model.

Therefore, differences in lung inflation affect the measured tracer concentrations, in addition to the regional metabolic activity (Schroeder et al., 2011). The calculated net uptake rate of $^{18}$F-FDG has to be corrected for $F_{Tissue}$, computing the specific $K_i$ ($K_{iS}$) according to Equation (1.9).

$$K_{iS} = \frac{K_i}{F_{Tissue}} \tag{1.9}$$

The Sokoloff model is based on the assumption that all $^{18}$F-FDG molecules are present in the extra-vascular substrate compartment and available for metabolization. This assumptions, however, may not be valid in acutely injurious lungs featuring larger pools of edematous tissue that might allow $^{18}$F-FDG to leak nonspecifically into spaces functionally separate from cells trapping $^{18}$F-FDG (Schroeder et al., 2011).

**Four-Compartment Model**

Schroeder and coworkers developed a lung-specific four-compartment model that aims to describe the $^{18}$F-FDG kinetics in ARDS lungs by adding an extra-vascular, extra-cellular distribution volume exchanging $^{18}$F-FDG with the extra-vascular intra-cellular precursor compartment (Schroeder et al., 2008). This compartment accounts for the $^{18}$F-FDG-PET signal originating from extra-vascular volume that is not available for phosphorylation, like in edema fluid or alveolar flooding (Dittrich et al., 2012). Thus, at any given time, the total, regional activity of $^{18}$F-FDG assessed by dynamic PET imaging is assumed to be the sum of tracer activity in four functional compartments, illustrated in Figure 1.3.

## 1.3 Specific Aims and Hypotheses

The objective of this thesis was to use and advance PET/CT imaging techniques to study alterations in lung aeration, neutrophilic inflammation and perfusion in ARDS. Two interrelated studies were conducted, both of which used PET/CT.

The first study aimed to compare the relative contributions of volutrauma and atelectrauma to the pro-inflammatory response of the lung in a saline lung lavage model of ARDS in pigs. Recently, PET/CT has been used to assess the synergistic effects of volutrauma and atelectrauma on the inflammatory response of the lung (Musch et al. 2007; Borges et al., 2015). However, in those studies the extent of volutrauma and atelectrauma was potentially not the same. We therefore aimed to obtain information about the impact of volutrauma and atelectrauma at comparable low $V_T$ and low driving pressure (ΔP, defined as difference between peak airway pressure and PEEP) on the neutrophilic, pro-inflammatory response of the lung using $^{18}$F-FDG and PET/CT. In addition, we obtained information on lung aeration by performing CT and on lung perfusion by static PET of the distribution of $^{68}$Ga-labeled microspheres.

The main hypotheses of the study were:

1.1) Both volutrauma and atelectrauma increase lung mechanical stress and associated neutrophilic inflammation.
1.2) Atelectrauma damages especially the gravitational regions, whereas volutrauma injures particularly the gravitational non-dependent lung regions.
1.3) Volutrauma leads to higher pulmonary neutrophilic inflammation as compared to atelectrauma, at comparable low $V_T$ and ΔP, since static stress and strain are higher in the inflated than in the collapsed lungs.

The aim of the study on fluorescence-labeled microspheres derived perfusion measurements in ARDS was to validate the use of fluorescence-labeled microspheres for measurements of pulmonary perfusion distribution in acutely injured lungs. It has been shown previously that the use of fluorescence-labeled microspheres is an appropriate method to assess the distribution of pulmonary perfusion in healthy lungs (Glenny et al., 1993). However, whether the assumptions used for the analyzis of the distribution of fluorescence-labeled microspheres in healthy lungs are transferable to injured lungs has yet to be determined. We compared *ex vivo* measurements of the distribution of lung perfusion using fluorescence-labeled microspheres with *in vivo* measurements using $^{68}$Ga-labeled microspheres and PET/CT in ARDS lungs. We analyzed the extent to which excised lungs deformed during their extraction and subsequent processing. In addition, different algorithms for the analyzis of the distribution of the fluorescence-labeled microspheres were compared.

The main hypotheses of the study on fluorescence-labeled microspheres derived perfusion measurements in ARDS were:

2.1) Extraction of lungs and the associated changes of pressures as well as the subsequent drying at high pressure cause substantial lung deformation relative to the *in vivo* state.

2.2) The mass of lung tissue pieces featuring differing tissue volume is not an adequate surrogate for the extent of lung tissue in a sample. Consequently, as compared to the analyzis of non-injured lungs, differing algorithms have to be used for the analyzis of trapped fluorescent microspheres in ARDS lungs in order to adequately correct fluorescence measurements for lung tissue content.

2.3) The use of a modified algorithm for the analyzis of trapped fluorescence-labeled microspheres in ARDS lungs increases the agreement with *in vivo* PET/CT measurements of the distribution of lung perfusion using $^{68}$Ga-labeled microspheres.

2.4) The use of modified algorithms for the analyzis of fluorescence-labeled microspheres reduces the heterogeneity of pulmonary perfusion measurements.

# 2 Materials and Methods

This section is comprised of two sub-sections. In the first sub-section, which has been published as original article (Güldner et al., 2016), the materials and methods used to study the inflammatory impact of volutrauma and atelectrauma are presented. The Institutional Animal Care and Welfare Committee and the Government of the State of Saxony, Germany, approved all animal procedures of this study (protocol number 24-9168.11-1/2012-42). The study was supported by a grant of the MeDDrive Program, Medical Faculty Carl Gustav Carus, Dresden, Germany and by a grant from the German Research Council (Deutsche Forschungsgemeinschaft, DFG), Bonn, Germany (grant number GA 1256/7-1).

In the second sub-section, the materials and methods of the study on fluorescence-labeled microspheres derived perfusion measurements in ARDS are presented. Parts of this study have been published as original article (Güldner et al., 2014). All animal procedures of this study were approved by the Institutional Animal Care and Welfare Committee and the Government of the State of Saxony, Germany (protocol number 24-9168.11-1/2009-36). This study was supported by a grant from the German Research Council (Deutsche Forschungsgemeinschaft, DFG), Bonn, Germany (grant number GA 1256/6-1).

The PET/CT device used in both studies was a gift from the German Federal Ministry of Education and Research (BMBF contract 03ZIK42/ OncoRay), Bonn, Germany.

# 2.1 Volutrauma and Atelectrauma in ARDS

## 2.1.1 Experimental Protocol

The experimental protocol of this study was approved by the local animal care committee (Landesdirektion Dresden, Dresden, Germany). Ten juvenile pigs weighting 34.7 kg to 49.9 kg were studied. A randomized, parallel group design was used, where each group served as its own control. Figure 2.1 illustrates the time course of the experimental procedures.

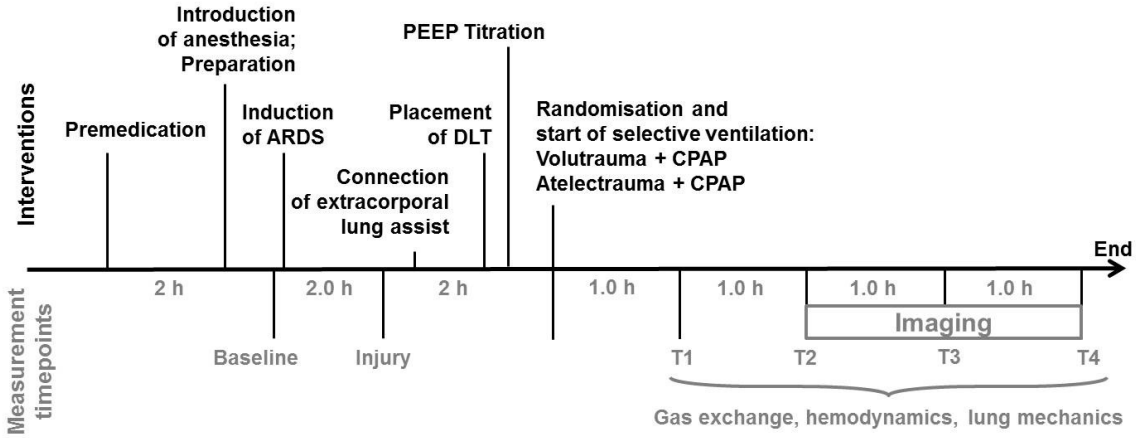


***Figure 2.1:*** *Time course of interventions during the study on volutrauma and atelectrauma in ARDS.*

After premedication, pigs were anesthetized, paralyzed, intubated and mechanically ventilated in supine position. After surgical preparation, the lungs were recruited with continuous positive airway pressure (CPAP) of 30 $cmH_2O$ for 30 sec, followed by 15 min of stabilization. Baseline measurements of hemodynamics, lung mechanics and gas exchange were collected (Baseline 1). Experimental ARDS was induced in both lungs by saline lavage (first hit of the double hit model) and measurements at the injury time point were performed (Injury). A pump-less interventional lung assist (Novalung GmbH, Heilbronn, Germany) was connected to the catheters in the femoral artery and vein, in order to support gas exchange and $CO_2$ removal extra corporeally. A modified right-sided double lumen tube was placed with the bronchial tip in the left main bronchus in order to separate the lungs. Two separate ventilators were connected in order to only ventilate the left lungs and to apply CPAP in the right lungs. After placement of the double lumen tube and following recruitment of both lungs for 30 sec at 30 $cmH_2O$, a PEEP titration was done in the left lungs in order to find the ventilator setting of the volutrauma and atelectrauma ventilator modes. After a further recruitment of the left lungs, the animals were randomly assigned to either the volutrauma or atelectrauma group, and injurious ventilation of the left lungs (second hit of the double

hit model) was started. The right lungs were not ventilated and served as within-animal control. During the following 4 h of mechanical ventilation of the left lungs in volutrauma or atelectrauma mode, parameters regarding lung mechanics, gas exchange and hemodynamics were recorded (time point T 1: 60 min after randomization until time point T 4: 4 h after randomization). During the last 2 h of injurious ventilation, lung imaging data were acquired using PET and $^{18}$F-FDG and $^{68}$Ga-labeled microspheres, respectively, as well as CT. At the end of the experiment, the anesthetic depth was increased with intravenous injection of thiopental (2 g) and animals were sacrificed by an intravenous injection of potassium chloride (1 mol, 50 ml). Lungs were excised and further processed for the following analyzis of molecular biology as well as for the determination of wet- to-dry ratios.

#### 2.1.1.1 Premedication, Anesthesia and Initial Ventilator Settings

Experimental subjects were premedicated with an intramuscular injection of 1 mg/kg midazolam und 10 mg/kg ketamine. An ear vein was punctured and intravenous anesthesia was induced with a bolus of 0.5 to 1 mg/kg Midazolam and 3 to 4 mg/kg ketamine. Anesthesia was maintained with continuous, intravenous injection of 1 to 2 mg/kg/h midazolam and 10 to 18 mg/kg/h ketamine. Muscle paralysis was induced with an intravenous bolus of 3 to 4 mg/kg atracurium, and maintained by continuous injection of 1 to 2 mg/kg/h atracurium. After premedication, experimental animals were intubated orally and mechanical ventilation of both lungs was started in volume controlled mode using a EVITA XL (Dräger Medical AG, Lübeck, Germany) and the following settings: $V_T$ of 8 mL/kg PBW, fraction of inspired oxygen ($FiO_2$) of 100 %, PEEP of 8 $cmH_2O$, time ratio of inspiration to exspiration (I:E) of 1:1, RR adjusted to achieve an arterial partial pressure of carbon dioxide ($PaCO_2$) between 35 and 45 mmHg, airway flow of 35 L/min. An intravenous infusion of a crystalloid solution (E153, Serumwerk Bernburg AG, Bernburg, Germany) at a rate of 10 to 20 mg/kg/h was used to maintain intravascular volume. Colloid solution (6 % hydroxyenthyl starch; Fresenius Kabi Deutschland GmbH, Bad Homburg, Germany) was administered as necessary to keep the hemoglobin concentration in the blood approximately constant. Animals were positioned supine during the entire experiment.

#### 2.1.1.2 Preparation

After premedication, experimental animals were intubated through tracheotomy using a cuffed, modified, right-sided double lumen tube (8.0 mm internal diameter, Mallinckrodt, Athlone, Ireland) with the bronchial tip placed in the left main bronchus. After surgical preparation of the right common carotid artery, an indwelling catheter was inserted and the mean pulmonary artery pressure was continuously monitored. The catheter in the arteria carotid was also used to take arterial blood samples and to measure the cardiac output (CO). The right external jugular vein was punctured and the Swan-Ganz pulmonary artery catheter (7.5 Fr., Opticath, Abbott, Abbott Park, USA) was inserted. Mean arterial pressure and pulmonary artery pressure were continuously monitored with a CMS Monitor (IntelliVue Patient Monitor MP 50, Philips AG, Böblingen, Germany). The pulmonary artery catheter was also used to take mixed-venous blood samples and to administer the $^{18}$F-FDG and the $^{68}$Ga-labeled microspheres during the imaging period. Two catheters (NovaPort one, Novalung GmbH, Heilbronn, Germany) were placed in the left femoral artery and right femoral vein. Each catheter was filled with 20 ml of normal saline solution containing 1000 IU Heparin and clamped until extra-corporeal gas exchange unit was connected. A catheter was inserted in the bladder to collect urine and to measure the intra-abdominal pressure.

#### 2.1.1.3 Induction of ARDS

Experimental ARDS was induced in both lungs according to the double hit model. The primary hit of both lungs was achieved by repetitive saline lung lavage using isotonic, body heated saline solution (6-12 lavages), as described by Lachmann and coworkers (Lachmann et al., 1980). To achieve a homogeneous distribution of the lavage fluid, the position of the animals was alternated between prone and supine every 2 lavages. This procedure was repeated until the criterion of the moderate ARDS ($PaO_2/FiO_2$ less than 200 mmHg) was reached after 30 min of stabilization (Ferguson et al., 2012). A second hit was induced in the left lungs by ventilating with injurious settings according to the study group for 4 h. The double-lumen tube allowed for isolated, injurious ventilation of the left lungs, while protecting the non-ventilated, control lungs from VILI.

#### 2.1.1.4 Ventilation Modes, Randomization and Start of the Selective Ventilation in Volutrauma or Atelectrauma

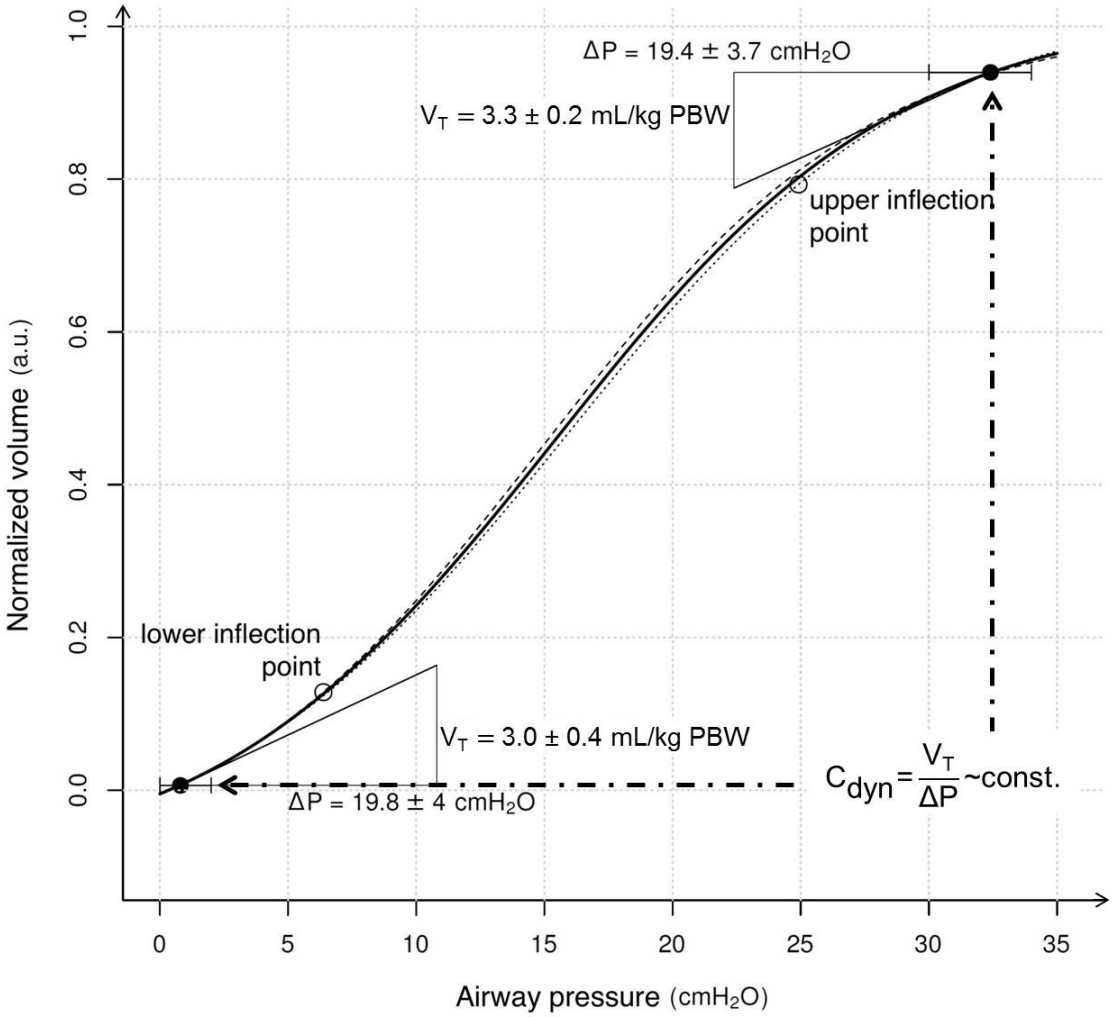


***Figure 2.2:*** *Recorded pressure-volume curve of the respiratory system during decremental PEEP trial averaged for each group (atelectrauma: dashed; volutrauma: dotted) and averaged over all experiments (black solid). Averaged selected PEEP values for each group (filled circles) and calculated points of maximal absolute curvature, i.e. upper and lower inflection point (open circles), are shown. Normalized volume (Vn) corresponds to Vn = (LV – FRC)/IC with lung volume (LV), functional residual capacity (FRC) and inspiratory capacity (IC), ΔP and $V_T$ are presented as mean ± standard deviation.*

A decremental PEEP trial was performed in the ventilated, VILI lungs during pressure controlled ventilation, keeping the following settings constant: $V_T$ of 3 mL/kg PBW, $FiO_2$ of 100 %, I:E of 1:1, and RR of 30 breaths per minute. The PEEP trial was started at 36 $cmH_2O$ to assure that the region of the pressure-volume curve of the respiratory system describing overdistension would be achieved. PEEP was reduced by steps of 2 $cmH_2O$ until zero, while every step was maintained for 2 min. Before every PEEP change, the dynamic compliance of the respiratory system, as measured by the ventilator, as well as the peak airway pressure ($P_{aw,peak}$) and ΔP were recorded. During the PEEP titration in the left lungs and until the end of the experiment, the right lungs were kept on a CPAP of 20 $cmH_2O$.

The PEEP settings during injurious ventilation of the left lungs of the volutrauma and atelectrauma groups, respectively, were defined according to measurements acquired during the PEEP trial. In volutrauma, the PEEP was set one step above the level where dynamic compliance had increased by more than 5 % compared to the previous value during the PEEP trial (Figure 2.2), in order to ensure complete lung recruitment and overdistension. In order to achieve comparable $V_T$ and ΔP in both groups, in atelectrauma, PEEP was adjusted at the opposite end of the pressure-volume curve of the respiratory system to achieve a dynamic compliance comparable to the one measured at volutrauma PEEP. From that compliance value, the ΔP was calculated for animals of the atelectrauma group.

After random assignment of the animals to either volutrauma or atelectrauma (n = 5 / group), the respective injurious ventilator settings were applied on the ventilated, VILI lungs for 4 h. In order to reset the lung history, the left lungs of animals assigned to volutrauma were initially recruited (CPAP of 40 $cmH_2O$ for 30 sec). The selective ventilation of the left lungs was performed using a SERVOi ventilator (Maquet, Rastatt, Germany), which was connected to the bronchial lumen of the double lumen tube. A second ventilator (EVITA XL Dräger Medical AG, Lübeck, Germany) was connected to the tracheal lumen of the double lumen tube in order to apply a CPAP of 20 $cmH_2O$ in the right lungs until the end of the experiment. Every 30 min a recruitment maneuver was performed to minimize right lung atelectasis. A pressure limit of 60 $cmH_2O$ was used to prevent barotrauma.

Simultaneously with the start of the injurious ventilation, the sweep gas flow through the extra-corporeal gas exchange unit was started. The flow was adjusted in order to keep $PaCO_2$ between 50 and 80 mmHg and arterial pH above 7.15. Maximal flow was limited to 15 L/min since gas exchange improves only marginally at higher values (Zhou et al., 2005). Breathing frequency was adjusted if $PaCO_2$ rose above 80 mmHg despite maximal sweep gas flow or if $PaCO_2$ fell below 50 mmHg in case sweep gas flow needed to be maintained due to severe hypoxemia. All other ventilator settings were kept constant in both groups until the end of the experiment.

#### 2.1.1.5 Assessment of Lung Mechanics, Gas Exchange and Hemodynamics

At time points shown in Figure 2.1, the parameters regarding respiratory mechanics, gas exchange and hemodynamic were acquired.

**Respiratory mechanics**

Airflow and RR were obtained from an internal sensor of the mechanical ventilator. $P_{aw}$ was assessed for each lung separately using pressure transducers (163PC01D48-PCB, Sensortechnics GmbH, Germany), having the tip placed next to the tracheal tube. Signals were digitized at 180 to 200 Hz using an analog-digital board (DAQ-Pad 1200; National Instruments, Austin, TX) and acquired by a laptop using a data acquisition system written for LabVIEW™ environment (National Instruments, Austin, TX). The dynamic compliance of the respiratory system was obtained by the mechanical ventilator.

**Gas exchange**

Arterial and mixed venous blood samples were analyzed for arterial pH, arterial partial pressure of oxygen ($PaO_2$), and $PaCO_2$ using a blood gas analyzer (ABL 505, Radiometer, Copenhagen, Denmark).

**Hemodynamics**

Mean arterial pressure and mean pulmonary artery pressures were measured continuously using a CMS Monitor (Compound Monitor System CMS, IntelliVue Patient Monitor MP 50, Philips AG, Böblingen, Germany). CO was assessed using the thermodilution method, averaging three measurements equally spread over the respiratory cycle and using 10 ml 0.9 % saline solution at room temperature.

#### 2.1.1.6 Lung Imaging Protocol

Imaging data of lung aeration, perfusion, and neutrophilic inflammation were acquired during the last 2 h of the injurious ventilation of the left lungs. The time course of the acquisition of the imaging data is shown in Figure 2.3. For all scans, animals were positioned supine in the PET/CT camera (Biograph16 Hirez PET/CT, Siemens, Knoxville, TN, USA).

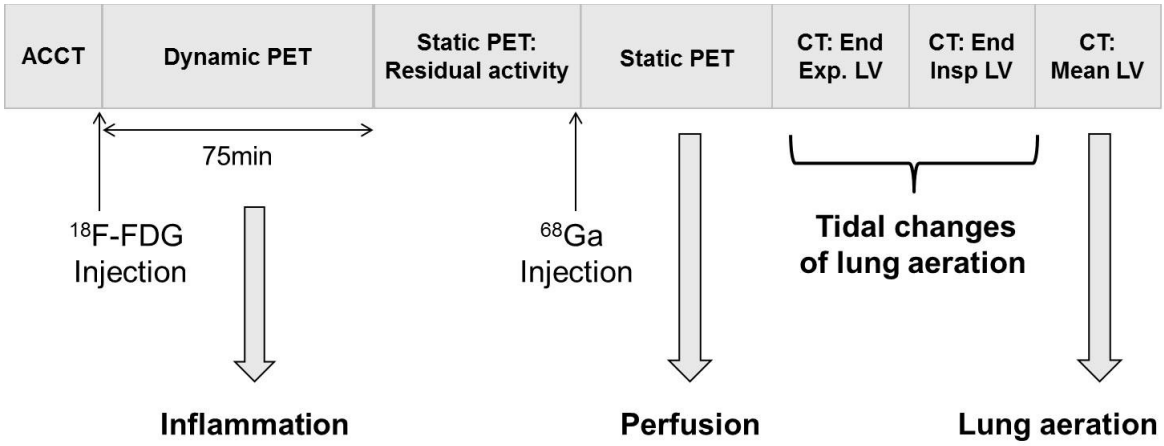


***Figure 2.3:*** *Lung imaging protocol.*

Following low dose helical CT scans used for attenuation correction of the following dynamic PET scans (attenuation correction CT, ACCT), $^{18}$F-FDG (179 MBq – 216 MBq) was injected intravenously at a constant rate over 60 s via the pulmonary artery catheter, as depicted in Figure 2.4. Simultaneous with the beginning of the infusion, the acquisition of a 75 min image sequence consisting of 32 sequential PET frames (6x30”, 7x60”, 15x120”, 1x300”, 3x600”) was started. Pulmonary arterial blood was sampled at each mean frame time point (12x15”, 4x30”, 5x60”, 11x300”, 75’) in the pulmonary artery (Figure 2.4). The blood samples were centrifuged (5000 rpm, 5 min) and 1.0 ml blood plasma was pipetted. The concentration of $^{18}$F-FDG in each blood plasma sample was measured in a gamma counter cross-calibrated with the PET scanner (Musch et al., 2007). To reduce artifacts due to motion of the diaphragm, the field of view was positioned such that the most caudal slice was adjacent to the diaphragm dome. The camera collected transverse slices of 2 mm thickness over a 15 cm cranio-caudal field. PET images were reconstructed iteratively (ordered subset expectation maximization, 6 iterations, 4 subsets, post-filtering Gauss 5 mm) with correction for scatter and attenuation effects. Images were decay corrected to the beginning of tracer injection. Each frame yielded a 168 x 168 x 82 matrix with a voxel size of 2.03 x 2.03 x 2 mm$^3$.

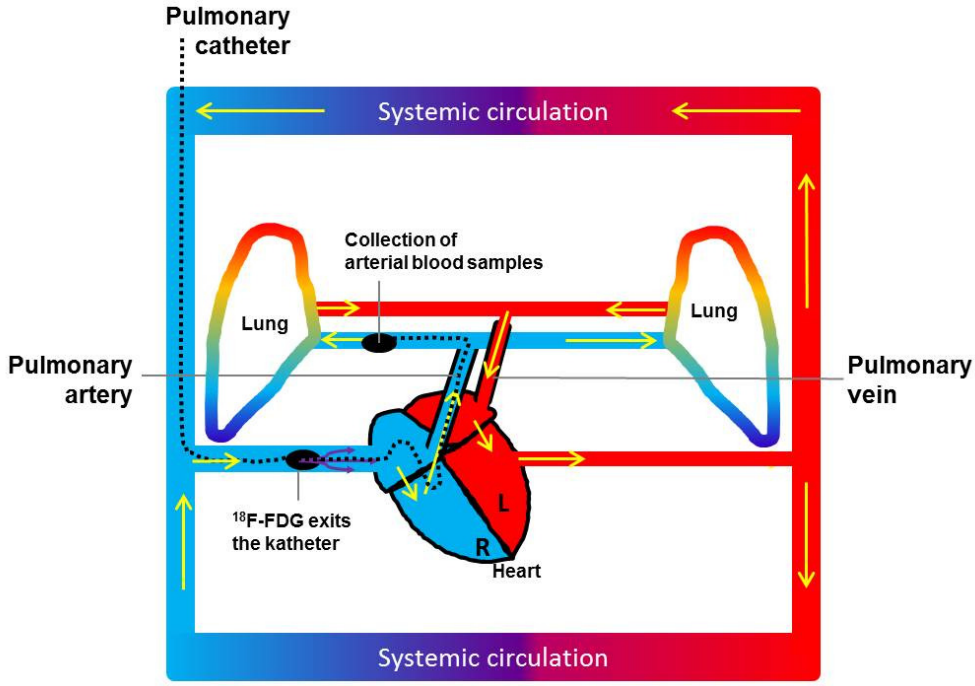


***Figure 2.4:*** *Position of the pulmonary artery catheter, via which $^{18}$F-FDG was injected at the proximal end and via which the arterial blood samples were collected at the distance end.*

Before perfusion scans were acquired, the remaining level of $^{18}$F-FDG activity within the lungs was measured by static PET scanning. For preparation of $^{68}$Ga-labeled microspheres, $^{68}$Ga was produced using a germanium-68/gallium-68 generator (ITG Isotope Technologies Garching GmbH, Germany), eluted in 7 ml 0.05 M HCl, purified, and concentrated using a cation-exchanger (STRATA-XC, Phenomenex, Aschaffenburg, Germany). For labeling, approximately 450 MBq of the $^{68}$Ga elute was transferred into a microsphere B20 kit (Rotop Pharmaka GmbH, Dresden, Germany). $^{68}$Ga-labeled microspheres (86 MBq - 130 MBq) were injected intravenously and manually as a slow bolus over approximately 1 min followed by a flush with saline solution. The distribution of the $^{68}$Ga-labeled microspheres in the pulmonary capillary bed was assessed by static PET scanning of the whole lungs. Image reconstruction was carried out iteratively (ordered subset expectation maximization, 6 iterations, 4 subsets, post-filtering Gauss 5 mm) with attenuation correction using the CT scans at mean lung volume. The voxel size of the perfusion scans was 2.03 x 2.03 x 2 mm$^3$ yielding a 168 x 168 x 198 matrix. Helical CT scans of the chest were acquired during muscle paralysis and CPAP in the ventilated, VILI lungs at end-inspiratory and end-expiratory pressure levels as well as on a pressure level corresponding to mean lung volume. The CT scanner was set as follows: collimation of 16 × 0.75 mm, pitch of 1.35, bed speed of 38.6 mm/s, voltage of 120 kV and tube current-time product of 120 mAs. CT images were reconstructed using a B70f convolution kernel and 1.0 mm slice thickness, yielding matrices with 512 x 512 pixel with a size of 0.426 × 0.426 mm$^2$.

#### 2.1.1.7 *Ex vivo* Analysis: Molecular Biology and Wet- To- Dry Ratio

After organ extraction, lung tissue samples of ventral, central, and dorsal parts of the left and right upper lobes were further processed for the analyzis of molecular biology and the estimation of wet- to- dry weight ratios.

**Molecular Biology**

The samples were snap frozen in liquid nitrogen and storage at -80 °C. Tissue probes were grounded to powder using liquid nitrogen. Conventionally available enzyme linked immuno-sorbent assay kits (R&D Systems) were used for protein analyzis. The protein concentrations of IL-6, IL-8 und TNF-α were determined.

**Wet- To- Dry Ratio**

Tissue blocks of approximately 1 x 1 x 1 $cm^3$ were sampled. The tissue blocks were weighted in wet state. Thereafter, they were dried using a microwave (30 min at 120 W) and weighted in dry state. After drying the samples for a second time (microwave: 5 min at 120 W) they were weighted again. If the weight before and after the second drying process differed by more than 5 %, the drying of the samples was repeated (microwave: 5 min at 120 W) until the deviation compared to the previous measurement was less than 5 %. The weight-ratio was calculated as the weight of the wet tissue blocks measured shortly after lung extraction relative to the weight of the lung blocks after their drying.

## 2.1.2 Data Processing and Analysis

### 2.1.2.1 Analysis of Respiratory Mechanics Variables

The respiratory volume signal was estimated from the 5 min recordings of the airflow signal by numerical integration for each measurement time point. The time point of the beginning of inspiration and expiration, respectively, were detected from the airflow signal using a zero crossing algorithm. For each respiratory cycle, $V_T$ was computed as the difference between the minimum and maximum value of the respiratory volume signal. Minute ventilation (MV) was computed as RR multiplied by $V_T$. For each measurement time point, mean airway pressure ($P_{aw,mean}$), PEEP, and $P_{aw,peak}$ were calculated for each respiratory cycle as average, minimum, and maximum value of the $P_{aw}$ signal, respectively, and averaged over all respiratory cycles of the 5 min recordings. Resistance and elastance of the respiratory system ($R_{rs}$ and $E_{rs}$, respectively) were calculated from 5 min acquisitions of airflow and $P_{aw}$ signals using a volume-dependent, first-order model of respiratory mechanics shown in Equation (2.1), (Avanzolini et al., 1997).

$$P_{aw}(t) = R_{rs} * \dot{V}(t) + (E_1 + E_2 * V(t)) * V(t) + P_0 \tag{2.1}$$

In this equation, V represents volume, $\dot{V}$ is airflow, *t* is time, $P_0$ represents residual airway pressure at the end-expiratory lung volume (≈ PEEP), and $E_1$ and $E_2$ are the volume-independent and volume-dependent components of $E_{rs}$, respectively.

The distension index percentage $E_2$ ($\%E_2$) was computed according to Equation (2.2).

$$\%E_2(t) = 100 * \frac{E_2 * V(t)}{E_1 + E_2 * V(t)} \tag{2.2}$$

Mechanical power at measurement time point T 4 expressed in Joule per minute was calculated for each animal according Equation (2.3), (Gattinoni et al., 2016).

$$Power_{rs} = 0.098 * RR * \left\{ V_T{}^2 * \left[ \frac{1}{2} * E_{rs} + RR * \frac{(1 + I:E)}{60 * I:E} * R_{rs} \right] + V_T * PEEP \right\} \tag{2.3}$$

For each animal, regional “intensity” was calculated as mechanical power normalized to the mean mass of the open, ventilated, VILI lung (see chapter 2.1.2.3 for explanation of the calculation of mass) according to (Samary et al., 2016).

### 2.1.2.2 Definition of Lung Fields for Analysis of Imaging Data

For the analyzis of lung perfusion, CT scans at mean lung volume were coregistrated to the static $^{68}$Ga-PET scans using the software Rover (ABX advanced & biochemical compounds GmbH, 2015), (Hofheinz et al., 2012). Coregistrated CT scans were used for manual segmentation of volumetric masks of the ventilated, VILI lungs and of the non-ventilated, control lungs, respectively. Segmentation was done using the software ITK-Snap (Yushkevich et al., 2006). The trachea, main bronchi, and associated blood vessels were excluded from lung masks. Regions outside the lung masks were excluded from further analyzis. The ventilated, VILI lungs and the non-ventilated, control lungs were divided in 5 isogravimetric subregions reaching from ventral to dorsal. The subdivision was done using the coregistrated CT scans at mean lung volume and by analyzing the mass of all voxel within the lung masks (see chapter 2.1.2.3 for explanation of the calculation of mass). For the analyzis of the dynamic PET scans, ACCT scans were coregistrated to the dynamic PET scans. Coregistrated ACCT scans were used for manual segmentation of volumetric masks of the assessed 15 cm cranio-caudal part of the ventilated, VILI lungs and of the non-ventilated, control lungs, respectively. Lung masks were refined manually in order to exclude partial volume effects near lung edges and the heart. For the analyzis of the dynamic PET scans, the assessed part of the ventilated, VILI and the non-ventilated, control lungs, respectively, were divided in 5 isogravimetric regions of interest (ROIs) along the ventro-dorsal axis using the coregistrated ACCT scans (Figure 2.5). After coregistration of the end-inspiratory and end-expiratory CT scans to the dynamic PET scans, the same ROIs of the 15 cm cranio-caudal field of view were used to determine tidal changes of lung aeration.

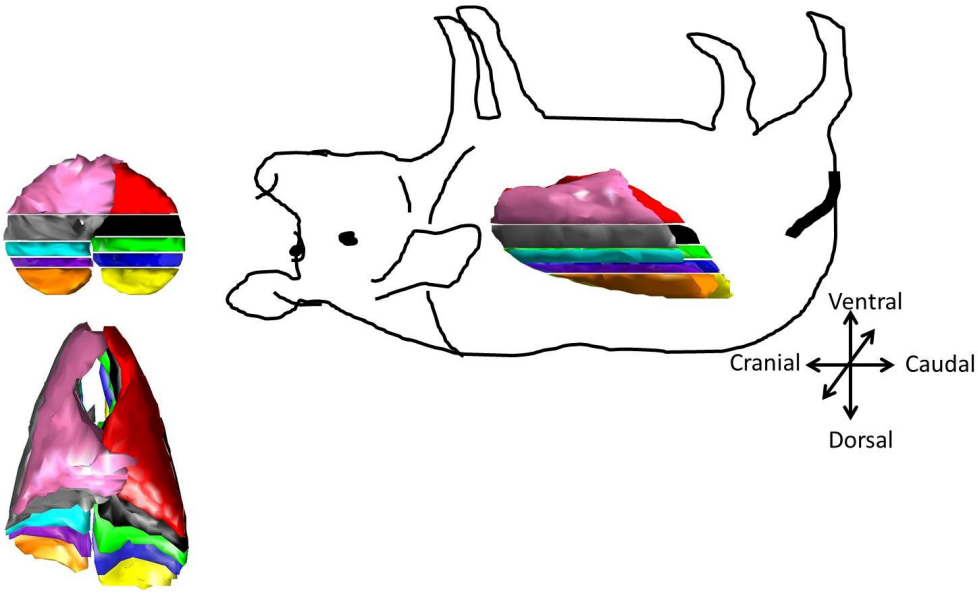


***Figure 2.5:*** *ROIs defined for the analyzis of the regional distribution of lung perfusion. After manual segmentation of the ventilated, VILI lungs and non-ventilated, control lungs, respectively, lungs were divided in 5 isogravimetric subregions along the ventro-dorsal axis.*

#### 2.1.2.3 Analysis of CT scans for quantification of lung aeration

The CT scans at mean lung volume were used for the determination of the total volume of the ventilated, VILI and non-ventilated, control lungs, respectively. **Total volume** was calculated by multiplying of the number of pixel determining the lungs by the square pixel size and the slice thickness.

The CT scans at mean lung volume were used for the determination of the total weight of the ventilated, VILI and non-ventilated, control lungs, respectively. The CT scans at end-expiration coregistrated to $^{18}$F-FDG-PET scans were analyzed for the mass of the captured lung parts as well as for lung mass per ROI. For the calculation of **lung mass**, the mean CT number of each lung region was used as surrogate for its density and multiplied by the volume of the region (Gattinoni, Pesenti, Avalli, et al., 1987).

The CT scans at mean lung volume were used to assess the **average degree of aeration** during a breathing cycle. For the ventilated, VILI and non-ventilated, control lungs, respectively, 4 degrees of lung aeration were distinguished based on previously described thresholds (Puybasset et al., 2000): ranges of -1000 HU to -900 HU, -900 HU to -500 HU, -500 HU to -100 HU, and -100 HU to +100 HU were used to define the hyper-aerated, normally aerated, poorly aerated, and non-aerated compartments, respectively.

The CT scans at mean lung volume were used to calculate the **mass of the open, ventilated, VILI lungs**, estimated as sum of the mass of hyper, normally, and poorly aerated compartments.

The CT scans at end-expiration and end-inspiration were used to determine **tidal changes of lung, aeration**. For all 5 isogravimetric subregions of the 15 cm cranio-caudal section of the ventilated, VILI and non-ventilated, control lungs, respectively, aeration compartments were computed. Tidal recruitment was calculated as difference in the size of the non-aerated compartment between end-expiration and end-inspiration. Tidal hyper-aeration was calculated as difference in the size of the hyper-aerated compartment between end-inspiration and end-expiration (Malbouisson et al., 2001).

.

#### 2.1.2.4 Analysis of $^{68}$Ga-PET Scans for Quantification of Lung Perfusion

The $^{68}$Ga net activity ($^{68}$Ga-PET$_{net}$) of the images was calculated by subtraction of the residual background radioactivity of $^{18}$F-FDG, taking the decay half-lives of $^{18}$F and $^{68}$Ga into account. Absolute lung perfusion ($Q_{abs}$) was calculated for the ventilated, VILI and non-ventilated, control lungs, respectively, as well as for 5 isogravimetric sub-regions along the ventro-dorsal axis according to Equation (2.4).

$$Q_{abs} = \frac{^{68}\text{Ga} - \text{PET}_{net,ROI}}{^{68}\text{Ga} - \text{PET}_{net,TOTAL}} \times CO \qquad (2.4)$$

In this equation, $^{68}$Ga-PET$_{net,ROI}$ represents the $^{68}$Ga-PET$_{net}$ inside the ROI, $^{68}$Ga-PET$_{net,TOTAL}$ represents the total $^{68}$Ga-PET$_{net}$ activity within the whole lung.

#### 2.1.2.5 Analysis of $^{18}$F-FDG-PET Scans for Quantification of Pulmonary Neutrophilic Inflammation

The ACCT images coregistrated to the dynamic PET scans were used to calculate $F_{Gas}$ of each voxel. For each voxel as well as for all ROIs, $F_{Gas}$ was calculated as average CT number divided by -1000. For each ROI, as well as for the ventilated, VILI and non-ventilated, control lungs, the $^{18}$F-FDG kinetics were analyzed using the Sokoloff three-compartment model, yielding $K_i$ and $F_{Blood}$. $K_{iS}$ was calculated as explained in chapter 1.2.7.2. in order to account for differences in lung inflation and blood volume between ROIs, lungs, and animals. For graphical illustration, $K_i$ was also calculated for each voxel according to the Patlak model and normalized to $F_{Tissue}$.

### 2.1.3 Statistics

The calculation of the sample size (number of animal experiments) was needed to test the hypothesis that 'volutrauma causes a comparable inflammatory response of the lung'. It was done based on results of pilot experiments and on results of another research group (Hotchkiss et al., 2000). Correspondingly we assumed that a sample size of 5 animals per group would provide the appropriate power (inferential statistical parameter: significance values $\alpha = 0.05$, power $1 - \beta = 0.80$) to achieve significant difference of $K_{iS}$ between volutrauma and atelectrauma within a two-armed, randomized trial. The sample size calculation was based on an effect size of $d = 2.25$. It was done using the software G-Power (Version 3.1.2, University of Düsseldorf, Germany, Institut für Experimentelle Psychologie). Data are presented as median and [25 % and 75 % quantile] if not stated otherwise.

Due to the small sample size, statistical analyzes were done using non-parametric statistical tests. Differences between the ventilated, VILI and the non-ventilated, control lungs within the same animal were tested using Wilcoxon signed rank tests for matched pairs. Adjustments for repeated measurements were done according to the Sidak procedure. Differences between the groups were tested using Mann-Whitney U tests. Parameters regarding lung mechanics, hemodynamics, and gas exchange were analyzed as following: comparability of groups at Baseline 1 and Injury time point as well as $V_T$ and $\Delta P$ after the PEEP trial were tested using an unpaired t-test, while differences among groups after randomization were tested using general linear model statistics and using Injury as covariate.

Statistical analyzes were done using the software SPSS (Version 23.0, SPSS Inc., Chicago, USA). Statistical significance was set at a p-value $\leq 0.05$.

# 2.2 Fluorescence-Labeled Microspheres Derived Perfusion Measurements in ARDS

## 2.2.1 Experimental Protocol

The experimental protocol of this study was approved by the local animal care committee (Landesdirektion Dresden, Dresden, Germany). The data of this study were obtained from an already published experiment (Güldner et al., 2014). Briefly, twelve juvenile pigs weighting 26 to 40 kg were studied, but only the data of seven pigs were used in this substudy. A randomized, 4 × 4 (therapies × animals) Latin square group design was used. Figure 2.6 illustrates the time course of the experimental procedures.

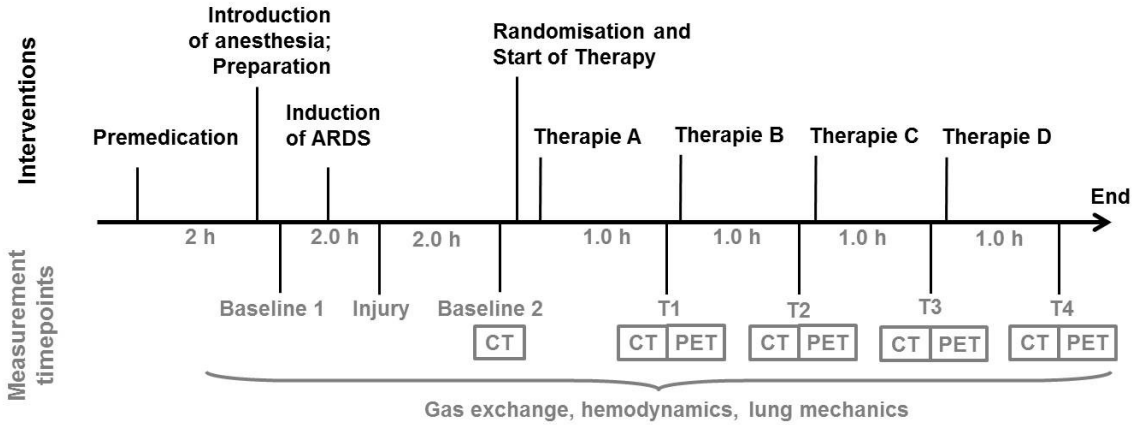


***Figure 2.6:*** *Time course of interventions of the study on fluorescence-labeled microspheres derived perfusion measurements in ARDS.*

After premedication, pigs were anesthetized, intubated, and mechanically ventilated in supine position. After the start of ventilation in volume controlled mode and surgical preparation, the lungs were recruited with an inspiratory pressure of 30 $cmH_2O$ for 30 s in CPAP mode to reset the lung history. Animals were allowed to stabilize for 15 min and baseline measurements of hemodynamics, lung mechanics and gas exchange were collected (Baseline 1). Experimental ARDS was induced by repetitive saline lung lavage and measurements were repeated (Injury). Mechanical ventilation mode was switched to biphasic positive airway pressure/ airway pressure release ventilation (BIPAP/APRV). After 30 min of stabilization measurements were recorded and lung aeration was quantified by CT scanning (Baseline 2). Thereafter, muscle paralysis was ended to resume spontaneous breathing. Animals were randomly assigned to one of four experimental groups, which differed in the order of four different levels of contribution of spontaneous breathing (SB) to the total MV during ventilation in BIPAP/APRV mode. To minimize carryover effects, a derecruitment maneuver was performed before each sequence. Animals were ventilated at each level of SB for 1 h. At the end of each

sequence (time point T 1 at the end of sequence 1, until time point T 4 at the end of sequence 4), parameters regarding lung mechanics, gas exchange, and hemodynamics were recorded. At the end of each sequence, fluorescence-labeled microspheres (FluoSpheres, LifeTechnology) were injected intravenously over 60 s for *ex vivo* measurements of lung perfusion. At the same time, $^{68}$Ga-labeled microspheres were injected intravenously over 60 s and immediately thereafter lung imaging data were acquired.

At the end of the experiment, the anesthetic depth was increased with intravenous injection of thiopental (2 g) and animals were sacrificed by an intravenous injection of potassium chloride (1 mole, 50 ml). The left and right lungs were excised and further processed for the analyzis of the fluorescence-labeled microspheres.

#### 2.2.1.1 Premedication, Anesthesia and Initial Ventilator Settings

Pigs were premedicated with an intramuscular injection of 1 mg/kg midazolam and 10 mg/kg ketamine. An ear vein was punctured and intravenous anesthesia was induced with a bolus of 0.5 to 1 mg/kg Midazolam and 3 to 4 mg/kg ketamine. Anesthesia was maintained with continuous, intravenous injection of 1 to 2 mg/kg/h midazolam and 10 to 18 mg/kg/h ketamine. Muscle paralysis was induced with an intravenous bolus of 3 to 4 mg/kg atracurium, and maintained by continuous injection of 1 to 2 mg/kg/h atracurium. After premedication, animals were intubated orally with a cuffed endotracheal tube and ventilated with a mechanical ventilator EVITA XL (Dräger Medical AG, Lübeck, Germany) in volume controlled mode with the following settings: $FiO_2$ of 100 %, $V_T$ of 10 mL/kg PBW, PEEP of 5 $cmH_2O$, I:E of 1:1, and inspiratory airway flow of 35 L/min. RR was titrated to achieve a $PaCO_2$ of 35 to 45 mmHg. An intravenous infusion of a crystalloid solution (E153, Serumwerk Bernburg AG, Bernburg, Germany) at a rate of 10 to 15 mg/kg/h was used to maintain intravascular volume. Animals were positioned supine during the entire experiment.

#### 2.2.1.2 Preparation

After premedication, experimental animals were intubated orotracheally using a cuffed, endotracheal tube (8.0 mm internal diameter, Mallinckrodt, Athlone, Ireland). After surgical preparation of the right common carotid artery, an indwelling catheter was inserted and the mean arterial pressure, blood pressure, temperature und heart rate were continuously monitored using a CMS monitor (IntelliVue Patient Monitor MP 50 Philips, Böblingen, Germany). The right external jugular vein was punctured and the Swan-Ganz pulmonary artery catheter (7.5 Fr., Opticath, Abbott, Abbott Park, USA) was inserted via the vena cava superior into the arteria pulmonary artery. Mean pulmonary artery pressure and CO were continuously monitored using a pressure transducer (PMSET 1DT-XX) connected a CMS Monitor (IntelliVue Patient Monitor MP 50, Philips AG, Böblingen, Germany). The pulmonary artery catheter was also used to administer the $^{68}$Ga-labeled microspheres and the fluorescence-labeled microspheres during the imaging period. Urine was collected with a catheter inserted into the bladder. An balloon catheter (Erich Jaeger, Höchberg, Germany) was placed in the esophagus for measurements of the intrathoracic pressure and the position was verified according to the method of Lanteri and coworkers (Lanteri et al., 1994).

#### 2.2.1.3 Induction of ARDS

Experimental ARDS was induced by repetitive lung lavage with warm (38 °C) 0.9 % saline solution as described by Lachmann and coworkers (Lachmann et al., 1980). To achieve a homogeneous distribution of the lavage fluid, the position of the animals was alternated between prone and supine every 2 lavages. Saline lung lavage was repeated until the criterion of the moderate ARDS ($PaO_2/FiO_2$ < 200 mmHg) was reached after 30 min of stabilization (Ferguson et al., 2012).

#### 2.2.1.4 Randomization and Start of the Selective Ventilation with Different Spontaneous Breathing Contributions

After induction of ARDS and before measurements at time point Baseline 2, mechanical ventilation mode was switched to BIPAP/APRV and using the following settings: fraction of inspired oxygen of 0.5, ΔP gradient amounting to a $V_T$ of 6 mL/kg PBW, PEEP of 10 $cmH_2O$, I:E of 1:1, and RR adjusted to achieve an arterial pH between 7.30 and 7.45.

Thereafter, muscle paralysis was ended to resume spontaneous breathing. Animals were randomly assigned to one of the four experimental groups, which differed according to the level of contribution of SB to the total MV during BIPAP/APRV (60 min each, crossover design):

(A) 0 % SB (BIPAP/APRV 0%);
(B) Greater than 0 % to 30 % SB (BIPAP/APRV > 0 – 30%);
(C) Greater than 30 % to 60 % SB (BIPAP/APRV > 30 – 60%);
(D) Greater than 60 % SB (BIPAP/APRV >60%).

In each phase, the mandatory rate of BIPAP/APRV was adjusted by changing the inspiratory and the expiratory times in the same proportion, while keeping the other mechanical ventilator settings constant. To avoid predominance of any particular level of contribution of SB to the total MV, the sequences of SB levels were defined according to a specific 4 × 4 (therapies × animals) Latin square. The following sequences were used:

1. Sequence: A B C D > 0 % – 30 % / > 30 % – 60 % / > 60 % / 0 % level of SB
2. Sequence: B A D C > 30 % – 60 % / > 0 % – 30 % / 0 % / > 60 % level of SB
3. Sequence: C D B A > 60 % / 0 % / > 30 % – 60 % / > 0 % – 30 % level of SB
4. Sequence: D C A B 0 % / > 60 % / > 0 % – 30 % / > 30 % – 60 % level of SB

Every sequence was applied in 3 animals. To minimize carryover effects, the order of the sequences varied and a derecruitment maneuver consisting of 15 s of disconnection from the ventilator was performed before each level of SB. Before the disconnection, an intravenous bolus of 0.3 mg/kg of atracurium was given to suppress SB. The derecruitment maneuver was considered stable if the global impedance measured by electrical impedance tomography varied less than 5 % during the last 5 s. After that, the electrical impedance tomography belt was removed to avoid interference with CT measurements. If level B, C, or D followed in the randomized sequence, SB was resumed within 15 min after reconnection to the ventilator. During BIPAP/APRV 0% (level A), atracurium was infused at 1 to 2 mg/kg/h to suppress SB. Infusion rates of midazolam and ketamine remained unchanged.

In this substudy, only perfusion measurements at the end of the BIPAP/APRV 0% and BIPAP/APRV >60% period were analyzed, since perfusion distribution along the cranio-caudal and ventro-dorsal axes as well as total gas volume of the whole lung and lung aeration differed most between those two levels of SB (Güldner et al., 2014).

#### 2.2.1.5 Assessment of Lung Mechanics, Gas Exchange and Hemodynamics

At every time point shown in Figure 2.6, parameters regarding respiratory mechanics, gas exchange and hemodynamics were acquired:

**Respiratory mechanics**

Airflow and RR were obtained from an internal sensor of the mechanical ventilator. $P_{aw}$ was assessed using pressure transducers (163PC01D48-PCB, Sensortechnics GmbH, Germany), having the tip placed next to the tracheal tube. Respiratory signals were digitized at 200 Hz using an analog-digital board (NI USB-6210; National Instruments, Austin, TX) and acquired by a laptop using a data acquisition system. An esophageal balloon catheter was connected to a pressure transducer (163PC01D48-PCB; Sensortechnics GmbH) to measure the esophageal pressure.

**Gas exchange**

Arterial and mixed venous blood samples were analyzed for arterial pH, $PaO_2$, and $PaCO_2$ using a blood gas analyzer (ABL 505, Radiometer, Copenhagen, Denmark). Oxygen saturation and hemoglobin concentration were assessed using an OSM 3 Hemoximeter (Radiometer), which was calibrated for porcine blood.

**Hemodynamics**

Mean arterial pressure and mean pulmonary artery pressure was measured continuously using a CMS Monitor (Compound Monitor System CMS, IntelliVue Patient Monitor MP 50, Philips AG, Böblingen, Germany). CO was assessed using the thermodilution method, averaging three measurements equally spread over the respiratory cycle and using 10 ml 0.9 % saline solution at room temperature.

#### 2.2.1.6 Lung Imaging Protocol

For all scans, animals were positioned supine in the PET/CT camera (Biograph16 Hirez PET/CT, Siemens, Knoxville, TN, USA). ACCT scans (120 kVp, CareDose) were acquired for attenuation correction of the following static PET scans. Thereafter, preliminary PET scans of the whole lung were acquired at the end of each sequence to detect residual radioactivity of previous $^{68}$Ga-PET scans ($^{68}$Ga-PET$_{before}$). For preparation of $^{68}$Ga-labeled microspheres, $^{68}$Ga was produced using a germanium-68/gallium-68 generator (ITG Isotope Technologies Garching GmbH, Germany), eluted in 7 ml 0.05 M HCl, purified, and concentrated using a cation-exchanger (STRATA-XC, Phenomenex, Aschaffenburg, Germany). For labeling, approximately 450 MBq of the $^{68}$Ga elute was transferred into a microsphere B20 kit (Rotop Pharmaka GmbH, Dresden, Germany). $^{68}$Ga-labeled microspheres were injected intravenously and manually as a slow bolus over approximately 1 min followed by a flush with saline solution. The injected $^{68}$Ga activities were increased prior to each scan (mean values: Baseline 2: 6 MBq; time point T 1: 9 Bq; T 2: 17 MBq; T 3: 37 MBq; T 4: 65 MBq). Static PET scans were obtained ($^{68}$Ga-PET$_{after}$). The imaging protocol was repeated for data aquisition at every time point. Static PET scans were reconstructed iteratively (ordered subset expectation maximization, 6 iterations, 4 subsets, post-filtering Gauss 5 mm) with attenuation correction using the ACCT scans. The resulting voxel size of the static PET scans was 4.06 x 4.06 x 5 mm³ yielding matrices with 168 x 168 x 79 voxel.

At time point Baseline 2 as well as after each static PET scan at the end of each ventilation sequence, helical CT scans of the chest were acquired during muscle paralysis and CPAP at end-expiratory pressure levels. The CT scanner was set as follows: collimation of 16 × 0.75 mm, pitch of 1.35, bed speed of 38.6 mm/s, voltage of 120 kV and tube current-time product of 120 mAs. CT images were reconstructed using a B70f convolution kernel and 1.0 mm slice thickness, yielding matrices with 512 x 512 pixel with a size of 0.426 x 0.426 mm$^2$.

#### 2.2.1.7 Preparation and Administration of Fluorescence-Labeled Microspheres

Fluorescence-labeled microspheres were prepared and administered as described in detail in (Glenny et al., 1991). Briefly, fluorescent albumin microspheres of 6 different colors (red, yellow-green, crimson, blue-green, orange, and scarlet) and 15 µm diameter (Molecular Probes, Eugene, Oregon, USA) were dissolved in sodium chloride (Vortex, IKA Works Inc., Wilmington NC, USA). At time point Baseline 2 and at the end of each sequence of SB, approximately 1.5 * $10^6$ microspheres of one color were injected intravenously via the pulmonary artery catheter over a period of 1 min followed by a flush with saline solution. In each experiment, the order of the fluorescence color was randomly varied across animals in order to negate an effect of order.

#### 2.2.1.8 *Ex vivo* Processing of the Lung for Analysis of Fluorescence-Labeled Microspheres

After animals were sacrificed, the thorax was opened, lungs were removed from the chest and flushed with 50 mL/kg PBW 6 % hydroxyethyl starch (Fresenius Kabi, Bad Homburg) until they were clear of blood. Lungs were air dried for 7 d with continuous positive pressure of 25 $cmH_2O$. When dry, all of the 12 analyzed whole lungs were first coated with one-component polyurethane foam (BTI Befestigungstechnik, Ingelfingen, Germany), then suspended vertically in a square box and embedding in two-component polyurethane foam (HR-AT, Vosschemie GmbH, Uetersen, Germany). The created lung-foam-blocks were cut into slices of approximately 1.2 cm thickness. The slices were then cut into pieces of 12 x 12 x 12 $mm^3$ size using a rigid grid system. Each of the resulting lung tissue piece was weighed, giving the mass (m), and was assigned a three-dimensional coordinate. Lung pieces were graded in respect to their airway and vessel contents. The higher the proportion of airways and vessels, the higher the score was ranked (score range: 0 - 3). Lung pieces were soaked in 2 ml of 2-ethoxyethyl acetate (Aldrich Chemical, Milwaukee, WI) for 7 d to extract the fluorescence dye out of the lung tissue. Considering the specific excitation and emission wavelength of the fluorescence colors (Table 2.1), the dissolved microspheres were excised and the emitting fluorescence was read using a luminescence spectrophotometer (LS-50B, Perkin-Elmer, Beaconsfield, Buckinghamshire, UK). Blank measurements were performed to determine background fluorescence.

***Table 2.1:*** *Excitation and emission wavelength used for fluorescence measurements.*

| Color | Excitation Wavelength [nm] | Emission Wavelength [nm] |
|---|---|---|
| Blue | 365 | 415 |
| Blue-green | 430 | 450 |
| Yellow-green | 480 | 495 |
| Orange | 530 | 545 |
| Red | 580 | 592 |
| Crimson | 610 | 620 |
| Scarlet | 645 | 660 |

In this substudy, only fluorescence-labeled microspheres derived perfusion measurements at the end of the BIPAP/APRV 0% and BIPAP/APRV >60% sequences were analyzed.

## 2.2.2 Data Processing and Analysis

### 2.2.2.1 Analysis of Respiratory Mechanics Variables

The respiratory volume signal was calculated from the 5 min recordings of the airflow by numerical integration for each measurement time point. The time points of the beginning of inspiration and expiration were detected from the airflow signal using a zero crossing algorithm. For each respiratory cycle, $V_T$ was computed as difference between the minimum and maximum value of the respiratory volume signal. MV was computed as RR multiplied by $V_T$.

For each measurement time point, $P_{aw,mean}$, PEEP, and $P_{aw,peak}$ were calculated from the 5 min recordings of the Paw-signal as average, minimum, and maximum value of the $P_{aw}$ signal of each respiratory cycle, respectively, and averaged over all respiratory cycles during the 5 min recordings. The transpulmonary pressure ($P_L$) was calculated as difference in $P_{aw}$ and esophageal pressure. Mean transpulmonary pressures ($P_{L,mean}$) and peak transpulmonary pressures ($P_{L,peak}$) were calculated from the 5 min recordings of the $P_L$-signal as average and maximum values of each respiratory cycle, respectively, and averaged over all respiratory cycles during the 5 min recordings.

The product of esophageal pressure and time (pressure time product: PTP) was calculated during inspiration, using the first value at the beginning of the respiratory cycle as offset. For each measurement time point, PTP was averaged over all respiratory cycles during the 5 min recordings.

#### 2.2.2.2 Definition of Lung Fields for Analysis of Imaging Data

The CT scans at end-expiratory lung volume were coregistrated to the corresponding static PET scans using the software Rover (ABX advanced and biochemical compounds GmbH, 2015), (Hofheinz et al., 2012). The downscaled CT scans were used for manual segmentation of volumetric masks of the left and right lungs, respectively, using the software ITK-Snap, Version 2.4.0. 2012 (Yushkevich et al., 2006). The trachea, main bronchi, and associated blood vessels were excluded from the lung masks. Regions outside the lung masks were excluded from further analyzis.

#### 2.2.2.3 Analysis of CT Scans for Quantification of Lung Aeration

Using the downscaled CT scans, lung tissue mass was calculated for each voxel within the lung masks using the software Matlab (MathWorks, Natick, MA, Version R2012b) and taking advantage of the linear correlation of the CT number and the density of the voxel (g/cm$^3$), (Richter et al., 2015). Voxel with mass < 5 % of the maximal mass of the dataset were excluded. Values were defined as outliers using the definition of (Leys et al., 2013). Outliers were excluded from further analyzis.

#### 2.2.2.4 Analysis of $^{68}$Ga-Labeled Microspheres Derived Perfusion Measurements

For each of the 7 selected animals and for the left and right lungs separately (n = 14 lungs), the activity emitted by $^{68}$Ga-labeled microspheres injected for $^{68}$Ga-PET scans at previous time points ($^{68}$Ga-PET$_{before}$) was subtracted from the measured radioactivity emitted by $^{68}$Ga-labeled microspheres injected at the actual time point ($^{68}$Ga-PET$_{after}$), taking into account the decay half-lives of $^{68}$Ga. For each voxel, relative lung perfusion was calculated as **mass-normalized, relative radioactive intensity** ($Q_{RM}$) according to Equation (2.5).

$$Q_{RM,i} = \frac{\frac{(^{68}Ga-PET_{after,i} - ^{68}Ga-PET_{before,i}) * V_{Voxel}}{m_i}}{\sum_{i=1}^{n} \frac{(^{68}Ga-PET_{after,i} - ^{68}Ga-PET_{before,i}) * V_{Voxel}}{m_i}}{n} \quad (2.5)$$

In this equation, i represents the voxel number, n is the total number of voxel within the lung mask, m is the lung tissue mass of the voxel, and $V_{Voxel}$ represents the volume of a voxel. Values were defined as outliers, if flow was outside the range of median ± 3 * median absolute deviation within the transversal, coronal, and sagittal planes (Leys et al., 2013). Outliers were excluded from further analyzis.

For the left and right lung of each animal, global heterogeneity of $Q_{RM}$-measurements was estimated as variance of perfusion values of all voxel within the lung normalized by the square of the mean, also defined as coefficient of variation squared ($CV^2$) and in the following referred to as heterogeneity on a whole lung level (Venegas and Galletti, 2000; Winkler et al., 2015).

Also for each lung separately, regional heterogeneity of $Q_{RM}$-measurements was quantified as $CV^2$ of voxel within 24.36 x 24.36 x 25 $mm^3$ elements (which corresponds to 6 x 6 x 5 voxel). For comparison among all animals and lungs, mean micro level $CV^2$-values were calculated for each lung.

For each voxel, $Q_{RM}$ was characterized as function of location along the ventro-dorsal and cranio-caudal axes by means of linear least-squares regression analyzis. Vertical perfusion gradients were characterized by the slope of the regression lines. The dimension of the vertical perfusion gradients were relative flow units per cm. Positive slopes indicate an increase in perfusion from the ventral or cranial to the dorsal or caudal region, respectively.

The outer dimensions of the 7 left and right lungs were assessed. For one representative animal, a three-dimensional visualization of the outer contours of the left and right lungs were obtained from $Q_{RM}$-measurements using the software Matlab (MathWorks, Natick, Massachusetts).

#### 2.2.2.5 Downscaling of $^{68}$Ga-Labeled Microspheres Derived Perfusion Measurements

For each of the 7 selected animals and for each lung separately, both the $^{68}$Ga-PET datasets and the CT datasets were downscaled to the resolution of the fluorescence-labeled microspheres derived perfusion measurements using the function *imresize* implemented in the software Matlab (MathWorks, Natick, MA, Version R2012b). Downscaled datasets featured 33 x 57 x 57 voxel with a voxel size of 12 x 12 x 12 $mm^3$. Using the downscaled CT and PET datasets, **downscaled mass-normalized, relative radioactive intensity** ($Q_{RM,downscale}$) was calculated for each voxel within the lung according to Equation (2.5). Values were defined as outliers, if flow was outside the range of median ± 3 * median absolute deviation within the transversal, coronal, and sagittal planes (Leys et al., 2013). Outliers were excluded from further analyzis.

The distribution of $Q_{RM,downscale}$-measurements was characterized as function of location along the ventro-dorsal and cranio-caudal axes by means of linear least-squares regression analyzis. Vertical perfusion gradients were characterized by the slope of the linear regression lines.

For each lung, heterogeneity on a whole lung level of $Q_{RM,downscale}$-measurements was estimated as $CV^2$. Regional heterogeneity was quantified as $CV^2$ of voxel within 24.0 x 24.0 x 24.0 $mm^3$ elements (corresponding to 2 x 2 x 2 voxel). For comparison among all animals and lungs, mean micro level $CV^2$-values were calculated for each lung.

### 2.2.2.6 Analysis of Fluorescence-Labeled Microspheres Derived Perfusion Measurements

#### 2.2.2.6.1 Definition of Lung Fields for Analysis of Fluorescence Data

For the analyzis of the mass of lung pieces and the fluorescence-labeled microspheres derived perfusion measurements, the left and right lungs of the 7 selected animals were analyzed separately (n = 14 lungs). Lung pieces featuring larger airways or vessels (airway score > 1) were excluded from further analyzis. Only a subset of lung pieces was analyzed for its mass and for mass- as well as mass- and volume-normalized, relative fluorescence intensities (see chapter 2.2.2.6.3). Only pieces that fully consisted of lung tissue but no lung-embedding foam were analyzed. It was therefore assumed that this subset of pieces featured comparable lung tissue volume.

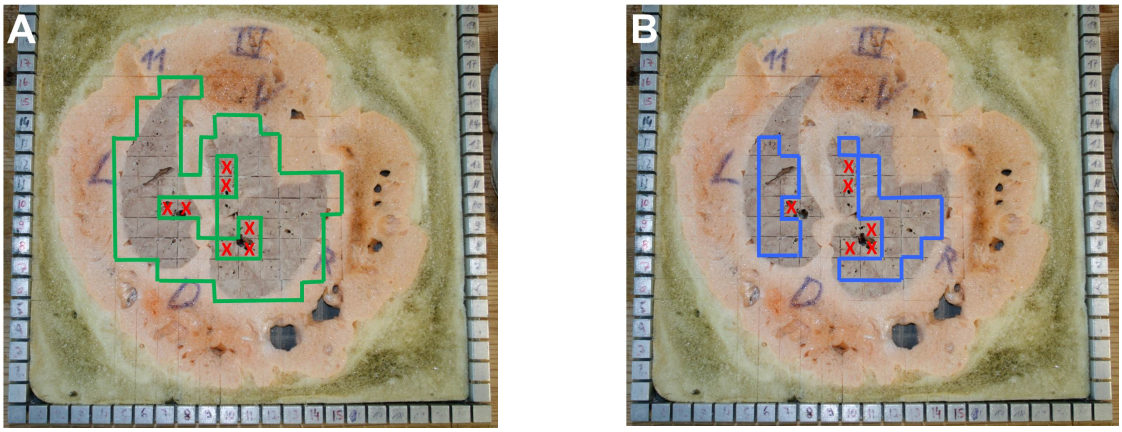


***Figure 2.7:*** *Rigid grid system used for post mortem processing of air dried lung slices embedded in foam. In parts of the analyzis, all pieces containing lung tissue were selected (left picture A: all pieces containing lung tissue are highlighted by green boarder line), whereas in other parts of the analyzis only pieces fully containing of lung tissue and no lung-embedding foam were analyzed (right picture B: subset of analyzed lung pieces is highlighted by blue boarder line). Pieces featuring larger airways or vessels were excluded from the analyzis (as highlighted by red cross in both pictures).*

#### 2.2.2.6.2 Analysis of Mass of Lung pieces

For each of the 14 analyzed lungs separately, lung pieces fully containing of lung tissue were defined as outliers, if its mass was outside the range of median ± 3 * median absolute deviation within the transversal, coronal, and sagittal planes (Leys et al., 2013). Outliers were excluded from further analyzis. The distribution of mass was characterized as function of location along the ventro-dorsal and cranio-caudal axes by means of linear least-squares regression analyzis. Vertical mass gradients were characterized by the slopes of the linear regression lines.

#### 2.2.2.6.3 Analysis of Fluorescence Measurements

For every piece of each of the 14 analyzed lungs, the net fluorescence intensity ($I_{FM,net}$) was calculated by subtraction of the average color-specific background fluorescence intensity from the measured color-specific fluorescence intensity.

Considering the mass (m) of each lung piece, lung perfusion was calculated for every lung piece including boundary pieces consisting of lung tissue and lung-embedding foam as **mass-normalized, relative fluorescence intensity** ($Q_{FM,Mass}$) as shown in Equation (2.6).

$$Q_{FM,Mass,i} = \frac{\frac{I_{FM,net,i}}{m_i}}{\frac{1}{n} * \sum_{i=1}^{n} \frac{I_{FM,net,i}}{m_i}} \tag{2.6}$$

In this equation, i represents the voxel number, n is the total number of pieces the lungs were cut into. Mean mass-normalized, relative fluorescence intensity of each lung was therefore 1 and accounted for differing total number of injected fluorescent microspheres.

For all pieces featuring comparable lung tissue volume, lung perfusion was calculated as **volume-normalized, relative fluorescence intensity** ($Q_{FM,Volume}$) according to Equation (2.7).

$$Q_{FM,Volume,i} = \frac{\frac{I_{FM,net,i}}{V_{Tissue}}}{\frac{1}{z} * \sum_{i=1}^{z} \frac{I_{FM,net,i}}{V_{Tissue}}} \tag{2.7}$$

In this equation, i represents the voxel number and z is the total number of pieces fully consisting of lung tissue and no lung-embedding foam.

Since the volume of the subset of analyzed lung pieces is approximately comparable, Equation (2.7) can be simplified to Equation (2.8).

$$Q_{FM,Volume,i} = \frac{I_{FM,net,i}}{\frac{1}{z} * \sum_{i=1}^{z} FM,net,i} \quad (2.8)$$

Similarly, **mass- and volume-normalized, relative fluorescence intensity** ($Q_{FM,Mass,Volume}$) was calculated for all pieces featuring comparable lung tissue volume according to Equation (2.9).

$$Q_{FM,Mass,Volume,i} = \frac{\frac{I_{FM,net,i}}{m_i}}{\frac{1}{z} * \sum_{i=1}^{z} \frac{I_{FM,net,i}}{m_i}} \quad (2.9)$$

For $Q_{FM,Mass}$, $Q_{FM,Volume}$, and $Q_{FM,Mass,Volume}$, respectively, values were defined as outliers, if perfusion was outside the range of median ± 3 * median absolute deviation within the transversal, coronal, and sagittal planes (Leys et al., 2013). Outliers were excluded from further analyzis.

Assuming linear correlation, the distributions of $Q_{FM,Mass}$, $Q_{FM,Volume}$, and $Q_{FM,Mass,Volume}$-measurements were characterized as function of location along the ventro-dorsal and cranio-caudal axes by means of linear least-squares regression analyzis. Vertical perfusion gradients were characterized by the slope of the linear regression lines. The dimension of the vertical perfusion gradients were relative flow units per cm. A slope of + 0.04 / cm, for example, describes an increase in flow by 0.04 of mean normalized flow per unit cm along the axis.

For $Q_{FM,Mass}$-, $Q_{FM,Volume}$-, and $Q_{FM,Mass,Volume}$-measurements, respectively, heterogeneity on a whole lung level was estimated as $CV^2$. Regional heterogeneity was quantified as $CV^2$ of voxel within 24.0 x 24.0 x 24.0 $mm^3$ elements (corresponding to 2 x 2 x 2 voxel). For comparison among all animals and lungs, mean micro level $CV^2$-values were calculated for each lung.

The outer dimensions of the 7 left and right lungs were assessed. For one representative animal, a three-dimensional visualization of the outer contours of the left and right lungs were obtained from $Q_{FM,Mass}$-measurements using the software Matlab (MathWorks, Natick, Massachusetts).

### 2.2.3 Statistics

Data are presented as median and [25 % and 75 % quantile] if not stated otherwise. Due to the small sample size, statistical analyzes were done using non-parametric tests. Global statistical significance levels were defined as p-values ≤ 0.05. Tests were performed using the software SPSS (Version 23, IBM SPSS statistics, Armonk, USA).

The slopes of the linear regressions of perfusion and spatial location were compared with zero using a one-sample two-tailed t-test. The detected slopes of the linear regression of perfusion and spatial location along both axes were compared between $^{68}$Ga-labeled and fluorescence-labeled microspheres derived measurements using Wilcoxon signed rank tests for matched pairs. Adjustments for repeated measurements were done according to the Bonferroni-Holm procedure.

Measurements of the distribution of pulmonary blood flow were compared between *in vivo* $Q_{RM}$- and $Q_{RM,downscale}$-measurements and *ex vivo* $Q_{FM,Volume}$-, $Q_{FM,Mass}$-, and $Q_{FM,Volume,Mass}$-measurements using Bland-Altman diagrams.

# 3 Results

This section is comprised of two sub-sections. The results of the study on the inflammatory impact of volutrauma and atelectrauma are presented in the first sub-section, whereas the results of the study on fluorescence-labeled microspheres derived perfusion measurements in ARDS are depicted in the second sub-section.

## 3.1 Volutrauma and Atelectrauma in ARDS

### 3.1.1 General Aspects

Body weight, number of saline lung lavages and cumulative doses of crystalloids and colloids did not differ between volutrauma and atelectrauma (Appendix: Table A.5.1).

### 3.1.2 Respiratory Mechanics, Pulmonary Gas Exchange and Hemodynamics

**Respiratory mechanics**

$V_T$ and RR were comparable between volutrauma and atelectrauma and constant over time in both groups (Appendix: Table A.5.2). $P_{aw,mean}$, $P_{aw,peak}$, and the percentage of volume-dependent components of $E_{rs}$ were higher in volutrauma, whereas $R_{rs}$, $E_{rs}$, and $\Delta P$ were increased in atelectrauma, as indicated by a significant difference of the respective group effect (Appendix: Table A.5.2). $\Delta P$ was initially (Baseline, Injury) comparable between groups, but increased in atelectrauma, but not in volutrauma, over time and was significantly different at time point T 4 (Appendix: Table A.5.2). At time point T 4, mechanical power was higher in volutrauma as compared to atelectrauma (volutrauma: 16.44 [13.07 - 16.93] J/min; atelectrauma: 5.64 [5.62 - 6.52] J/min; $p = 0.016$), while regional “intensity” was comparable between groups (volutrauma: 0.071 [0.043 - 0.076] J/min/g; atelectrauma: 0.062 [0.049 - 0.081] J/min/g; $p = 0.917$).

**Gas exchange and Hemodynamics**

Lung lavage induced a decrease in $PaO_2$ and an increase in $PaCO_2$, respectively, but both parameters did not differ between groups at Baseline or Injury time point (Appendix: Table A.5.3). Parameters regarding hemodynamics and gas exchange were comparable between groups. There was a no significant trend towards a higher $PaCO_2$ in volutrauma as compared to atelectrauma (Appendix: Table A.5.3).

### 3.1.3 Imaging Results: Overview

Figure 3.1 illustrates the distribution of aeration, $F_{Gas}$, perfusion, and $K_{iS}$ in one representative animal of each group.

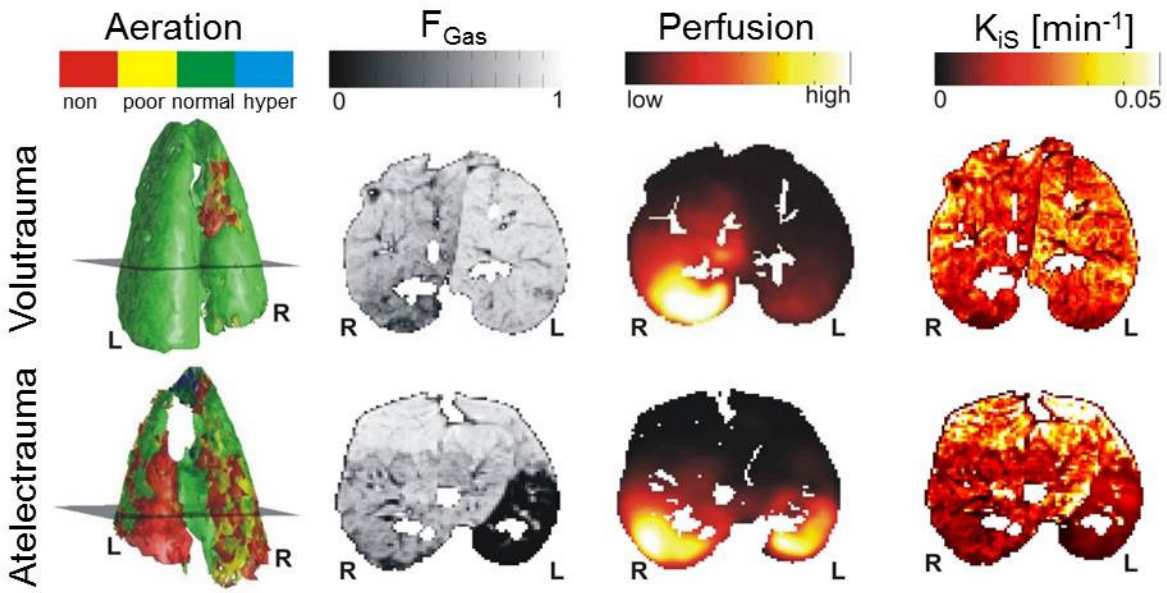


***Figure 3.1:*** *Three-dimensional illustration of the distribution of aeration (1. column), as well as transversal slices of the distribution of $F_{Gas}$ (2. column), perfusion (3. column), and $K_{iS}$ (4. column) in one representative animal of the volutrauma (upper panel) and atelectrauma group (lower panel), respectively. Positions of the transversal slices are illustrated in the 3D image and were chosen as the slices featuring maximal cross-sectional areas. Color bars denote the respective scales. Hyper corresponds to hyper-aerated compartment; normal to normally aerated compartment; poor to poorly aerated compartment, and non to non-aerated compartment. L corresponds to the ventilated, VILI lung and R to the non-ventilated, control lung.*

### 3.1.4 Analysis of CT Data

**Lung Volume**

The volumes of the ventilated, VILI and non-ventilated, control lungs were 1406.0 [1283.9 – 1824.3] L and 1172.8 [855.4 – 1418.9] L in volutrauma, and 415.7 [362.1 – 566.5] L and 1176.8 [937.1 – 1270.4] L in atelectrauma, respectively. The volumes of the ventilated, VILI lungs were significantly higher than that of the non-ventilated, control lungs in the atelectrauma ($p = 0.043$), but not in the volutrauma group ($p = 0.080$). The volumes of the ventilated, VILI lungs of the volutrauma group were highly significantly higher than that of the atelectrauma group ($p \leq 0.01$), whereas the sizes of the non-ventilated, control lungs were comparable between groups ($p = 0.917$).

**Lung Weight**

The weights of the ventilated, VILI and non-ventilated, control lungs were 293.9 [208.2 – 313.1] g and 410.1 [350.6 – 487.6] g in volutrauma, and 326.2 [268.6 – 521.2] g and 423.3 [343.6 – 586.3] g in atelectrauma, respectively. Weights of the ventilated, VILI lungs as well as weights of the non-ventilated, control lungs did not differ between groups (VILI lungs: p = 0.251; control lungs: p = 0.754). In volutrauma, the weights of the ventilated, VILI lungs were higher than that of the corresponding non-ventilated, control lungs (p = 0.043), whereas in atelectrauma weights were comparable between corresponding lungs (p = 0.080). Tissue masses of the isogravimetric subregions of the 15 cm cranio-caudal lung field assessed by dynamic PET scanning were only comparable between ROIs of the same ventilated, VILI lung, but not between animals or groups (Table 3.1). Mass of the total 15 cm cranio-caudal field of the ventilated, VILI lungs were lower in volutrauma as compared to atelectrauma, both absolutely and relatively to the mass of the whole ventilated, VILI lungs (Table 3.1). Analyzing the whole cranio-caudal lung expansion, tissue mass of the ventilated, VILI lungs were higher in volutrauma (268.2 [216.5 – 281.4] g) as compared to atelectrauma (107.2 [90.6 - 134.4] g; p = 0.009).

***Table 3.1:*** *Tissue mass per isogravimetric subregion of the 15 cm cranio-caudal field of the ventilated, VILI lungs and non-ventilated, control lungs at end of expiration of all animals of the volutrauma and atelectrauma group, respectively.*

| | **Volutrauma: Ventilated, VILI Lung** | **Atelectrauma: Ventilated, VILI Lung** |
|---|---|---|
| Mass of ROI1 [g] | 30.85 # [29.47 – 35.04] | 52.67 [37.67 – 55.05] |
| Mass of ROI2 [g] | 31.15 # [29.45 – 35.08] | 50.01 [35.68 – 53.88] |
| Mass of ROI3 [g] | 31.53 # [30.02 – 35.57] | 49.57 [35.88 – 54.56] |
| Mass of ROI4 [g] | 31.50 # [29.53 – 35.16] | 50.78 [36.99 – 54.70] |
| Mass of ROI5 [g] | 30.57 # [29.76 – 35.27] | 50.29 [36.78 – 54.71] |
| Mass of all ROIs [g] | 155.60 # [148.23 – 176.13] | 253.32 [182.46 – 272.89] |
| Mass of all ROIs [% of whole lung mass] | 56.63 ## [50.05 – 59.93] | 71.90 [63.22 – 72.90] |

*# p ≤ 0.05 (vs. same ROI of the ventilated, VILI lungs of the atelectrauma group). ## p ≤ 0.01 (vs. same ROI of the ventilated, VILI lungs of the atelectrauma group). No significant differences between ROIs of the same lung in both groups.*

**Average Lung Aeration**

The normally and hyper-aerated compartments were much bigger while the non-aerated compartment was much smaller in the ventilated, VILI lungs of the volutrauma compared to the atelectrauma group (Figure 3.2). Sizes of the aeration compartments of the non-ventilated, control lungs were comparable between groups (Figure 3.2). In volutrauma, normally and hyper-aerated compartments were smaller, while poorly and non-aerated compartments were bigger in the non-ventilated, control lungs as compared to the ventilated, VILI lungs (Figure 3.2). In comparison, in atelectrauma, normally and hyper-aerated compartments were bigger, while non-aerated compartment was smaller in the non-ventilated, control lungs as compared to the ventilated, VILI lungs (Figure 3.2).

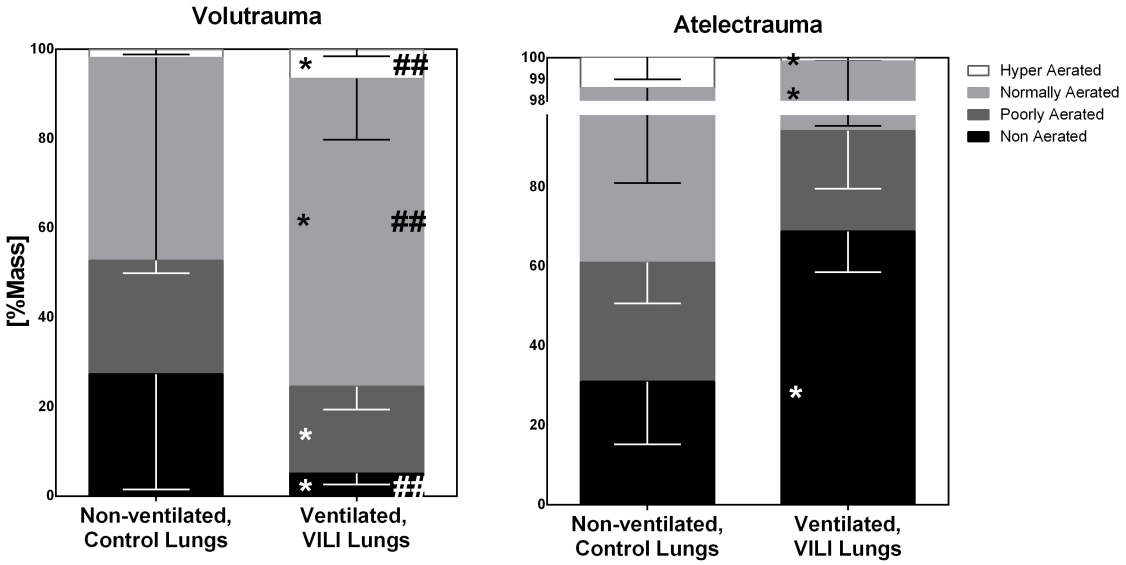


***Figure 3.2:*** *Mean and standard deviation (error bar) of the percentage of hyper-aerated (white), normally aerated (light gray), poorly aerated (dark gray), and non-aerated compartments (black) relative to the total mass [% mass] of the ventilated, VILI lungs and non-ventilated, control lungs of the volutrauma (left panel) and atelectrauma group (right panel), respectively. Note different axes scales between panels. * p ≤ 0.05 (ventilated, VILI lungs vs. non-ventilated, control lungs for same aeration compartment and group). # p ≤ 0.05 (volutrauma vs. atelectrauma for same aeration compartment of the ventilated, VILI lungs). ## p ≤ 0.01 (volutrauma vs. atelectrauma for same aeration compartment of the ventilated, VILI lungs).*

**Regional Lung Aeration**

Within all subregions and at end-expiration and end-inspiration, respectively, the normally and hyper-aerated compartments were significantly bigger, while the non-aerated compartments were significantly smaller in the ventilated, VILI lungs of the volutrauma compared to the atelectrauma group (Figure 3.3). At end-inspiration, the poorly aerated compartment was smaller in ventral and second most ventral lung regions in the ventilated, VILI lungs of the volutrauma compared to the atelectrauma group, while only ventral regions featured smaller poorly aerated compartments at end-expiration (Figure 3.3).

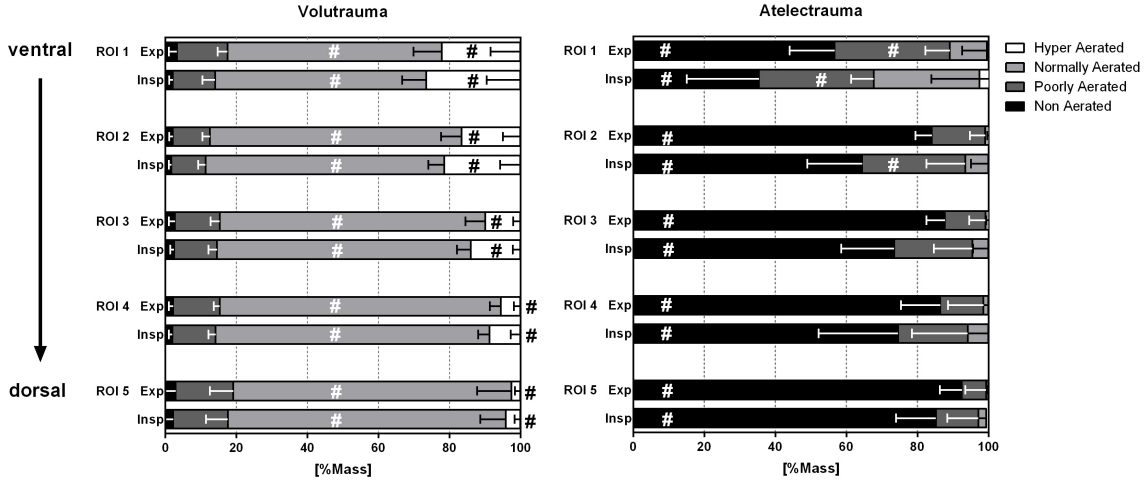


***Figure 3.3:*** *Mean and standard deviation of the percentage of hyper-aerated (white), normally aerated (light gray), poorly aerated (dark gray) and non-aerated compartments (black) relative to the total mass [% mass] of ventilated, VILI lungs in volutrauma (left panel) and atelectrauma (right panel), respectively, for 5 adjacent regions of the same lung mass reaching from ventral (ROI 1) to dorsal (ROI 5) at end-expiration (Exp) and end-inspiration (Insp), respectively. # $p \leq 0.05$ (atelectrauma vs. volutrauma for same aeration compartment in same ROI at the same lung volume). No significant difference of size of aeration compartments between ROIs of the same lung and group.*

### Tidal Changes of Lung Aeration

The extent of tidal hyper-aeration was higher in volutrauma as compared to atelectrauma in all, except to ventral, ROIs (Figure 3.4). In contrast, tidal recruitment was significantly higher in the atelectrauma compared to the volutrauma group in all lung regions. In volutrauma, tidal hyper-aeration was increased compared to tidal recruitment in all, except the dorsal, lung regions. In ventral, mid-ventral and middle lung regions of the atelectrauma group, tidal recruitment was significantly higher than tidal hyper-aeration (Figure 3.4).

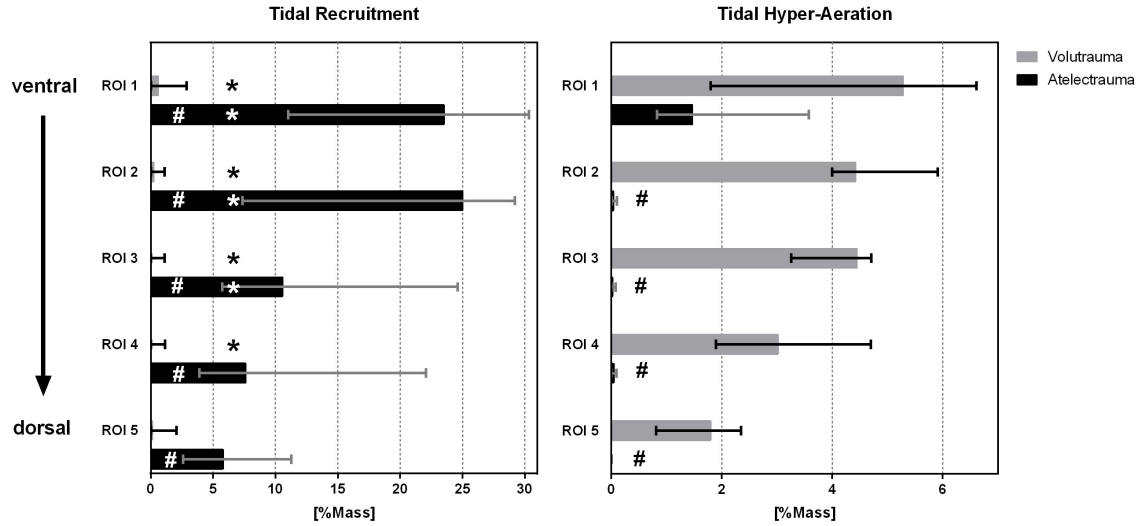


***Figure 3.4:*** *Extent of tidal recruitment (left panel) and tidal hyper-aeration (right panel) of ventilated, VILI lungs in volutrauma (gray) and atelectrauma (black), respectively, in 5 adjacent regions of the same lung mass reaching from ventral (ROI 1) to dorsal (ROI 5). Note different axes scales in left and right panel. * $p \leq 0.05$ (tidal recruitment vs. tidal hyper-aeration in same ROI and group). # $p \leq 0.05$ (atelectrauma vs. volutrauma for tidal recruitment or tidal hyper-aeration, respectively, in same ROI).*

### 3.1.5 Lung Perfusion

Absolute perfusion of the ventilated, VILI lungs did not differ between volutrauma and atelectrauma, both on a whole lung level (volutrauma: 1.510 [1.098 – 2.202] L/min; atelectrauma: 1.410 [1.298 – 2.192] L/min; p = 0.917) as well as on a regional level (Figure 3.5). Absolute perfusion of the non-ventilated, control lungs did also not differ between groups (volutrauma: 3.629 [2.797 – 4.454] L/min; atelectrauma: 3.969 [3.364 – 6.436] L/min; p = 0.347). Absolute perfusion of the ventilated, VILI lungs compared to the non-ventilated, control lungs was lower in atelectrauma ($p \leq 0.05$), but not in volutrauma (p = 0.080). However, on a regional level, absolute perfusion of the ventilated, VILI compared to the non-ventilated, control lungs of the volutrauma group was lower in all, except the dorsal, ROIs. In atelectrauma, all ROIs showed lower absolute perfusion of the ventilated, VILI compared to the non-ventilated, control lungs (Figure 3.5). Both in volutrauma and atelectrauma, absolute perfusion was comparable between subregions of the ventilated, VILI lungs and the non-ventilated, control lungs, respectively (Figure 3.5).

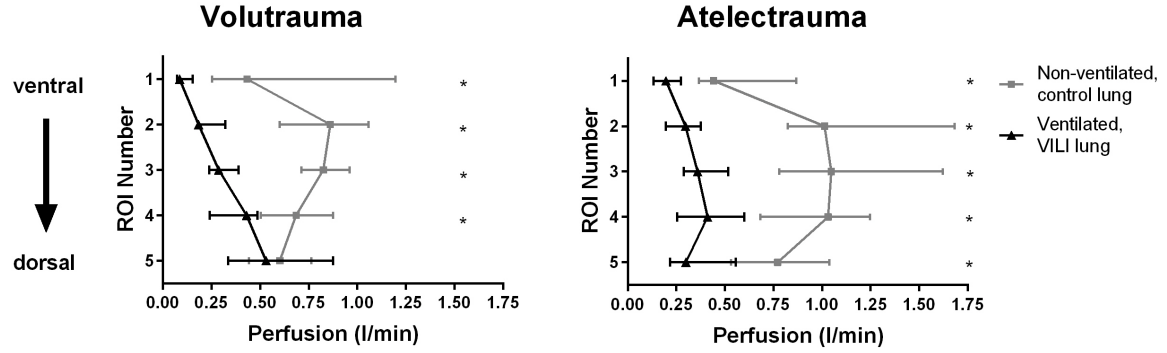


***Figure 3.5:*** *Absolute regional lung perfusion in 5 adjacent regions of the same lung mass reaching from ventral (ROI 1) to dorsal (ROI 5) for the ventilated, VILI (black triangles) and non-ventilated, control lungs (gray squares) of all animals of the volutrauma (left panel) and atelectrauma group (right panel), respectively. * $p \leq 0.05$ (ventilated, VILI lungs vs. non-ventilated, control lungs in same ROI and group). No significant difference between ventilated, VILI lungs of the volutrauma and atelectrauma group in same ROI. No significant difference between ROIs of the same lung and group.*

### 3.1.6 Pulmonary Neutrophilic Inflammation

**Whole Lung Level**

$K_i$ and $F_{Blood}$ were lower, while $F_{Gas}$ and $K_{iS}$ were higher in the ventilated, VILI lungs of the volutrauma compared to the atelectrauma group, respectively (Table 3.2). In contrast, $K_i$, $F_{Blood}$, $F_{Gas}$, and $K_{iS}$ of the non-ventilated, control lungs did not differ between groups. In volutrauma, $F_{Blood}$ was lower while $F_{Gas}$ was higher in the ventilated, VILI compared to the non-ventilated, control lungs. The opposite distribution occurred in atelectrauma. In atelectrauma, $K_i$ of the ventilated, VILI lungs was higher compared to the non-ventilated, control lungs. In volutrauma but not in atelectrauma, $K_{iS}$ of the ventilated, VILI lungs was higher compared to the respective non-ventilated, control lungs (Table 3.2).

***Table 3.2:*** *$K_i$, $F_{Gas}$, $F_{Blood}$, and $K_{iS}$ of the ventilated, VILI lungs and non-ventilated, control lungs of all animals of the volutrauma and atelectrauma group, respectively.*

| | **Volutrauma** | | **Atelectrauma** | |
|---|---|---|---|---|
| | **Ventilated, VILI Lung** | **Non-ventilated, Control Lung** | **Ventilated, VILI Lung** | **Non-ventilated, Control Lung** |
| $K_i$ [$10^{-3}$/min] | 3.05 ## | 3.85 | 7.77 * | 2.78 |
| | [2.61 – 3.95] | [2.54 – 4.68] | [6.64 – 8.33] | [2.53 – 3.11] |
| $F_{Gas}$ | 0.78 * ## | 0.68 | 0.22 * | 0.65 |
| | [0.77 – 0.79] | [0.63 – 0.69] | [0.18 – 0.24] | [0.60 – 0.65] |
| $F_{Blood}$ | 0.04 * ## | 0.08 | 0.17 * | 0.09 |
| | [0.03 – 0.04] | [0.08 – 0.09] | [0.17 – 0.19] | [0.07 – 0.10] |
| $K_{iS}$ [$10^{-3}$/min] | 16.89 * ## | 10.58 | 13.49 | 11.51 |
| | [14.58 – 22.66] | [9.72 – 16.11] | [9.85 – 13.71] | [9.44 – 13.30] |

** $p \leq 0.05$ (vs. non-ventilated, control lung of the same group). ## $p \leq 0.01$ (vs. ventilated, VILI lung of atelectrauma group).*

### Regional Inflammation

$K_i$ and $F_{Blood}$ were lower while $F_{Gas}$ was higher in all regions of the ventilated, VILI lungs of the volutrauma compared to the atelectrauma group (Figure 3.6). In volutrauma, $F_{Gas}$ of ventilated, VILI lungs was higher compared to the respective non-ventilated, control lungs in all ROIs. The opposite distribution occurred in all ROIs of the atelectrauma group. In volutrauma, $F_{Blood}$ of the ventilated, VILI lungs was lower compared to the respective non-ventilated, control lungs in all ROIs. The opposite distribution occurred in mid-ventral, central and mid-dorsal ROIs of the atelectrauma group. While in atelectrauma $K_i$ was higher in all regions of the ventilated, VILI lungs compared to the corresponding non-ventilated, control lungs, there was no difference in any ROI of the volutrauma group. In mid-ventral, central, and mid-dorsal lung regions, $K_{iS}$ of the ventilated, VILI lungs of the volutrauma group were higher compared to the corresponding non-ventilated, control lungs and to ventilated, VILI lungs of the atelectrauma group, respectively (Figure 3.6).

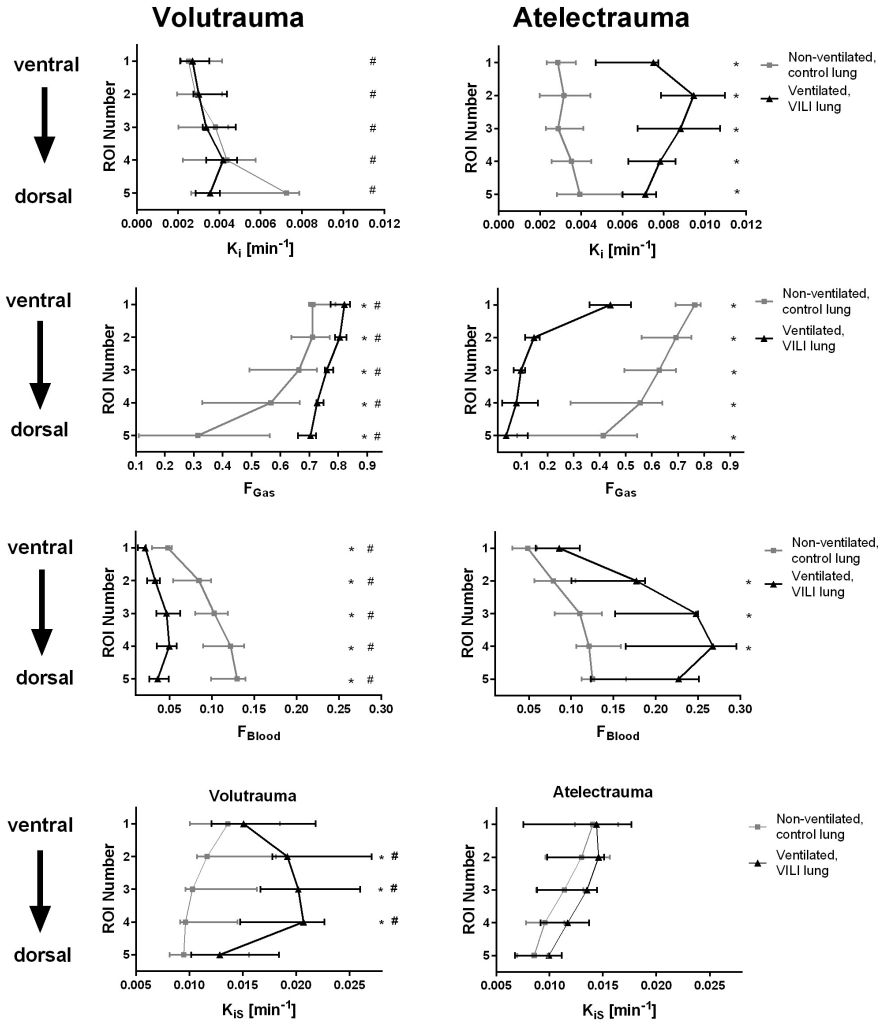


***Figure 3.6:*** *$K_i$, $F_{Gas}$, $F_{Blood}$, and $K_{iS}$ (line 1 to line 4) in 5 adjacent regions of the same lung mass reaching from ventral (ROI 1) to dorsal (ROI 5) for the ventilated, VILI lungs (black triangles) and non-ventilated, control lungs (gray squares) of all animals of the volutrauma (left panel) and atelectrauma group (right panel), respectively. * p ≤ 0.05 (vs. same ROI of non-ventilated, control lungs, same group). # p ≤ 0.05 (vs. same ROI of the ventilated, VILI lungs of atelectrauma group). ## p ≤ 0.01 (vs. same ROI of the ventilated, VILI lungs of atelectrauma group).*

### 3.1.7 Results of *ex vivo* Analyses

**Wet- To- Dry Ratio**

The wet- to- dry ratios of samples of the upper lobe of the ventilated, VILI and non-ventilated, control lungs were 5.9 [5.4 – 7.4] g and 6.1 [6.0 – 8.3] g in volutrauma, and 8.4 [8.2 – 10.1] g and 7.6 [7.4 – 8.3] g in atelectrauma, respectively. Wet- to- dry ratios did not differ between volutrauma and atelectrauma both for the ventilated, VILI lungs ($p = 0.142$) and the non-ventilated, control lungs ($p = 0.293$). In both groups, wet- to- dry ratios did not differ between ventilated, VILI and non-ventilated, control lungs (volutrauma: $p = 0.176$; atelectrauma: $p = 0.225$).

**Molecular Biology**

Both in volutrauma and atelectrauma, the protein concentrations of IL-6 and IL-8 did not differ between the ventilated, VILI and the non-ventilated, control lungs (Figure 3.7). Both in the ventilated, VILI and in the non-ventilated, control lungs, protein concentrations of IL-6 and IL-8 did also not differ between volutrauma and atelectrauma. The protein concentration of TNF-α was not detectable in 24 of the 30 samples of the volutrauma group and in 18 of the 30 samples of the atelectrauma group.

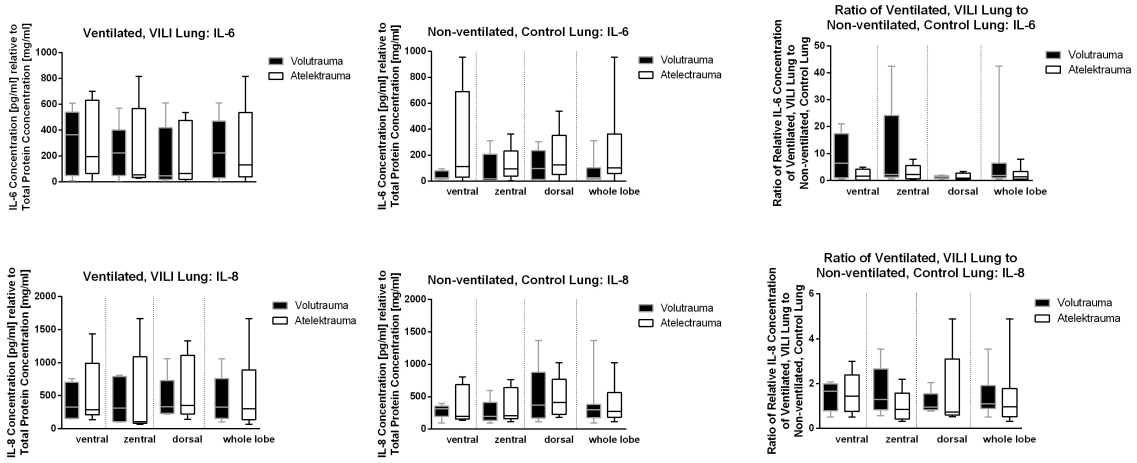


***Figure 3.7:*** *Protein concentrations of IL-6 (upper line) and IL-8 (lower line), in the ventilated, VILI lungs (1. column) and in the non-ventilated, control lungs (2. column) as well as the ratio of the concentration in the ventilated, VILI to the non-ventilated, control lungs (3. column) of ventral, central and dorsal regions of the upper lobes of all animals of the volutrauma (left, black panel) and atelectrauma group (right, white panel). No significant difference of protein concentrations of IL-6 and IL-8, respectively, between same ROI of corresponding lungs of the volutrauma and atelectrauma group, respectively. No significant difference of protein concentrations of IL-6 and IL-8, respectively, between ventilated, VILI lungs and corresponding non-ventilated, control lungs in both groups and all ROIs.*

## 3.2 Fluorescence-Labeled Microspheres Derived Perfusion Measurements in ARDS

### 3.2.1 General Aspects

Three to 13 lung lavages were necessary to induce moderate ARDS. At the end of the experiment, excised lungs of 5 of the 12 animals had to be excluded from the analyzis of fluorescence-labeled microspheres derived perfusion measurements due to rotation artifacts resulting from strong rotation of the lungs around their sagittal axis during fixation with the two-component foam (see Figure 3.8 for illustration). Therefore, only the left and right lungs of 7 animals were further analyzed.

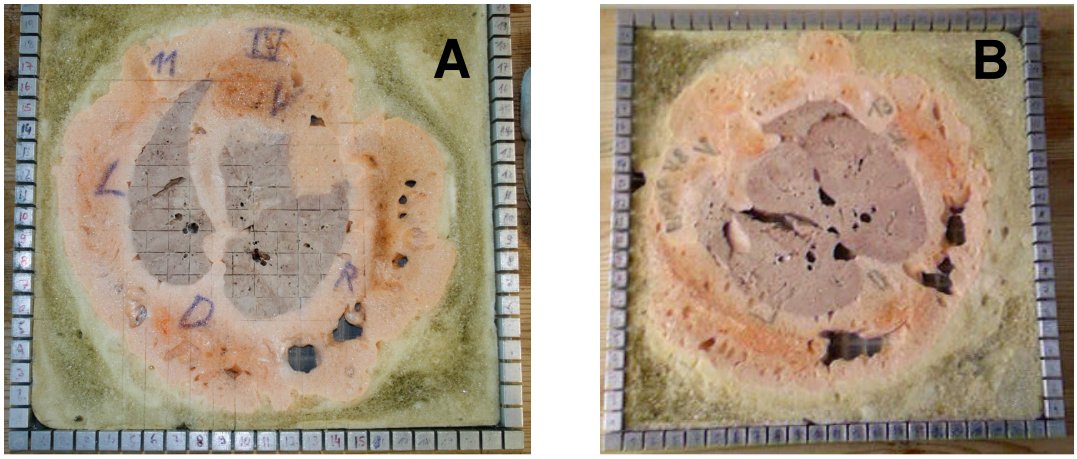


***Figure 3.8:*** *The lungs of 2 different animals (inner, brown structure) embedded in one-component polyurethane foam (orange structure) and two-component polyurethane foam (outermost, yellow structure). Lung-foam-blocks were cut into slices and placed in a rigid grid system for further processing. The lung shown in the left subplot (A) was selected for further analyzis, whereas the lung shown in the right subplot (B) was excluded from further analyzis since it was strongly rotated around its sagittal axis.*

The right lung of one animal had to be excluded due to incomplete PET/CT data and missing caudal lung parts for measurements in BIPAP/APRV 0%. The remaining left and right lungs were analyzed separately, resulting in n = 13 lungs analyzed for the *in vivo* $Q_{RM}$-measurements and *ex vivo* $Q_{FM}$-measurements in BIPAP/APRV 0% and BIPAP/APRV >60%, respectively.

### 3.2.2 Resolution of *ex vivo* and *in vivo* Perfusion Measurements

The resolution of the $Q_{RM}$-measurements (4.06 x 4.06 x 5 $mm^3$) was about 21 times higher than that of the $Q_{FM}$-measurements (12 x 12 x 12 $mm^3$). Consequently, lungs were represented by a correspondingly higher number of voxel or lung pieces in $Q_{RM}$-measurements (Figure 3.9). After exclusion of tissue pieces containing lung-embedding foam, only 28 % of the total number of pieces remained for the analyzis of the mass of lung pieces as well as for $Q_{FM,Volume}$- and $Q_{FM,Mass,Volume}$-measurements.

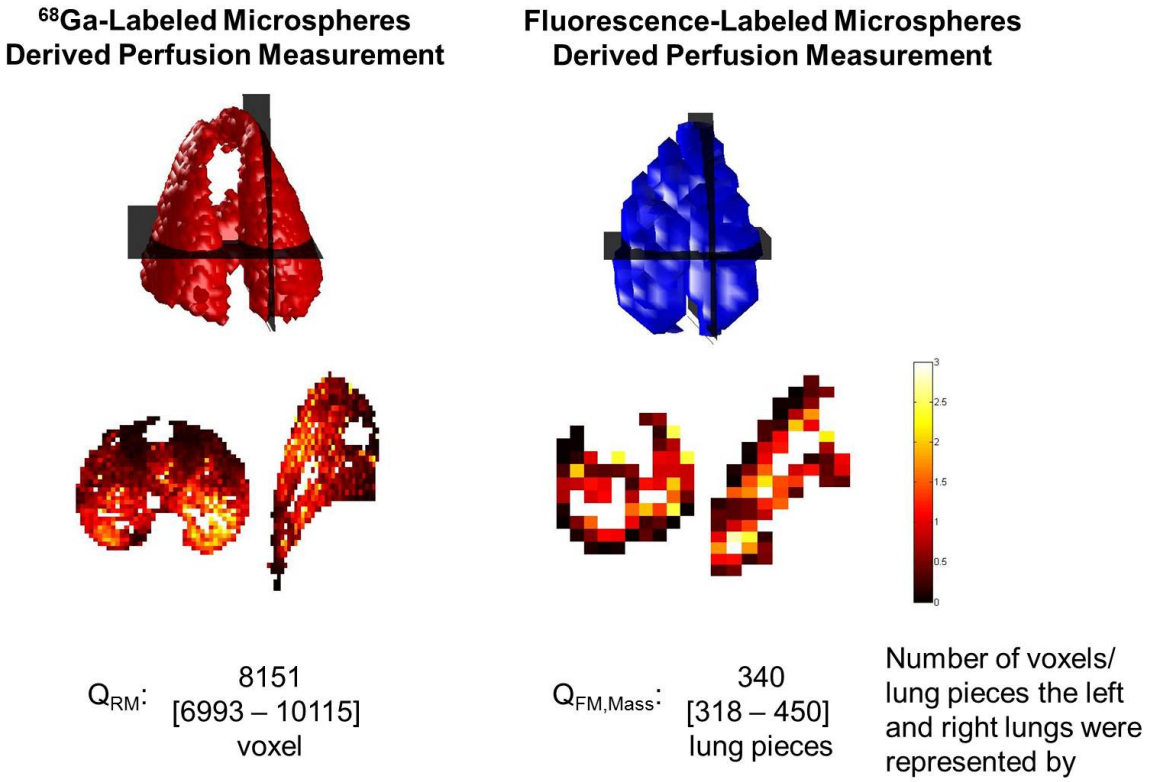


***Figure 3.9:*** *Three-dimensional contour of the left and right lungs of one representative animal (upper line) illustrating the position of the transversal and sagittal planes (lower line) of the distribution of perfusion assessed using $Q_{RM}$-measurements (left column) and $Q_{FM,Mass}$-measurements (right column) in BIPAP/APRV >60%, as well as number of voxel or lung pieces the left and right lungs were represented by.*

### 3.2.3 Lung Dimensions *ex vivo* and *in vivo*

Compared with lung dimensions assessed *in vivo* using $Q_{RM}$-measurements in BIPAP/APRV >60% and in BIPAP/APRV 0%, respectively, excitation and drying of the lungs caused an increase of the cranio-caudal distention, whereas the ventro-dorsal and left-right expansions decreased (Figure 3.10). Differences in lung distention between *in vivo* and *ex vivo* measurements were comparable between measurements in BIPAP/APRV 0% and BIPAP/APRV >60%, respectively (cranio-caudal distention: $p = 0.293$; ventro-dorsal distention: $p = 0.293$; left-right distention: $p = 0.248$). For $Q_{FM,Volume}$- and $Q_{FM,Mass,Volume}$-measurements, respectively, the exclusion of tissue pieces containing lung-embedding foam resulted in a reduction of the analyzed lung range to 82.6 [78.3 – 88.5] % of the longitudinal, 80.0 [75.0 – 81.8] % of the sagittal and 71.4 [66.7 – 80.0] % of the transversal lung expansions.

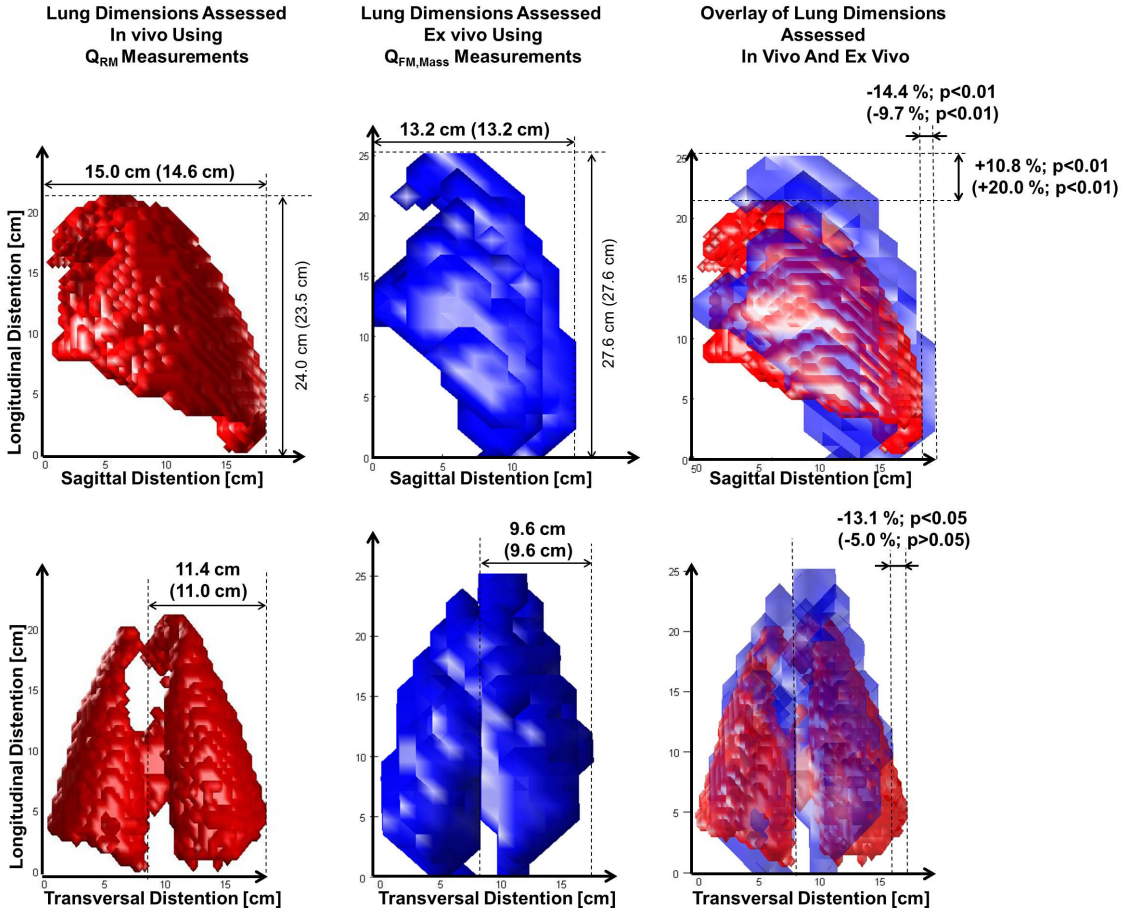


***Figure 3.10:*** *Three-dimensional illustration of the outer contours of the left and right lungs of one representative animal in lateral (upper line) and frontal projection (lower line) assessed in vivo using $Q_{RM}$-measurements in BIPAP/APRV >60% (illustrated in red, first column) and ex vivo using $Q_{FM,Mass}$-measurements (illustrated in blue, second column), respectively, as well as overlay of the 2 outer contours (third column). Median of lung expansions of all analyzed lungs in BIPAP/APRV >60% (and in BIPAP/APRV 0% in parentheses) as well as differences in lung dimensions between in vivo and ex vivo measurements in BIPAP/APRV >60% (and in BIPAP/APRV 0% in parentheses) as well as associated p-values are specified in the respective subplot.*

### 3.2.4 *Ex vivo* Measurements: Regional Differences in Lung Mass

Figure 3.11 shows the slopes of the linear regression of the mass of lung pieces fully containing of lung tissue and their spatial location along the ventro-dorsal and cranio-caudal gradient, respectively. Along the ventro-dorsal and cranio-caudal axes, respectively, the slopes of the linear regression lines were significantly different from zero ($p = 0.033$ and $p = 0.000$, respectively) and positive (0.0018 [0.0008 - 0.0033] g/cm and 0.0012 [0.0008 - 0.0022] g/cm, respectively).

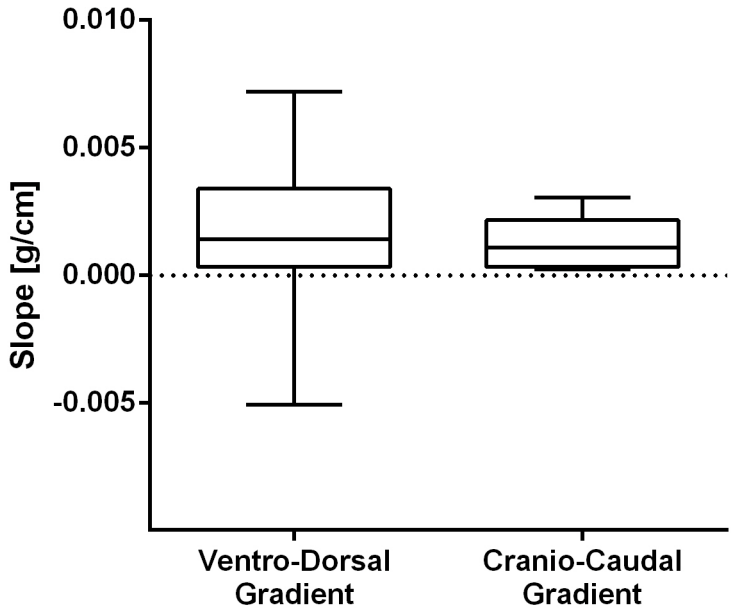


***Figure 3.11:*** *Box plot of the slope of the linear regression of the mass of lung pieces fully containing of lung tissue and their spatial location along the ventro-dorsal gradient (left) and cranio-caudal gradient (right), respectively, of all 13 analyzed lungs.*

### 3.2.5 *Ex vivo* versus *in vivo* Measurements of Pulmonary Perfusion

**Presence of Difference of Slopes form Zero**

Along the ventro-dorsal axis, all measurements revealed a significant difference of the slopes of linear regression of pulmonary blood flow and spatial location from zero (Figure 3.12). In BIPAP/APRV 0%, the significance level was lower for $Q_{FM,Mass}$-measurements as compared to all other analyzed measurements (Figure 3.12).

Along the cranio-caudal axis, only $Q_{FM,Volume}$-measurements revealed consistently with $Q_{RM}$- and $Q_{RM,downscaled}$-measurements, respectively, a significant difference of the slopes of the linear regression lines from zero in both ventilation modes. $Q_{FM,Mass}$- and $Q_{FM,Mass,Volume}$-measurements did not reveal a slope difference from zero in BIPAP/APRV 0%. However, in BIPAP/APRV 0% the significance level of the slope difference from zero differed between $Q_{FM,Volume}$- and $Q_{RM}$-measurements and between $Q_{FM,Volume}$- and $Q_{RM,downscaled}$-measurements (Figure 3.12).

**Magnitude of Slopes**

Along the ventro-dorsal axis and in both ventilation modes, $Q_{RM}$- and $Q_{FM}$-measurements revealed comparable slopes of linear regression of perfusion and spatial location, independent of the normalization technique of the $Q_{FM}$-measurements. $Q_{RM,downscaled}$-measurements revealed slightly lower slopes as compared to $Q_{RM}$-measurements in both ventilation modes.

Along the cranio-caudal gradient, only $Q_{FM,Volume}$-measurements showed comparable slopes of linear regression of perfusion and spatial location with $Q_{RM}$-measurements in both ventilation modes. In BIPAP/APRV >60%, $Q_{FM,Mass}$- and $Q_{FM,Mass,Volume}$-measurements revealed lower slopes as compared to $Q_{RM}$-measurements, whereas $Q_{RM,downscaled}$-measurements revealed slightly higher slopes.

**Slope variation after change of ventilation mode**

None of the measurement techniques revealed differences in the slopes of the linear regression of pulmonary blood flow and spatial location along the ventro-dorsal and cranio-caudal axes between ventilation in BIPAP/APRV 0% and BIPAP/APRV >60% ($p > 0.05$ for all 5 measurement techniques).

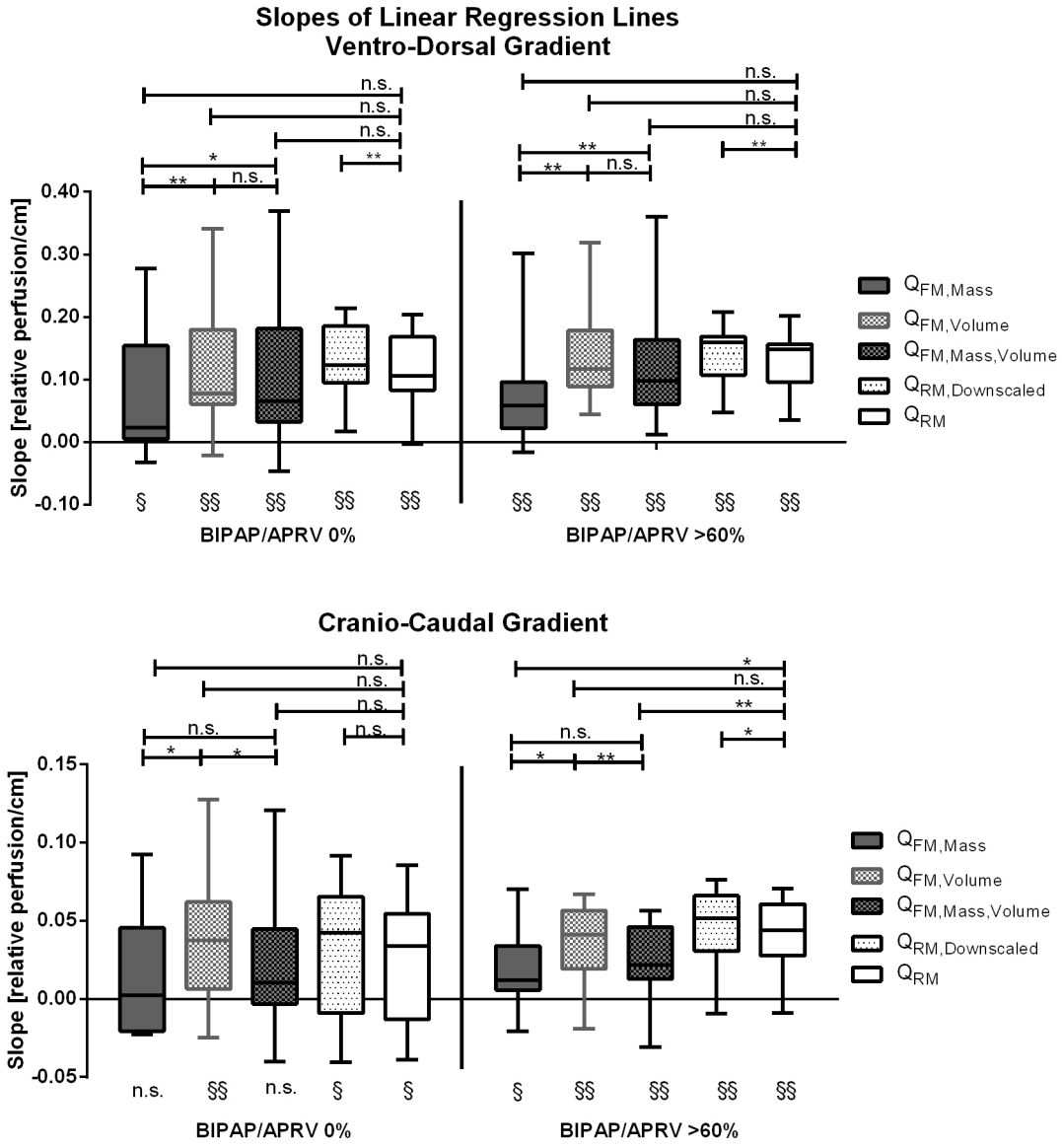


***Figure 3.12:*** *Box plot of the slopes of linear regression of pulmonary blood flow and spatial location along the ventro-dorsal (upper line) and cranio-caudal gradient (lower line), respectively, assessed using $Q_{RM}$- and all 3 $Q_{FM}$-measurements. * ($p < 0.05$) and ** ($p < 0.01$) (vs. $Q_{RM}$-measurement at the same ventilation mode and along the same axis. § ($p < 0.05$), §§ ($p < 0.01$), n.s. (no significant difference), (vs. zero).*

The Bland-Altman plots shown in Figure 3.13 illustrate the analyzis of the agreement of slopes of the linear regression of perfusion and spatial location along the ventro-dorsal and cranio-caudal gradients between $Q_{RM}$- and $Q_{FM,Mass}$-measurements, $Q_{RM}$- and $Q_{FM,Volume}$-measurements as well as between $Q_{RM}$- and $Q_{FM,Mass,Volume}$-measurements, respectively. Slope differences were highest between $Q_{FM,Mass}$- and $Q_{RM}$-measurements, as indicated by highest bias and largest limits of agreement. In comparison, the agreements of slopes between $Q_{RM}$- and $Q_{FM,Volume}$-measurements and between $Q_{RM}$- and $Q_{FM,Mass,Volume}$-measurements were better, as indicated by lower bias and lower limits of agreements (Figure 3.13).

The were no differences in the bias of the slope differences between $Q_{RM}$- and $Q_{FM,Volume}$-measurements from zero at any ventilation mode or perfusion gradient. In comparison, the bias of the slope differences between $Q_{RM}$- and $Q_{FM,Mass,Volume}$-measurements was unequal zero and positive for measurements along the cranio-caudal gradient in BIPAP/APRV >60%. The bias of the slope differences between $Q_{RM}$- and $Q_{FM,Mass}$-measurements was unequal zero and positive for all measurements except the measurements along the ventro-dorsal gradient in BIPAP/APRV >60% (Figure 3.13).

Along the ventro-dorsal gradient, the slope differences between all analyzed measurements determined in both ventilation modes decreased with increasing average slope values, as indicated by negative slopes of the linear correlation of slope differences and slope averages (slope of linear correlation different from zero: $p < 0.05$ for all 6 comparisons). No such trend was apparent for any of the 6 comparisons along the cranio-caudal gradient (slope of linear correlation different from zero: $p > 0.05$ for all 6 comparisons).

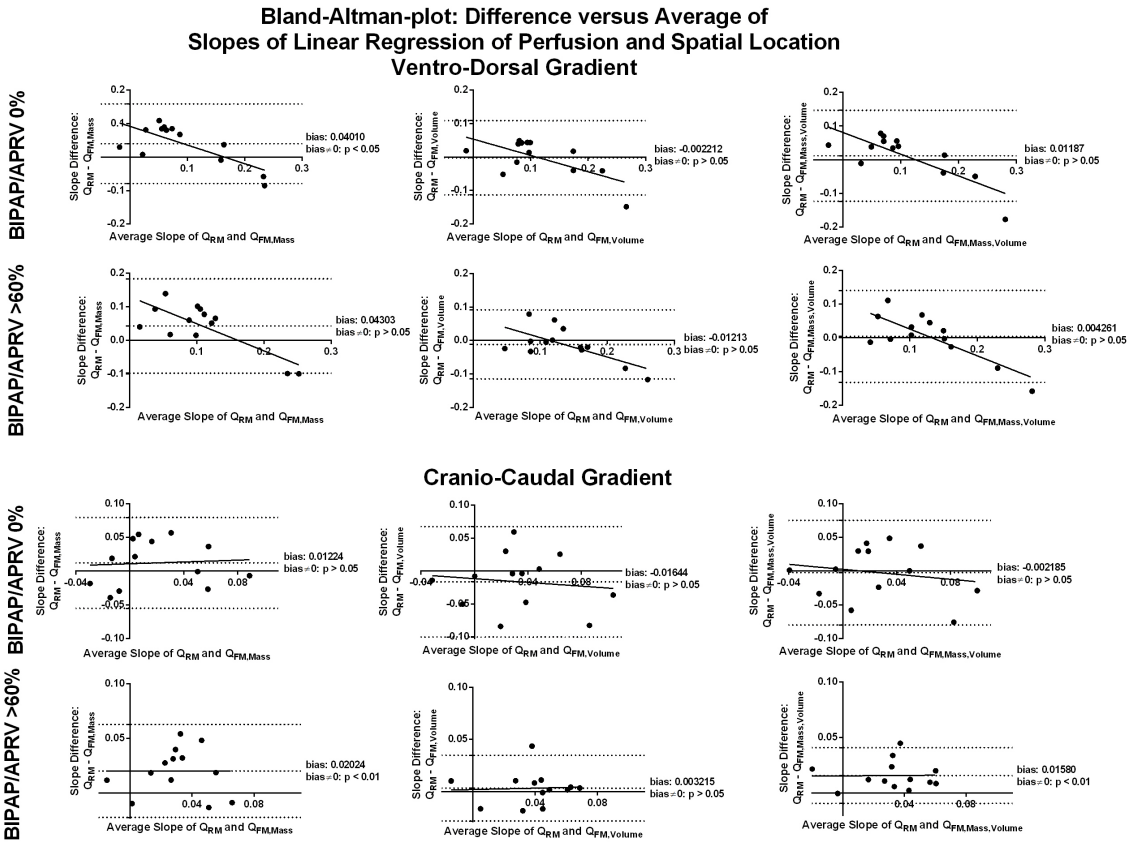


***Figure 3.13:*** *Bland-Altman plots of differences versus averages of the slopes of linear regression of perfusion and spatial location determined using $Q_{RM}$- versus $Q_{FM,Mass}$-measurements (1. column), versus $Q_{FM,Volume}$-measurements (2. column), and versus $Q_{FM,Mass,Volume}$-measurements (3. column), for regression along the ventro-dorsal gradient (upper panels) and along the cranio-caudal gradient (lower panels). Dashed lines represent bias as well as upper and lower limits of agreement.*

### 3.2.6 Pulmonary Perfusion Heterogeneity

Perfusion heterogeneity on a whole lung level was slightly but significantly lower in $Q_{RM,downscaled}$- as compared to $Q_{RM}$-measurements (Figure 3.14). In both ventilation modes, perfusion heterogeneity on a whole lung level was comparable between $Q_{RM,downscaled}$ and $Q_{FM,Mass}$-measurements, while $Q_{FM,Mass,Volume}$-measurements revealed lower values as compared to $Q_{RM,downscaled}$-measurements (Figure 3.14).

Regional perfusion heterogeneity was much lower in $Q_{RM,downscaled}$- as compared to $Q_{RM}$-measurements in both ventilation modes (Figure 3.14). Compared to $Q_{RM,downscaled}$-measurements in both ventilation modes, $Q_{FM,Mass,Volume}$- and $Q_{FM,Volume}$-measurements revealed comparable regional perfusion heterogeneities, while $Q_{FM,Mass}$-measurements revealed higher regional heterogeneity. Also in both ventilation modes, regional heterogeneity was higher in $Q_{FM,Mass}$-measurements as compared to $Q_{FM,Mass,Volume}$- and $Q_{FM,Volume}$-measurements, respectively, whereas it was comparable between $Q_{FM,Mass,Volume}$- and $Q_{FM,Volume}$-measurements (Figure 3.14).

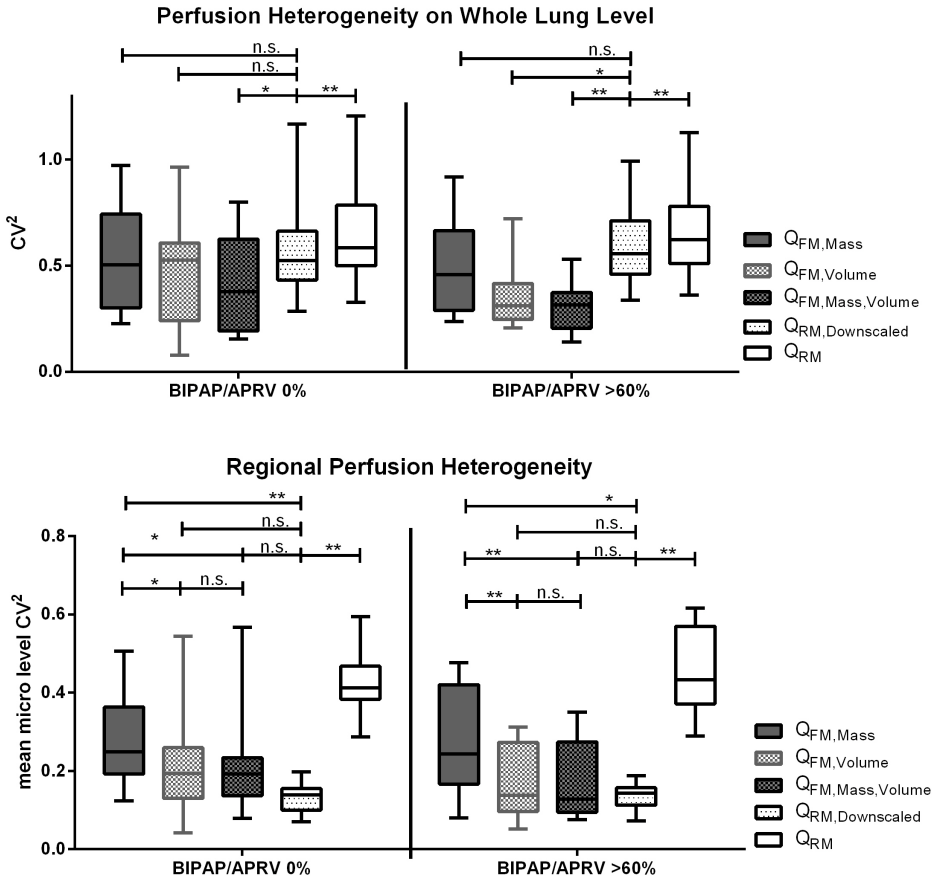


***Figure 3.14:*** *Box plots of perfusion heterogeneity on a whole lung level (upper line) and regional heterogeneity (lower line) of all analyzed lungs and animals. * ($p < 0.05$), ** ($p < 0.01$), n.s. (no significant difference), (vs. $Q_{RM,downscaled}$-measurement at the same ventilation mode and along the same gradient.*

# 4 Discussion

This section is divided in two sub-sections. The results of the study on the inflammatory impact of volutrauma and atelectrauma in ARDS will be discussed in the first part, while the results of the study on fluorescence-labeled microspheres derived perfusion measurements in ARDS will be discussed in the second sub-sections.

## 4.1 Volutrauma and Atelectrauma in ARDS

### 4.1.1 Major Findings

To the knowledge of the author, this is the first study comparing the impact of a comparable contribution of volutrauma and atelectrauma on pulmonary neutrophilic inflammation, perfusion, and aeration in a pig model of ARDS. We found that, as compared to atelectrauma, volutrauma caused:

1. Higher $^{18}$F-FDG uptake rates, mainly in mid-ventral, central, and mid-dorsal lung regions;
2. More tidal hyper-aeration and less tidal recruitment;
3. Decreased $F_{Blood}$ at comparable perfusion levels;
4. Decreased extent of non-aerated, but increased extent of normally and hyper-aerated lung regions.

### 4.1.2 Study Design

We used the double hit model for the induction of ARDS, since saline lung lavage used as first hit is associated with little tissue injury and a low inflammatory response of the lung (Rosenthal et al., 1998b). Thus, the impact of different injurious ventilation strategies (second hit) on the development of lung tissue injury and the associated inflammatory response can be ideally investigated (Matute-Bello et al., 2008b).

The double hit model of ARDS does not reproduce the initial pathophysiological mechanisms leading to ARDS, but reproduces surfactant depletion as an important consequence of the disease (Castillo et al., 2015). Therefore, the extent of edema is reduced as compared to findings in patients with ARDS (Cochrane and Revak, 1999). However, this is of advantage in this study since CT imaging does not allow the differentiation between collapsed lung regions and edema.

We used a randomized, parallel group design where each animal was used as its own control. Thus, a low number of experiments was sufficient to achieve a sample size of 5 lungs per group. Depleting surfactant in both lungs followed by mechanical ventilation of only one lung allowed the analyzis of the individual impact of only mechanical ventilation, especially when the same regions along the vertical gradient are compared. In addition, it prevents the impact of subject variability.

### 4.1.3 Ventilator Settings

The analyzis of the distribution of aeration compartments together with the analyzis of tidal changes of the pulmonary gas content confirmed that the applied ventilator settings were appropriate to reproduce volutrauma and atelectrauma. While the ventilated, VILI lungs of the volutrauma group were dominated by normally and hyper-aerated lung regions and more tidal hyper-aeration, the ventilated, VILI lungs of the atelectrauma group featured a large proportion of non-aerated lung tissue and a comparatively high extent of tidal recruitment. The appearance of non-aerated compartments and little tidal recruitment in some of the ventilated, VILI lungs of the volutrauma group were most likely a result of imprecise lung masks including small parts of blood vessels and small airways. Although tidal recruitment did not occur in volutrauma, we were not able to completely distinguish between the two mechanisms in the atelectrauma group. The ventilated, VILI lungs of the atelectrauma group featured little overdistension and tidal hyper-aeration. This was limited to the most non-dependent lung zones featuring the highest inflammatory response. Therefore, the small extent of volutrauma in the atelectrauma group may have caused an overestimation of the pulmonary $^{18}$F-FDG uptake in the atelectrauma group as compared to distinct investigations of the effects of opening and closing of alveoli.

Comparable low $V_T$ and low $\Delta P$ between groups indicate that the impact of both mechanisms was comparable. Consistently, the intensity delivered to the ventilated lung surface, which is defined as the mechanical power applied by the mechanical ventilator to the lung per gram of open, ventilated lung, was comparable between groups at the time point of the imaging sequence. The concept, that mechanical power might be a good determinant to characterize the impact of volutrauma and atelectrauma, has not yet been well investigated. It would be interesting to gain further experimental and clinical information about the correlation between mechanical power or intensity and the associated lung injury.

### 4.1.4 Impact of Volutrauma and Atelectrauma on Neutrophilic Inflammation

The higher inflammatory response of the ventilated, VILI lungs of the volutrauma as compared to the atelectrauma group, indicated by the higher $^{18}$F-FDG uptake rates, might be explained by different relative contributions of static and dynamic components of stress and strain.

In volutrauma, high static stress and strain likely determined the high uptake rates of $^{18}$F-FDG of the ventilated, VILI lungs. The very high proportion of normally and hyper-aerated regions indicated that the ventilated, VILI lungs were suffering from very high static strain. The increased inspiratory $P_{aw}$ is also an evidence for the higher contribution of static stress in volutrauma as compared to atelectrauma. The contribution of dynamic strain was much lower in volutrauma as compared to atelectrauma, as indicated by a lower extent of tidal hyper-aeration at comparable $V_T$ between both groups. The ventilated, VILI lungs of the volutrauma group might have been at their limits in terms of static stress and strain. It is possible that only an additional small contribution of dynamic strain in the central regions of the ventilated, VILI lungs of the volutrauma group might have worsened lung injury, causing the higher inflammatory response in those regions. Our findings suggest that the high impact of static stress and strain cause a higher risk for VILI in volutrauma areas, despite lower dynamic components. This might explain why high frequency oscillation was not found to improve 30 d mortality in patients with ARDS undergoing mechanical ventilation (Young et al., 2013), but even increases mortality in adults with moderate to severe ARDS (Ferguson et al., 2013), as compared to conventional mechanical ventilation using low $V_T$ and high PEEP.

In the atelectrauma group, static stress seemed to have only a minor impact on the inflammatory response of the ventilated, VILI lungs, as indicated by a very low extent of hyper-aerated regions. In fact, in ventilated, VILI lungs of the atelectrauma group, regional differences of the $^{18}$F-FDG uptake rates were very similar to regional extents of tidal recruitment. This suggests that tidal recruitment and therefore dynamic components of stress and strain likely determined pulmonary neutrophilic inflammation in atelectrauma. Alveolar instability induced by surfactant depletion and the associated collapse and reopening of alveoli during tidal breathing likely mainly determined the higher $^{18}$F-FDG uptake rates. Despite the use of low $V_T$, shear stress due to the presence of collapsed areas neighboring expanded alveoli might have also determined, at least in part, neutrophilic inflammation in the atelectrauma group, but most likely did not occur in volutrauma due to the negligible proportion of non-aerated tissue and tidal recruitment.

Collapse and reopening of alveoli likely not occurred in dorsal parts of the ventilated, VILI lungs of the atelectrauma group, since they were dominated by non-aerated regions and a low extent of tidal recruitment. The predominant part of those regions might therefore have remained collapsed throughout breathing. Consequently, the impact of both static and dynamic strain on the dorsal parts of the ventilated, VILI lungs of the atelectrauma group were likely very low, causing lowest $K_{iS}$ values. Our finding, that dynamic components of stress and strain seem to be the major determinant for the pulmonary inflammatory response, is in line with recent *in vivo* imaging studies in sheep, showing that in atelectatic lungs the dynamic components of lung strain seem to be more critical than the static ones (Wellman et al., 2014). Similarly, de Prost and coworkers showed in unilateral surfactant-depleted sheep lungs that dynamic components of stress and strain associated with tidal recruitment increased the inflammatory response especially in dependent, low aerated lung regions (de Prost et al., 2011).

Static components of stress and strain might have determined the tendency of slightly higher $K_{iS}$ values in ventral compared to dorsal regions of the non-ventilated, control lungs. Since the control lungs were not ventilated, the contribution of dynamic stress and strain is negligible. However, distending pressures have likely been higher in ventral regions of the control lungs due to gravitational dependence, leading to higher static strain and associated higher inflammatory responses of these lung parts.

### 4.1.5 Acquisition of the Distribution of $^{18}$F-FDG

The total tissue content of the imaged lung parts strongly differed between groups since dynamic PET scans capture only a 15 cm cranio-caudal lung field and since lung sizes differed strongly between animals of the atelectrauma and volutrauma group. The high tissue fraction of the ventilated, VILI lungs of the atelectrauma group had an impact on the high $K_i$ values of those lungs. We therefore calculated $K_{iS}$ values to allow inter-animal comparisons of $K_{iS}$. However, this correction might have introduced some error in cases of the occurrence of lung edema featuring similar density to collapsed lung tissue. Regional tissue fraction may have been overestimated in edematous regions, causing a potential underestimation of $K_{iS}$. Furthermore, the Sokoloff model applied in this study for the calculation of $K_i$ does not account for an extra-vascular, extra-cellular compartment of $^{18}$F-FDG distribution (edema). The model might therefore overestimate $K_i$ and $F_{Blood}$ in regions with edema, as shown by Dittrich and coworkers in an lavage model of ARDS in sheep followed by endotoxin administration (Dittrich et al., 2012). However, ARDS induced by endotoxin administration causes more edema production as compared to the double hit model used in this study (Castillo et al., 2015). In addition, CT-derived mass of the whole ventilated, VILI lungs and of the non-ventilated, control lungs was comparable between groups. Therefore, the impact of edema on the calculation of $F_{Tissue}$ and consequently on $K_{iS}$ was likely in the same magnitude in both groups.

Local perfusion is an important determinant for the inflammatory response of the lung and the associated uptake rate of $^{18}$F-FDG. Perfusion significantly influences both the load of neutrophils and their supply with $^{18}$F-FDG (Costa et al., 2010). In this study, perfusion was comparable between the ventilated, VILI lungs of the volutrauma and atelectrauma group, both on a whole lung level and on a regional level, implying that regional differences in $K_{iS}$ were not a result of differences in regional perfusion.

### 4.1.6 Pulmonary Perfusion Distribution

Perfusion of the ventilated, VILI lungs was lower as compared to the non-ventilated, control lungs in both groups. In volutrauma, this was most likely determined by higher $P_{aw}$ in the ventilated, VILI lungs as compared to the non-ventilated lungs, and associated higher transpulmonary pressures. In contrast to the well accepted concept of increasing perfusion with increasing gravitation dependence explained by West (West, 1978), we saw no gravitationally-dependent differences in lung perfusion neither in the non-ventilated, control lungs of both groups nor in the ventilated, VILI lungs of the atelectrauma group. This might have been caused by regional interactions between hydrostatic and transpulmonary pressures. Regional differences in the transpulmonary pressure are not distinguishable due to missing techniques or regional measurements. In addition, hypoxic pulmonary vasoconstriction most likely contributed to lower perfusion of dorsal parts of the ventilated, VILI lungs of the atelectrauma group.

### 4.1.7 Lung Mechanics and Gas Exchange

We kept both $V_T$ and ΔP approximately constant during the intervention phase of the experiments. However, comparable $V_T$ was of higher relevance in order to keep lung strain similar between groups. Since ΔP is a surrogate of dynamic stress, the increase in ΔP over time in the atelectrauma but not in the volutrauma group suggests that dynamic stress associated with tidal recruitment and tidal hyper-aeration increased over time in atelectrauma, but not in volutrauma, and resulted in higher dynamic stress at the end of the 4 h ventilation period in the atelectrauma group. Although a higher dynamic stress is associated with a higher inflammatory response, we found lower inflammatory values in the ventilated, VILI lungs of the atelectrauma as compared to the volutrauma group. This suggests that differences in the inflammatory response of the lung would have been even more pronounced between volutrauma and atelectrauma if ΔP would have been comparable between groups.

The non-significant trend towards a higher $PaCO_2$ in volutrauma as compared to atelectrauma was presumably a result of increased ventilation pressures and a resulting redistribution of perfusion towards the non-ventilated, control lungs, i.e. a deadspace effect. However, an increased $PaCO_2$ has been shown to have protective effects (Curley et al., 2010), and is therefore associated with a lower inflammatory response of the lung. This suggests that differences in the measured $^{18}$F-FDG uptake rates would likely have been even higher if $PaCO_2$ would have been comparable between groups.

### 4.1.8 *Ex vivo* Analysis versus *in vivo* Analysis of Pulmonary Inflammation

In contrast to the *in vivo* results on pulmonary inflammation, the *ex vivo* analyzis of the protein concentrations of IL-6 and IL-8 did neither reveal differences between the ventilated, VILI lungs and the non-ventilated, control lungs in volutrauma or atelectrauma, respectively, nor between the ventilated, VILI lungs of both groups. The different findings might be a result of different regions analyzed for *ex vivo* and *in vivo* acquisition. Lung tissue sampled of the upper lobes where analyzed for molecular biology. In comparison, only a 15 cm cranio-caudal field of view right above the diaphragms was assessed by PET/CT scanning, not covering the whole upper lobes.

The expression of TNF-α was below the detection limits, presumably because of the very short time course of gene transcription and translation. The protein concentration of TNF-α might have been already down regulated at the time point of tissue sampling.

### 4.1.9 Limitations

This study has several limitations.

First, compared to the clinical scenario, a relatively short period of mechanical ventilation of 4 h was chosen. The peak of the inflammatory impact of atelectrauma might occur later than that of volutrauma and after more than 4 h of injurious ventilation. However, the increase in ΔP in the atelectrauma group after 1 h suggests that tidal recruitment and derecruitment already occurred during the time course of the experiment. This is in line with a study performed by Musch et al. (Musch et al., 2007), where dynamic recruitment and derecruitment already caused an increase in $K_i$ after 120 min of injurious ventilation. Furthermore, study periods of 4 might not be long enough to investigate the development of the complex injury and all clinical syndromes associated with ARDS. It can take up to 7 days in patients with ARDS (Ware and Matthay, 2000). Animals would likely not have survived a longer study period due to the development of severe gas exchange failure. However, it cannot be completely ruled out that longer periods might have resulted in different findings.

Second, although volutrauma and atelectrauma often occur at the same time in different regions of the lung, we tried to separate these two phenomena as far as possible in order to study the associated mechanisms as well as their individual impact on the inflammatory response of the lung. However, in the ventilated, VILI lungs of the atelectrauma group, hyper-aeration of the most non-dependent lung regions and associated overdistension could not have been completely avoided. This might have

triggered an additional inflammation not purely associated with atelectrauma. However, this may have led to an overestimation of the pulmonary $^{18}$F-FDG uptake in the atelectrauma group, and consequently an underestimation of the differences between volutrauma and atelectrauma.

Third, we were not able to prevent a potential inflammatory cross talk between left and right lungs. Lung volumes and associated distending pressures of the ventilated, VILI lungs differed significantly between volutrauma and atelectrauma, affecting the non-ventilated, control lungs to differing extent. Since the non-ventilated, control lungs were not ventilated but perfused, hypoxemia might have increased neutrophilic inflammation in those lungs. In addition, neutrophilic inflammation of the control lungs might also have been increased by recruitment maneuvers, which were performed every 30 min in order to minimize lung collapse. However, these maneuvers were performed in the same way in both groups. Therefore, those mechanisms should have affected both groups and the interpretation of the comparative contribution of volutrauma and atelectrauma to VILI was most likely not affected.

Fourth, data were obtained under extreme conditions of overdistension and lung collapse, which were more extreme than common in the ICU. The used ventilator settings do not reproduce clinical practice but were used to better differentiate the mechanisms induces by volutrauma and atelectrauma, respectively.

Fifth, pulmonary $^{18}$F-FDG uptake cannot be solely ascribed to neutrophils, but also other inflammatory cells and non-inflammatory cells, such as type 2 epithelial cells, take up $^{18}$F-FDG (Saha et al., 2013). However, neutrophils are an essential component of lung injury. It has been shown that in the lung $^{18}$F-FDG is mainly taken up by neutrophils (Musch et al., 2007; Saha et al., 2013). Furthermore, pulmonary $^{18}$F-FDG uptake has been shown to be a reliable marker for neutrophilic inflammation in injured lungs (Jones et al., 2002; Musch et al., 2007; Saha et al., 2013).

Sixth, the dynamic PET scans acquired in this study captured only a 15 cm cranio-caudal field of view. It was therefore not possible to study the neutrophilic inflammation of the whole lung. Cranial parts of the upper lobes and caudal parts of the lower lobes were not assessed. We assumed that the captured 15 cm cranio-caudal lung parts were representative for the neutrophilic inflammation of the whole lungs, which has not been studied yet. However, currently no method is available that captures the dynamics of the neutrophilic inflammation in the whole lung *in vivo*.

Seventh, $K_i$ values were corrected for tissue fractions in order to account for the extreme differences in gas fraction between groups. The tissue fraction is majorly determined by the gas content of the scanned region, which is determined by CT. However, such density estimations by CT depend on different factors, including voxel size, characteristics of the CT scanner and parameters used for the reconstruction of the acquired CT data (Reske et al., 2008; Levi et al., 2012). We aimed to minimize those artifacts by using the same CT scanner for all animals, reconstructing the CT data with the same voxel size and using appropriate reconstruction parameters. We used smooth kernels that have been shown to be appropriate for the analyzis of CT scans and the assessment of hyper-aerated regions in injured lungs (Boedeker et al., 2004). Nevertheless, inaccuracies in the calculation of tissue density and of tissue fraction might have occurred. The normalization of the $^{18}$F-FDG uptake ratios to tissue fraction could therefore have introduced measurement artifacts.

Eighth, tidal recruitment and hyper-aeration as dynamic VILI mechanisms were calculated based on static CT scans, which were obtained at end-expiratory and end-inspiratory breath holding maneuvers. Static CT scanning does not represent strictly static conditions since lung aeration may have changed during the breath holding maneuver. Dynamic CT scans would have overcome such limitation. However, dynamic CT scans capture only a very limited cranio-caudal part of the lung of about 1 cm. Since dynamic changes of lung aeration occurred to different extents in the distinct regions of the lungs, dynamic CT scanning would have not been a valid alternative for the acquisition of tidal changes of lung aeration in this study.

### 4.1.10 Conclusion

The pulmonary neutrophilic inflammation associated with volutrauma and atelectrauma is caused by several factors, including static as well as dynamic stress and strain of lung units and ΔP. In this experimental model of ARDS, volutrauma caused a higher inflammatory response as compared to atelectrauma, despite comparable low $V_T$, lower ΔP, and comparable perfusion. In volutrauma, the inflammatory response was mainly determined by static stress and strain while the dynamic component was comparatively low. This evidences the important role of static components of stress and strain, which seem to be the more important mechanisms of VILI as compared to the dynamic components, in this model of ARDS. According to the findings of this study, lower PEEP values should be set in order to prevent volutrauma and its associated static stress and strain, even though this could cause a higher risk of atelectrauma.

## 4.2 Fluorescence-Labeled Microspheres Derived Perfusion Measurements in ARDS

### 4.2.1 Major Findings

To the knowledge of the author, this is the first study comparing *in vivo* perfusion measurements using $^{68}$Ga-labeled microspheres and PET/CT with *ex vivo* measurements using fluorescence-labeled microspheres in a pig model of ARDS. We found that in injured pig lungs:

1. The resolution of *ex vivo* perfusion measurements using fluorescence-labeled microspheres was lower than that of *in vivo* measurements using $^{68}$Ga-labeled microspheres and PET/CT.
2. Extraction of the lungs and further processing for *ex vivo* analyzis of the distribution of fluorescence-labeled microspheres causes lung deformation as compared to *in vivo*.
3. *Ex vivo* measurements of the mass of lung pieces fully containing of lung tissue and therefore featuring approximately comparable tissue volume were not homogeneous but showed a gradient with higher mass in dorsal and caudal as compared to ventral and cranial regions, respectively.
4. Normalization of fluorescence-labeled microspheres derived measurements using the volume of lung pieces resulted in better agreement of perfusion gradients with *in vivo* PET/CT measurements as compared to $Q_{FM,Mass}$- and $Q_{FM,Mass,Volume}$-measurements.
5. $Q_{RM}$-measurements showed higher heterogeneity on a whole lung level as compared to $Q_{RM,downscaled}$-measurements featuring a resolution comparable to that of fluorescence-labeled microspheres derived measurements.
6. As compared to $Q_{RM,downscaled}$-measurements, $Q_{FM,Volume}$-, and $Q_{FM,Mass,Volume}$-measurements featured comparable regional heterogeneity, respectively, whereas $Q_{FM,Mass}$-measurements featured higher regional heterogeneity. $Q_{FM,Mass}$-measurements featured higher regional heterogeneity as compared to $Q_{FM,Volume}$- and $Q_{FM,Mass,Volume}$-measurements, respectively.

### 4.2.2 Study Design

We used a saline lung lavage model of experimental ARDS in the perfusion measurements study since the associated little tissue injury and the low pulmonary inflammatory response causes little inflammatory deposition. Therefore, after extraction and drying of the lungs, the mass of lung pieces is potentially less affected by residues of inflammatory cells, mucus, and secretion and expression of edema.

We used a crossover design in order to reduce the number of experiments and animals. This model was suitable for this study since hemodynamics remained fairly stable and since the impairment of lung function was maintained by periodic derecruitment maneuvers. Due to the long shelf life of fluorescent microspheres and due to their availability in different colors, several perfusion measurements are possible in the same animal.

### 4.2.3 Methodical Aspects

We used a simplification for the quantification of perfusion distribution and assumed a linear correlation of relative perfusion and spatial location. A vertical gradient of pulmonary perfusion with higher perfusion of gravitational dependent as compared to non-dependent lung regions is generally accepted in supine position (Musch et al., 2002). It can be explained by a considerable impact of gravity together with the impact of structural factors, such as the anatomy of the vascular tree, and active regulation (Glenny et al., 1997; Glenny et al., 2007). In transversal slices of healthy, isolated and blood-perfused dog lungs, a linear regression analyzis of flow and spatial location along ventro-dorsal axis provided a better fit as compared to a quadratic fit (Beck, 1990).

We compared different normalization techniques of *ex vivo* measurements using fluorescence-labeled microspheres with *in vivo* measurements of pulmonary perfusion distribution using $^{68}$Ga-labeled microspheres and PET/CT scanning in ARDS lungs. Despite the disadvantage that PET/CT measurements of lung perfusion might overestimate lung tissue density in edematous regions and therefore underestimate regional perfusion, it has been shown to be an adequate method to assess regional pulmonary perfusion in ARDS lungs (Richter et al., 2015; Beck, 1987b; Richard et al., 2002). PET/CT scanning has the considerable advantage that it provides *in vivo* measurements at the time point at which perfusion is of interest. PET/CT measurements of the distribution of $^{68}$Ga-labeled microspheres were therefore used as reference for the detection of the distribution of pulmonary perfusion.

### 4.2.4 Magnitude of perfusion gradients

All measurements revealed a perfusion gradient along the ventro-dorsal axis, as indicated by a significant difference of the slopes of linear regression of pulmonary perfusion and spatial location from zero, independent of the normalization technique of the fluorescence-labeled microspheres measurements and of the resolution of the $^{68}$Ga-labeled microspheres measurements. In all measurements, the slopes of the linear regression lines along the ventro-dorsal axis were positive, indicating higher perfusion in dorsal compared to ventral regions. There were no differences in the magnitude of perfusion gradients along the ventro-dorsal axis between $Q_{RM}$-measurements and all fluorescence-labeled microspheres measurements. However, as compared to $Q_{FM,Mass}$-measurements, the Bland-Altman analyzes revealed a better agreement between fluorescence-labeled and $^{68}$Ga-labeled microspheres measurements when the fluorescence signals were corrected for the respective volume of a lung piece or for its volume and mass, as indicated by no or less difference in the bias of the slopes from zero and lower limits of agreements. The high and positive bias of slope differences between $Q_{RM}$- and $Q_{FM,Mass}$-measurements along both gradients and in both ventilation modes indicate that mass normalization of measurements of the distribution of fluorescence-labeled microspheres tends to reduce perfusion gradients as compared to $Q_{RM}$-measurements.

Along the cranio-caudal axis, only $Q_{RM}$-, $Q_{RM,downscaled}$-, and $Q_{FM,Volume}$-measurements consistently revealed perfusion gradients in both ventilation modes, as indicated by significant differences of the slopes of linear regression of pulmonary perfusion and spatial location from zero. In contrast, $Q_{FM,Mass}$- and $Q_{FM,Mass,Volume}$-measurements in BIPAP/APRV 0% did not indicate a perfusion gradient along the cranio-caudal axis. $Q_{RM}$-, $Q_{RM,downscaled}$-, and $Q_{FM,Volume}$-measurements consistently showed higher perfusion in caudal as compared to cranial lung regions, as indicated by positive slopes along the cranio-caudal axis. While the magnitude of the perfusion gradients along the cranio-caudal axis were comparable between $Q_{RM}$- and $Q_{FM,Volume}$-measurements in both ventilation modes, $Q_{RM,downscaled}$-measurements showed slightly higher perfusion gradients compared to $Q_{RM}$-measurements in BIPAP/APRV >60%. Consistently, also the Bland-Altman analyzis revealed good agreement between $Q_{RM}$- and $Q_{FM,Volume}$-measurements, as indicated by no difference in the bias of the slopes from zero and low limits of agreements.

### 4.2.5 Impact of Resolution on Differences in Perfusion Gradients

The resolution of the $Q_{RM}$-measurements was higher compared to that of the fluorescence-labeled microspheres derived perfusion measurements. However, downscaling the $Q_{RM}$-measurements to the resolution of the $Q_{FM}$-measurements had no effect on the presence of perfusion gradients along the ventro-dorsal and cranio-caudal axes and only slightly changed its magnitude. Therefore, the much higher resolution of the $Q_{RM}$-measurements as compared to the $Q_{FM}$-measurements seems not to be the crucial factor for the detected differences in the presence and magnitude of perfusion gradients. However, if no linear perfusion gradient can be assumed, differences in resolution might have a much higher impact on the determination of the distribution of pulmonary blood flow.

### 4.2.6 Impact of Lung Deformation on Perfusion Measurements

The extraction of the lungs followed by drying at a pressure of 25 $cmH_2O$ in upright position, which entailed significantly different pressure conditions compared to *in vivo* conditions, caused deformation of the lungs. As compared to their *in vivo* dimensions, the longitudinal expansion increased while the sagittal and transversal expansions decreased. Assuming an unchanged perfusion distribution, an increase of the lung expansion is associated with a decrease of the perfusion gradient. Therefore, an increase in the cranio-caudal distention in the course of the extraction and drying of the lungs may have contributed to the lower perfusion gradients assessed in $Q_{FM,Mass}$- as compared to $Q_{RM}$-measurements in BIPAP/APRV >60%, respectively. However, as compared to measurements in BIPAP/APRV >60%, no differences in the perfusion gradients along the cranio-caudal axis were assessed between $Q_{FM,Mass}$- and $Q_{RM}$-measurements in BIPAP/APRV 0%, despite a comparable increase in the longitudinal lung distention. Furthermore, despite an increase of the sagittal lung distentions, there were no differences in the perfusion gradients along the ventro-dorsal axis between *ex vivo* und *in vivo* measurements. Therefore, deformation of the lungs in the course of their extraction and drying process seems not to be the major determinant for the assessed differences in perfusion gradients between fluorescence-labeled and $^{68}$Ga-labeled microspheres derived measurements.

### 4.2.7 Impact of Mass Distribution on Perfusion Measurements

The *ex vivo* analyzis of mass of lung pieces fully containing of lung tissue and therefore featuring approximately comparable tissue volume revealed a mass gradient along the ventro-dorsal and cranio-caudal axes, as indicated by significant differences of the slopes of the linear regression of mass and spatial location of lung pieces along both gradients. Mass increased from gravitational non-dependent, ventral to gravitational dependent, dorsal regions, as well as from cranial to caudal regions, as indicated by the positive slopes of the linear regression lines. Therefore, in contrast to the assumption suggested for the analyzis of fluorescence measurements in healthy lungs, in injured lungs the mass of a lung piece seems not to be directly proportional to the containing tissue volume.

The mass gradients of pieces featuring comparable tissue volume have likely been caused by the combination of two aspects: first, drying acutely injured lungs at high pressure might not have been sufficient to fully reopen all alveoli. A potential higher extent of atelectasis in dorsal and caudal as compared to ventral and cranial regions, respectively, could explain the mass gradients along both gradients. Second, especially due to the induction of ARDS, lung pieces might not only be composed of lung tissue but also by accumulation of inflammatory deposition, altering the mass of lung pieces.

Heavy walls of small airways, capillaries, connective tissue or scar tissue likely altered the measured mass of lung pieces. However, the impact of those additive factors is presumably heterogeneous and might cause higher standard deviation of the mass of all lung pieces but might not have an impact on the observed mass gradients. The impact of heavy cartilage rings and smooth muscle surrounding large bronchi on the mass of lung pieces can be neglected since pieces featuring big airways were excluded from the analyzis. Also, the impact of heavy pleura wall can be ruled out since no edge pieces were analyzed for its mass. Since this study was done retrospectively, the individual impact of inhomogeneous lung tissue density and further factors contributing to the mass of lung pieces cannot be determined.

Compared to $Q_{FM,Mass}$-measurements, $Q_{FM,Volume}$-measurements correlated better with $Q_{RM}$-measurements, as indicated by a better agreement of the presence and magnitude of the perfusion gradients along the ventro-dorsal and cranio-caudal axes. This indicates that the volume of a lung piece might be a better surrogate for containing tissue content as compared to the mass, although volume normalization of fluorescence measurements would not account for inhomogeneous tissue density. A better correlation of $Q_{FM,Volume}$- with $Q_{RM}$-measurements as compared to $Q_{FM,Mass,Volume}$-measurements indicates that normalization of fluorescence-labeled microspheres derived perfusion

measurements to the mass and volume of a lung piece is less appropriate as compared to only volume normalization.

Only a smaller portion of the lung was analyzed in $Q_{FM,Volume}$- and $Q_{FM,Mass,Volume}$-measurements as compared to $Q_{FM,Mass}$-measurements since all edge pieces were discarded and only pieces fully containing of lung tissue were analyzed. Especially bigger dorsal and caudal lung parts were not considered. However, the exclusion of outermost lung regions should not importantly affect perfusion gradients as long as the used assumption of linear correlation of perfusion and spatial location is adequate.

Further studies would be necessary to provide further inside about which factors majorly determined the mass gradients and the associated greater weight range of tissue pieces featuring comparable volume in severely injured lungs as compared to pieces of healthy lung, as assessed by Hübler and coworkers in their ARDS sheep study (Hübler et al., 1999).

### 4.2.8 Heterogeneity

The findings, that heterogeneity of the whole lung and regional heterogeneity of $^{68}$Ga-labeled microspheres derived perfusion measurements are dependent on resolution, are in line with the results of other studies showing that resolution is a major determinant of the detected perfusion heterogeneity and that a decrease in resolution strongly decreases the heterogeneity of pulmonary blood flow measurements (Melo et al., 2010; Venegas et al., 1994). PET/CT measurements of the emitted radioactivity, which were performed during mechanical ventilation, had to be corrected for tissue attenuation. This was done by normalization of the emitted radioactivity to lung tissue density, which was quantified by CT scanning with breath hold maneuvers at end-expiratory lung volume. The registration of the two datasets acquired at slightly different lung volumes and with differing impact of lung motion, together with the impact of lung segmentation inaccuracies, most likely caused registration artifacts. In addition, regional image noise might have arisen from non-uniformity of the sensitivity of the PET camera and edge blurring effects created by the low spatial resolution of the camera (Venegas et al., 1994). We used a filtered back projection in the course of the reconstruction of the PET data, which was developed to reduce noise. However, such filter-based approaches are limited by the balance between reduction of noise, high resolution, and speed (Obi et al., 2000). For calculation of $Q_{RM,downscaled}$-data, $Q_{RM}$-measurements of several voxel were averaged. This has presumably reduced the impact of registration artifacts and regional image noise.

Despite comparable resolution of $Q_{RM,downscaled}$-measurements and fluorescence-labeled microspheres measurements of pulmonary perfusion, heterogeneity on a whole lung level was lower in $Q_{FM,Volume}$- and $Q_{FM,Mass,Volume}$-measurements as compared to $Q_{RM,downscaled}$-measurements, respectively. Such differences seem to be an effect of the different perfusion gradients and the associated differences in the regional variance of the data. Venegas and Galletti proposed to remove the impact of the perfusion gradient along the ventro-dorsal axis on estimations of perfusion heterogeneity by subtracting the plane featuring the best-fit vertical gradient from the three-dimensional dataset before calculating the heterogeneity index (Venegas and Galletti, 2000). However, we did not only observe perfusion gradients along the gravitational dependent plane, but also along the cranio-caudal axis. We therefore determined regional heterogeneity by calculation of the mean heterogeneity within blocks of approximately the same size (24 x 24 x 24 $mm^3$ in fluorescence derived and $Q_{RM,downscaled}$-measurements; 24.36 x 24.36 x 25 $mm^3$ in $Q_{RM}$-measurements) to consider mean regional perfusion within each block. Such block sizes were found to be an acceptable compromise between, on the one hand, the aim to quantify lung function in lung volumes as small as possible, and, on the other hand, lung volumes being big enough to reduce the impact of statistical noise and the limited spatial resolution of the measurement techniques (Xu et al., 2000). Under consideration of regional differences in lung perfusion, there were no differences in regional perfusion heterogeneity between $Q_{FM,Volume}$- and $Q_{RM,downscaled}$- as well as between $Q_{FM,Mass,Volume}$- and $Q_{RM,downscaled}$-measurements, respectively. This might have been caused by the balance between noise induced by PET/CT and fluorescence-labeled microspheres derived perfusion measurements, respectively, and by actual heterogeneity detected by measurements at different resolutions. Different structural factors and different active regulatory mechanisms of the pulmonary vasculature, such as hypoxic pulmonary vasoconstriction, act on different length scales and determine different heterogeneity levels at different spatial resolution (Glenny et al., 2000b). Future studies would be necessary to determine the contribution of artifacts induced by the measurement technique itself, which could then be used for the correction of the total measured heterogeneity.

$Q_{FM,Mass}$-measurements revealed higher regional heterogeneity as compared to $Q_{FM,Volume}$- and $Q_{FM,Mass,Volume}$-measurements, respectively. This could have been caused by the inappropriate normalization of the fluorescence measurements for inhomogeneous tissue content or by the higher sample size due to inclusion of outermost lung pieces or both.

### 4.2.9 Limitations

This study has two limitations.

First, we used a saline lung lavage model for the induction of ARDS, which is associated with a low pulmonary inflammatory response and only mild to moderate lung injury. When other injury models are applied, different effects on the variation of the lung tissue mass are possible and therefore differing normalization of the fluorescence measurements could correspond best with the *in vivo* measurements of the distribution of pulmonary blood flow.

Second, we assumed a linear correlation of perfusion and spatial location and of mass and spatial location. If this assumption was not valid, the exclusion of outermost lung regions induced by the volume normalization may have introduced a systematic error in perfusion gradient measurements. In further studies the volume of outermost lung pieces should be measured such that no lung containing pieces have to be excluded from the analyzis. This would also allow a differentiation of the impact of inhomogeneous tissue density and of inflammatory deposition on the mass of pieces of injured lungs.

### 4.2.10 Conclusion

In pig lungs injured by saline lavage, the mass of dried lung tissue pieces featuring approximately comparable tissue volume was higher in dorsal and caudal as compared to ventral and cranial regions, respectively. Therefore, contradictory to assumptions used for the analyzis of fluorescence-labeled microspheres derived perfusion measurements in heathy lungs, in ARDS pig lungs, the mass of a lung piece seems not to be directly proportional to the containing tissue volume. When applying volume normalization, *ex vivo* measurements of the distribution of fluorescence-labeled microspheres revealed comparable results as *in vivo* measurements of the distribution of $^{68}$Ga-labeled microspheres in respect to the presence and magnitudes of ventro-dorsal and cranio-caudal perfusion gradients. Consequently, $Q_{FM,Volume}$-measurements can be used interchangeably with $Q_{RM}$-measurements for the determination of perfusion gradients, despite a much lower resolution of the *ex vivo* measurement and the occurrence of lung deformation induced by lung extraction and drying. A reduction of the resolution of *in vivo* perfusion measurements and adjustment to that of the *ex vivo* measurements caused a reduction of both global and regional heterogeneity. Volume normalization of fluorescence-labeled microspheres derived perfusion measurements resulted in comparable global and regional perfusion heterogeneity of *ex vivo* and *in vivo* perfusion measurements at comparable resolution.

# 5 Summary

**Background:** The recent development and advancement of new *in vivo* imaging techniques, such as computed tomography (CT) and positron emission tomography (PET), have allowed to gain a better understanding of the pathophysiology of the acute respiratory distress syndrome (ARDS). PET/CT measurements revealed that ARDS is determined by alterations in both aeration and perfusion, which impairs gas exchange. Therefore, mechanical ventilation is frequently required in order to maintain gas exchange. However, the pathophysiology of ARDS and the potential injurious impact of mechanical ventilation in patients with ARDS are still not fully understood.

**Objective:** PET/CT imaging techniques were used to quantify alterations in lung aeration, neutrophilic inflammation and pulmonary perfusion in experimental studies of ARDS. Two interrelated studies were conducted.

The aim of the first substudy was to determine the relative contribution of the two main mechanisms of ventilator induced lung injury (VILI), cyclic closing and opening of alveoli (atelectrauma) and alveolar overdistension (volutrauma), to the pro-inflammatory response of the lung in an experimental model of ARDS.

The aim of the second substudy was to validate the use of fluorescence-labeled microspheres for measurements of pulmonary perfusion distribution in acutely injured lungs. This substudy investigated whether such *ex vivo* measurements of the distribution of lung perfusion could be used as alternative to *in vivo* measurements using gallium-68 ($^{68}$Ga)-labeled microspheres and PET/CT in experimental ARDS.

**Methods:** Two substudies were performed in anesthetized, intubated and mechanically ventilated pigs. ARDS was induced by repetitive, saline lung lavage.

In the first substudy, 10 animals were included. The lungs were recruited and a decremental positive end-expiratory pressure (PEEP) trial was performed. The pigs were randomly assigned to 4 hours of mechanical ventilation of the left, VILI lungs with either high PEEP set above the level where dynamic compliance increased more than 5 % during PEEP trial (volutrauma), or low PEEP (atelectrauma) to achieve comparable driving pressures (defined as difference between peak airway pressure and PEEP) and tidal volumes of 3 mL/kg predicted body weight between groups. The right lungs served as control and were kept under a continuous positive airway pressure of 20 cm$H_2O$. An extra-corporeal device was used to remove carbon dioxide. PET/CT scans were performed after

intravenous injection of $^{68}$Ga-labeled microspheres and 2-deoxy-2-[$^{18}$F]fluoro-D-glucose ($^{18}$F-FDG) to determine the magnitude and distribution of lung perfusion and inflammation, respectively. CT scans were acquired at end-inspiration, end-expiration and mean lung volume to assess aeration, tidal hyper-aeration, and tidal recruitment.

In the second substudy, the perfusion of the left and right lungs of 7 animals was assessed. The distribution of pulmonary blood flow was marked by intravenous injection of fluorescence-labeled microspheres and radioactive $^{68}$Ga-labeled microspheres after 1 h of mechanical ventilation superposed with > 60 % or 0 % contribution of spontaneous breathing to minute ventilation. The distribution of $^{68}$Ga-labeled microspheres was detected by PET/CT scanning immediately after injection. The distribution of fluorescence-labeled microspheres was assessed *ex vivo*. The excised lungs were dried, cut in pieces, and the emitted fluorescence intensity and the tissue weight of each was measured. *In vivo* PET/CT measurements of the distribution of $^{68}$Ga-labeled microspheres were quantified as mass-normalized, relative radioactive intensities ($Q_{RM}$). The $Q_{RM}$-measurements were downscaled to the resolution of the fluorescence-labeled microspheres derived perfusion measurements ($Q_{RM,downscaled}$). *Ex vivo* measurements of the distribution of fluorescence-labeled microspheres were quantified as mass-normalized ($Q_{FM,Mass}$), volume-normalized ($Q_{FM,Volume}$), and mass- and volume-normalized, relative fluorescence intensities ($Q_{FM,Mass,Volume}$). The resolution and the outer dimensions of the lungs were compared between *ex vivo* and *in vivo* measurements. For each lung, the perfusion gradients along the ventro-dorsal and cranio-caudal axes were determined by linear least-squares regression of perfusion and spatial location. Slopes of regression lines were compared between measurements. For each lung, perfusion heterogeneity on a whole lung level and regional perfusion heterogeneity were compared between measurements.

**Results:** In the first substudy, PET/CT data showed that, despite comparable perfusion, volutrauma led to higher specific uptake of $^{18}$F-FDG in the ventilated, VILI lungs as compared to atelectrauma, mainly in central lung regions. Volutrauma yielded higher specific uptake of $^{18}$F-FDG in ventilated, VILI lungs compared to non-ventilated, control lungs, whereas atelectrauma did not. CT data revealed that atelectrauma yielded bigger non-aerated compartments and higher extent of tidal recruitment, while volutrauma resulted in bigger normally and hyper-aerated compartments and higher extent of tidal hyper-aeration. Driving pressure increased in atelectrauma, but not in volutrauma.

In the second substudy we found that *ex vivo* measurements of the distribution of fluorescence-labeled microspheres and *in vivo* measurements of the distribution of $^{68}$Ga-labeled microspheres revealed comparable results in respect to the presence and magnitudes of perfusion gradients along the ventro-dorsal and cranio-caudal gradients, despite a much lower resolution of the *ex vivo* measurements and the occurrence of lung deformation induced by lung extraction and drying. Both measurements showed higher perfusion of dorsal and caudal as compared to ventral and cranial regions, respectively. $Q_{RM}$-measurements showed higher heterogeneity on a whole lung level as compared to $Q_{RM,downscaled}$-measurements. As compared to $Q_{RM,downscaled}$-measurements, $Q_{FM,Volume}$- and $Q_{FM,Mass,Volume}$-measurements featured comparable higher regional heterogeneity, whereas $Q_{FM,Mass}$-measurements featured higher regional heterogeneity.

**Conclusion:** In the first substudy, PET/CT measurements showed that volutrauma promoted higher lung inflammation than atelectrauma, despite comparable tidal volume, driving pressure, and perfusion. This suggests that static stress and strain associated with volutrauma are the more important mechanisms of VILI as compared to the dynamic components.

The second substudy revealed that when applying volume normalization, *ex vivo* measurements of the distribution of fluorescence-labeled microspheres can be used interchangeably with *in vivo* measurements of the distribution of $^{68}$Ga-labeled microspheres for the determination of perfusion gradients, despite a much lower resolution of the *ex vivo* measurements and the occurrence of lung deformation induced by their extraction and drying. A reduction of the resolution of *in vivo* perfusion measurements and adjustment to that of the *ex vivo* measurements caused a reduction of the global and regional heterogeneity, respectively. Volume normalization of fluorescence-labeled microspheres derived perfusion measurements resulted in comparable global and regional perfusion heterogeneity of *ex vivo* and *in vivo* perfusion measurements at comparable resolution.

# Zusammenfassung

**Hintergrund:** Durch die Entwicklung neuer *in vivo* Bildgebungsmethoden, z.B. der Computertomographie (CT) und der Positronen-Emissions-Tomographie (PET), konnte in den letzten Jahren das Verständnis über die Pathophysiologie des akuten Lungenversagens *(acute respiratory distress syndrome, ARDS)* maßgeblich verbessert werden. So zeigten PET/CT-Messungen, dass beim ARDS pathophysiologische Veränderungen von Lungenbelüftung und -durchblutung zu einer Störung des Gasaustausches beitragen. Die deshalb erforderliche mechanische Beatmung kann allerdings zu einer weiteren Schädigung der Lunge führen *(ventilator induced lung injury, VILI)*. Bisher konnten weder die exakten pathophysiologischen Mechanismen des ARDS noch der potentiell schädigende Einfluss der mechanischen Beatmung vollständig geklärt werden.

**Fragestellung:** In dieser Doktorarbeit wurden PET/CT-Bildgebungstechniken für die Quantifizierung der pulmonalen Belüftung, neutrophilischen Inflammation und Perfusion im experimentellen Modell des ARDS verwendet. Hierfür wurden zwei Substudien durchgeführt.

Ziel der ersten Substudie war es, in einem tierexperimentellen Modell des ARDS den relativen Einfluss der beiden wesentlichen Mechanismen von VILI, das zyklische Öffnen und Schließen von Alveolen (Atelektrauma) und die alveoläre Überdehnung (Volutrauma), auf die pro-inflammatorische Antwort der Lunge zu untersuchen.

Die zweite Substudie hatte das Ziel, die Anwendung von Fluoreszenz-markierten Mikrosphären für Messungen der pulmonalen Perfusionsverteilung in akut geschädigten Lungen zu validieren. Es sollte geprüft werden, ob *ex vivo* Messungen mittels Fluoreszenz-markierten Mikrosphären alternativ zu *in vivo* PET/CT-Messungen mittels Gallium-68 ($^{68}$Ga)-markierten Mikrosphären im experimentellen Modell das ARDS herangezogen werden können.

**Material und Methoden:** Es wurden zwei Substudien in analgosedierten, intubierten und mechanisch beatmeten Schweinen durchgeführt. Die Induktion des ARDS erfolgte durch repetitives, bronchoalveoläres Lavagieren mit isotonischer Kochsalzlösung.

In der ersten Substudie erfolgten Untersuchungen an 10 Tieren. Nach Rekrutierung beider Lungen wurde eine absteigende Titration des positiven, end-exspiratorischen Drucks *(positive end-expiratory pressure, PEEP)* durchgeführt. Es folgte eine randomisierte Zuordnung der Versuchstiere zu einer vierstündigen Beatmungstherapie der linken, VILI Lunge zur Induktion eines Atelektraumas oder Volutraumas. In beiden Versuchsgruppen wurde ein vergleichbares Tidalvolumen von 3 ml/kg Körpergewicht appliziert. Zur Induktion von Volutrauma wurde ein hoher PEEP gewählt (2 $cmH_2O$ oberhalb des Levels, an dem sich die dynamische Compliance während der PEEP-Titration um mehr als 5 % erhöht). Zur Induktion von Atelektrauma wurde ein niedriger PEEP appliziert (PEEP, bei dem eine mit Volutrauma vergleichbare Atemwegsdruckdifferenz (Differenz aus Spitzendruck und PEEP) auftritt). In der rechten Lunge, welche als Kontrolllunge diente, wurde ein kontinuierlicher, positiver Atemwegsdruck von 20 $cmH_2O$ aufrechterhalten. Der Gasaustausch, insbesondere die Eliminierung von Kohlenstoffdioxid, wurde extrakorporal unterstützt. Nach vierstündiger Beatmung der linken, VILI Lunge erfolgte die Bildgebung. Für die Quantifizierung von Ausmaß und regionaler Verteilung der pulmonalen Inflammation wurde 2-deoxy-2-[$^{18}$F]fluoro-D-glucose ($^{18}$F-FDG) intravenös injiziert und die Aktivität mittels dynamischen PET/CT-Aufnahmen erfasst. Die Erfassung der Lungenperfusion erfolgte mittels intravenös injizierten, $^{68}$Ga-markierten Mikrosphären und statischen PET/CT-Aufnahmen. Anschließende CT-Aufnahmen während Atemmanövern am Ende der Inspiration, Exspiration und am mittleren Atemvolumen dienten der Bestimmung von Lungenbelüftung, zyklischer Überdehnung und Rekrutierung.

In der zweiten Substudie wurde in 7 Schweinen die Perfusion der linken und rechten Lunge untersucht (n = 14 Lungen). Nach jeweils einstündiger mechanischer Beatmung mittels zweiphasigem, positivem Beatmungsdruck überlagert mit einem Anteil an Spontanatmung am Minutenvolumen von 0 % oder > 60 % wurden Fluoreszenz-markierte und $^{68}$Ga-markierte Mikrosphären intravenös injiziert. Unmittelbar im Anschluss erfolgten PET/CT-Messungen der Verteilung der $^{68}$Ga-markierten Mikrosphären. Für die Analyse der Verteilung der Fluoreszenz-markierten Mikrosphären wurden die Lungen am Versuchsende entnommen, getrocknet, in Würfel gesägt und die emittierende Fluoreszenz sowie das Gewicht jedes Würfels gemessen. Die *in vivo* PET-Aktivitätsmessungen wurden auf die mittels CT bestimmte Lungenmasse normalisiert ($Q_{RM}$). Die $Q_{RM}$-Daten wurden auf die Auflösung der Fluoreszenzmessungen

heruntersklaiert ($Q_{RM,downscaled}$). Die Analyse der *ex vivo* Fluoreszenzmessungen erfolgte durch Normalisierung auf die Masse der Lungenwürfel ($Q_{FM,Mass}$), auf deren Volumen ($Q_{FM,Volume}$) und auf Würfelmasse und -volumen ($Q_{FM,Mass,Volume}$). Die Auflösung und die äußeren Konturen der Lungen wurden zwischen *ex vivo* und *in vivo* Messungen verglichen. Lineare Regressionen von Perfusion und axialer Verteilung jedes Lungenvolumenelementes dienten der Bestimmung von Perfusionsgradienten entlang der ventro-dorsalen und kranio-kaudalen Achse. Die Anstiege der Regressionsgeraden wurden zwischen den Messmethoden verglichen. Für jede Lunge wurde die globale und regionale Perfusionsheterogenität bestimmt und zwischen den Messmethoden verglichen.

**Ergebnisse:** In der ersten Substudie verdeutlichten PET/CT-Messungen, dass, trotz vergleichbarer Perfusion, Volutrauma im Vergleich zu Atelektrauma zu einer höheren spezifischen Aufnahme von $^{18}$F-FDG in den beatmeten, VILI Lungen führte. Dieser Effekt trat hauptsächlich in zentralen Lungenregionen auf. Weiterhin führte Volutrauma, aber nicht Atelektrauma, zu einer höheren spezifischen $^{18}$F-FDG-Aufnahme in den beatmeten, VILI Lungen im Vergleich zu den nicht-ventilierten Kontrolllungen. CT-Aufnahmen verdeutlichten, dass Atelektrauma einen höheren Anteil an nicht belüfteten Lungenkompartimenten und mehr zyklische Rekrutierung zur Folge hatte. Volutrauma bedingte hingegen höhere Anteile an überblähten und normal belüfteten Lungenarealen und mehr zyklische Überdehnung. Die Atemwegsdruckdifferenzen waren anfänglich zwischen den Gruppen vergleichbar, stiegen im Verlauf bei Atelektrauma, aber nicht bei Volutrauma, an.

In der zweiten Substudie verdeutlichten sowohl *ex vivo* $Q_{FM,Volume}$-Messungen, als auch *in vivo* $Q_{RM}$-Messungen die Existenz von Perfusionsgradienten entlang der ventro-dorsalen und kranio-kaudalen Achsen, trotzdem $Q_{FM}$-Messungen eine 21-fach geringere Auflösung aufwiesen und die erforderliche Lungenentnahme und -trocknung eine Lungendeformation bedingte. Beide Messverfahren zeigten stärkere Perfusionen dorsaler und kaudaler im Vergleich zu ventraler und kranialer Lungenareale. Im Vergleich zu $Q_{RM,downscaled}$-Messungen wiesen $Q_{RM}$-Messungen höhere globale Perfusionsheterogenitäten auf. Verglichen mit $Q_{RM,downscaled}$-Messungen wiesen sowohl $Q_{FM,Volume}$-Messungen, als auch $Q_{FM,Mass,Volume}$-Messungen vergleichbare regionale Perfusionsheterogenitäten auf.

**Schlussfolgerungen:** In der ersten Substudie führte Volutrauma im Vergleich zu Atelektrauma, trotz vergleichbarem Tidalvolumen, geringerer Atemwegsdruckdifferenz und vergleichbarer Perfusion, zu einer höheren pulmonalen Inflammation. Dies deutet darauf hin, dass in diesem Modell des ARDS die mit Volutrauma assoziierten hohen statischen Drücke im Vergleich zu dynamischen Einflüssen die schädlicheren Mechanismen von VILI sind.

Die zweite Substudie verdeutlichte, dass *ex vivo* Messungen der Verteilung von Fluoreszenz-markierten Mikrosphären bei Volumennormalisierung, trotz geringerer Auflösung und auftretenden Lungendeformationen, vergleichbare Messergebnisse hinsichtlich der Existenz und des Ausmaßes von Lungengradienten mit *in vivo* PET/CT-Messungen aufzeigen. Eine Anpassung der Auflösung der *in vivo* Perfusionsmessungen an die der *ex vivo* Messungen verringerte sowohl die globale, als auch die regionale Perfusionsheterogenität. Bei gleicher Auflösung zeigten *ex vivo* $Q_{FM,Volume}$-Messungen vergleichbare globale und regionale Perfusionsheterogenitäten wie *in vivo* Messungen. Die Studienergebnisse deuten darauf hin, dass für die Quantifizierung von pulmonalen Perfusionsgradienten *ex vivo* $Q_{FM,Volume}$-Messungen alternativ zu *in vivo* PET/CT-Messungen durchgeführt werden können.

# References

ABX advanced, biochemical compounds GmbH. 2015.

Amato MB, Barbas CS, Medeiros DM, Magaldi RB, Schettino GP, Lorenzi-Filho G, Kairalla RA, Deheinzelin D, Munoz C, Oliveira R, Takagaki TY, Carvalho CR. 1998. Effect of a protective-ventilation strategy on mortality in the acute respiratory distress syndrome. N Engl J Med 338:347–354.

Ashbaugh DG, Bigelow DB, Petty TL, Levine BE. 1967. Acute respiratory distress in adults. Lancet Lond Engl 2:319–323.

Avanzolini G, Barbini P, Cappello A, Cevenini G, Chiari L. 1997. A new approach for tracking respiratory mechanical parameters in real-time. Ann Biomed Eng 25:154–163.

Beck KC. 1987a. Regional trapping of microspheres in the lung compares well with regional blood flow. J Appl Physiol 63:883–889.

Beck KC. 1987b. Regional trapping of microspheres in the lung compares well with regional blood flow. J Appl Physiol 63:883–889.

Beck KC. 1990. Influence of vascular distending pressure on regional flows in isolated perfused dog lungs. J Appl Physiol Bethesda Md 1985 69:1869–1874.

Bellani G, Amigoni M, Pesenti A. 2011. Positron emission tomography in ARDS: a new look at an old syndrome. Minerva Anestesiol 77:439–447.

Bellani G, Messa C, Guerra L, Spagnolli E, Foti G, Patroniti N, Fumagalli R, Musch G, Fazio F, Pesenti A. 2009. Lungs of patients with acute respiratory distress syndrome show diffuse inflammation in normally aerated regions: a [18F]-fluoro-2-deoxy-D-glucose PET/CT study. Crit Care Med 37:2216–2222.

Bellani G, Rouby J-J, Constantin J-M, Pesenti A. 2017. Looking closer at acute respiratory distress syndrome: the role of advanced imaging techniques. Curr Opin Crit Care 23:30–37.

Bellani G, Laffey JG, Pham T, et al. 2016. EPidemiology, patterns of care, and mortality for patients with acute respiratory distress syndrome in intensive care units in 50 countries. JAMA 315:788–800.

Bernard GR, Artigas A, Brigham KL, Carlet J, Falke K, Hudson L, Lamy M, Legall JR, Morris A, Spragg R. 1994a. The American-European Consensus Conference on ARDS. Definitions, mechanisms, relevant outcomes, and clinical trial coordination. Am J Respir Crit Care Med 149:818–824.

Bernard GR, Artigas A, Brigham KL, Carlet J, Falke K, Hudson L, Lamy M, LeGall JR, Morris A, Spragg R. 1994b. Report of the American-European Consensus conference on acute respiratory distress syndrome: definitions, mechanisms, relevant outcomes, and clinical trial coordination. Consensus Committee. J Crit Care 9:72–81.

Bilek AM, Dee KC, Gaver DP. 2003. Mechanisms of surface-tension-induced epithelial cell damage in a model of pulmonary airway reopening. J Appl Physiol Bethesda Md 1985 94:770–783.

Boedeker KL, McNitt-Gray MF, Rogers SR, Truong DA, Brown MS, Gjertson DW, Goldin JG. 2004. Emphysema: effect of reconstruction algorithm on CT imaging measures. Radiology 232:295–301.

Borges JB, Costa ELV, Bergquist M, Lucchetta L, Widström C, Maripuu E, Suarez-Sipmann F, Larsson A, Amato MBP, Hedenstierna G. 2015. Lung inflammation persists after 27 hours of protective Acute Respiratory Distress Syndrome Network Strategy and is concentrated in the nondependent lung. Crit Care Med 43:e123-132.

Carvalho AR, Spieth PM, Güldner A, Cuevas M, Carvalho NC, Beda A, Spieth S, Stroczynski C, Wiedemann B, Koch T, Pelosi P, Abreu MG de. 2011. Distribution of regional lung aeration and perfusion during conventional and noisy pressure support ventilation in experimental lung injury. J Appl Physiol Bethesda Md 1985 110:1083–1092.

Castillo RL, Carrasco Loza R, Romero-Dapueto C. 2015. Pathophysiological Approaches of Acute Respiratory Distress syndrome: Novel Bases for Study of Lung Injury. Open Respir Med J 9:83–91.

Chen DL, Mintun MA, Schuster DP. 2004a. Comparison of methods to quantitate 18F-FDG uptake with PET during experimental acute lung injury. J Nucl Med Off Publ Soc Nucl Med 45:1583–1590.

Chen DL, Mintun MA, Schuster DP. 2004b. Comparison of methods to quantitate 18F-FDG uptake with PET during experimental acute lung injury. J Nucl Med Off Publ Soc Nucl Med 45:1583–1590.

Chen DL, Schuster DP. 2004. Positron emission tomography with [18F]fluorodeoxyglucose to evaluate neutrophil kinetics during acute lung injury. Am J Physiol Lung Cell Mol Physiol 286:L834-840.

Cochrane CG, Revak SD. 1999. Surfactant lavage treatment in a model of respiratory distress syndrome. Chest 116:85S–86S.

Costa ELV, Musch G, Winkler T, Schroeder T, Harris RS, Jones HA, Venegas JG, Vidal Melo MF. 2010. Mild endotoxemia during mechanical ventilation produces spatially heterogeneous pulmonary neutrophilic inflammation in sheep. Anesthesiology 112:658–669.

Curley G, Laffey JG, Kavanagh BP. 2010. Bench-to-bedside review: carbon dioxide. Crit Care Lond Engl 14:220.

Dittrich AS, Winkler T, Wellman T, Prost N de, Musch G, Harris RS, Vidal Melo MF. 2012. Modeling 18F-FDG Kinetics during Acute Lung Injury: Experimental Data and Estimation Errors. PLoS ONE 7:e47588.

Ferguson ND, Cook DJ, Guyatt GH, Mehta S, Hand L, Austin P, Zhou Q, Matte A, Walter SD, Lamontagne F, Granton JT, Arabi YM, et al. 2013. High-frequency oscillation in early acute respiratory distress syndrome. N Engl J Med 368:795–805.

Ferguson ND, Fan E, Camporota L, Antonelli M, Anzueto A, Beale R, Brochard L, Brower R, Esteban A, Gattinoni L, Rhodes A, Slutsky AS, et al. 2012. The Berlin definition of ARDS: an expanded rationale, justification, and supplementary material. Intensive Care Med 38:1573–1582.

Gallagher BM, Fowler JS, Gutterson NI, MacGregor RR, Wan CN, Wolf AP. 1978. Metabolic trapping as a principle of oradiopharmaceutical design: some factors resposible for the biodistribution of [18F] 2-deoxy-2-fluoro-D-glucose. J Nucl Med Off Publ Soc Nucl Med 19:1154–1161.

Gattinoni L, Caironi P, Pelosi P, Goodman LR. 2001. What has computed tomography taught us about the acute respiratory distress syndrome? Am J Respir Crit Care Med 164:1701–1711.

Gattinoni L, Carlesso E, Cadringher P, Valenza F, Vagginelli F, Chiumello D. 2003. Physical and biological triggers of ventilator-induced lung injury and its prevention. Eur Respir J Suppl 47:15s–25s.

Gattinoni L, Mascheroni D, Torresin A, Marcolin R, Fumagalli R, Vesconi S, Rossi GP, Rossi F, Baglioni S, Bassi F. 1986a. Morphological response to positive end expiratory pressure in acute respiratory failure. Computerized tomography study. Intensive Care Med 12:137–142.

Gattinoni L, Mascheroni D, Torresin A, Marcolin R, Fumagalli R, Vesconi S, Rossi GP, Rossi F, Baglioni S, Bassi F, Nastri G, Pesenti A. 1986b. Morphological response to positive end expiratory pressure in acute respiratory failure. Computerized tomography study. Intensive Care Med 12:137–142.

Gattinoni L, Pesenti A. 2005. The concept of “baby lung.” Intensive Care Med 31:776–784.

Gattinoni L, Presenti A, Torresin A, Baglioni S, Rivolta M, Rossi F, Scarani F, Marcolin R, Cappelletti G. 1986c. Adult respiratory distress syndrome profiles by computed tomography. J Thorac Imaging 1:25–30.

Gattinoni L, Presenti A, Torresin A, Baglioni S, Rivolta M, Rossi F, Scarani F, Marcolin R, Cappelletti G. 1986d. Adult respiratory distress syndrome profiles by computed tomography. J Thorac Imaging 1:25–30.

Gattinoni L, Quintel M. 2016. Is mechanical ventilation a cure for ARDS? Intensive Care Med 42:916–917.

Gattinoni L, Tonetti T, Cressoni M, Cadringher P, Herrmann P, Moerer O, Protti A, Gotti M, Chiurazzi C, Carlesso E, Chiumello D, Quintel M. 2016. Ventilator-related causes of lung injury: the mechanical power. Intensive Care Med 42:1567–1575.

Glenny RW, Bernard S, Brinkley M. 1993. Validation of fluorescent-labeled microspheres for measurement of regional organ perfusion. J Appl Physiol Bethesda Md 1985 74:2585–2597.

Glenny RW, Bernard SL, Lamm WJ. 2000a. Hemodynamic effects of 15-microm-diameter microspheres on the rat pulmonary circulation. J Appl Physiol Bethesda Md 1985 89:499–504.

Glenny RW, Bernard SL, Luchtel DL, Neradilek B, Polissar NL. 2007. The spatial-temporal redistribution of pulmonary blood flow with postnatal growth. J Appl Physiol Bethesda Md 1985 102:1281–1288.

Glenny RW, Bernard SL, Robertson HT. 2000b. Pulmonary blood flow remains fractal down to the level of gas exchange. J Appl Physiol Bethesda Md 1985 89:742–748.

Glenny RW, McKinney S, Robertson HT. 1997. Spatial pattern of pulmonary blood flow distribution is stable over days. J Appl Physiol Bethesda Md 1985 82:902–907.

Glenny RW, Polissar L, Robertson HT. 1991. Relative contribution of gravity to pulmonary perfusion heterogeneity. J Appl Physiol Bethesda Md 1985 71:2449–2452.

Guérin C, Reignier J, Richard J-C, Beuret P, Gacouin A, Boulain T, Mercier E, Badet M, Mercat A, Baudin O, Clavel M, Chatellier D, et al. 2013. Prone positioning in severe acute respiratory distress syndrome. N Engl J Med 368:2159–2168.

Güldner A, Braune A, Ball L, Silva PL, Samary C, Insorsi A, Huhle R, Rentzsch I, Becker C, Oehme L, Andreeff M, Vidal Melo MF, et al. 2016. Comparative Effects of Volutrauma and Atelectrauma on Lung Inflammation in Experimental Acute Respiratory Distress Syndrome. Crit Care Med 44:e854-865.

Güldner A, Braune A, Carvalho N, Beda A, Zeidler S, Wiedemann B, Wunderlich G, Andreeff M, Uhlig C, Spieth PM, Koch T, Pelosi P, et al. 2014. Higher levels of spontaneous breathing induce lung recruitment and reduce global stress/strain in experimental lung injury. Anesthesiology 120:673–682.

Hoekstra CJ, Hoekstra OS, Stroobants SG, Vansteenkiste J, Nuyts J, Smit EF, Boers M, Twisk JWR, Lammertsma AA. 2002. Methods to Monitor Response to Chemotherapy in Non-Small Cell Lung Cancer with 18F-FDG PET. J Nucl Med 43:1304–1309.

Hoekstra CJ, Paglianiti I, Hoekstra OS, Smit EF, Postmus PE, Teule GJJ, Lammertsma AA. 2000. Monitoring response to therapy in cancer using [18F]-2-fluoro-2-deoxy-d-glucose and positron emission tomography: an overview of different analytical methods. Eur J Nucl Med 27:731–743.

Hoff J van den, Oehme L, Schramm G, Maus J, Lougovski A, Petr J, Beuthien-Baumann B, Hofheinz F. 2013. The PET-derived tumor-to-blood standard uptake ratio (SUR) is superior to tumor SUV as a surrogate parameter of the metabolic rate of FDG. EJNMMI Res 3:77.

Hofheinz F, Pötzsch C, Oehme L, Beuthien-Baumann B, Steinbach J, Kotzerke J, Hoff J van den. 2012. Automatic volume delineation in oncological PET. Evaluation of a dedicated software tool and comparison with manual delineation in clinical data sets. Nukl Nucl Med 51:9–16.

Hogg JC. 1987. Neutrophil kinetics and lung injury. Physiol Rev 67:1249–1295.

Hotchkiss JR, Blanch L, Murias G, Adams AB, Olson DA, Wangensteen OD, Leo PH, Marini JJ. 2000. Effects of decreased respiratory frequency on ventilator-induced lung injury. Am J Respir Crit Care Med 161:463–468.

Hounsfield GN. 1980. Computed medical imaging. Science 210:22–28.

Hübler M, Souders JE, Shade ED, Hlastala MP, Polissar NL, Glenny RW. 1999. Validation of fluorescent-labeled microspheres for measurement of relative blood flow in severely injured lungs. J Appl Physiol Bethesda Md 1985 87:2381–2385.

Hübler M, Souders JE, Shade ED, Polissar NL, Schimmel C, Hlastala MP. 2001. Effects of vaporized perfluorocarbon on pulmonary blood flow and ventilation/perfusion distribution in a model of acute respiratory distress syndrome. Anesthesiology 95:1414–1421.

Hudson LD, Milberg JA, Anardi D, Maunder RJ. 1995. Clinical risks for development of the acute respiratory distress syndrome. Am J Respir Crit Care Med 151:293–301.

Imanaka H, Shimaoka M, Matsuura N, Nishimura M, Ohta N, Kiyono H. 2001. Ventilator-induced lung injury is associated with neutrophil infiltration, macrophage activation, and TGF-beta 1 mRNA upregulation in rat lungs. Anesth Analg 92:428–436.

Jacene HA, Cohade C, Wahl RL. 2004. F-18 FDG PET/CT in acute respiratory distress syndrome: a case report. Clin Nucl Med 29:786–788.

Jones HA. 2005. Inflammation imaging. Proc Am Thorac Soc 2:545–548, 513–514.

Jones HA, Cadwallader KA, White JF, Uddin M, Peters AM, Chilvers ER. 2002. Dissociation Between Respiratory Burst Activity and Deoxyglucose Uptake in Human Neutrophil Granulocytes: Implications for Interpretation of 18F-FDG PET Images. J Nucl Med 43:652–657.

Kotzerke J, Andreeff M, Wunderlich G, Wiggermann P, Zöphel K. 2010. [Ventilation-perfusion-lungscintigraphy using PET and 68Ga-labeled radiopharmaceuticals]. Nukl Nucl Med 49:203–208.

Lachmann B, Robertson B, Vogel J. 1980. In vivo lung lavage as an experimental model of the respiratory distress syndrome. Acta Anaesthesiol Scand 24:231–236.

Lanteri CJ, Kano S, Sly PD. 1994. Validation of esophageal pressure occlusion test after paralysis. Pediatr Pulmonol 17:56–62.

Levi C, Gray J, McCullough E, Hattery R. 2012. The unreliability of CT numbers as absolute values. Am J Roentgenol 139:443–447.

Leys C, Ley C, Klein O, Bernard P, Licata L. 2013. Detecting outliers: Do not use standard deviation around the mean, use absolute deviation around the median. J Exp Soc Psychol 49:764–766.

Malbouisson LM, Muller J-C, Constantin J-M, Lu Q, Puybasset L, Rouby J-J. 2001. Computed Tomography Assessment of Positive End-expiratory Pressure-induced Alveolar Recruitment in Patients with Acute Respiratory Distress Syndrome. Am J Respir Crit Care Med 163:1444–1450.

Matthay MA, Zemans RL. 2011. The acute respiratory distress syndrome: pathogenesis and treatment. Annu Rev Pathol 6:147–163.

Matute-Bello G, Downey G, Moore BB, Groshong SD, Matthay MA, Slutsky AS, Kuebler WM, Acute Lung Injury in Animals Study Group. 2011. An official American Thoracic Society workshop report: features and measurements of experimental acute lung injury in animals. Am J Respir Cell Mol Biol 44:725–738.

Matute-Bello G, Frevert CW, Martin TR. 2008a. Animal models of acute lung injury. Am J Physiol - Lung Cell Mol Physiol 295:L379–L399.

Matute-Bello G, Frevert CW, Martin TR. 2008b. Animal models of acute lung injury. Am J Physiol Lung Cell Mol Physiol 295:L379-399.

Maunder RJ, Shuman WP, McHugh JW, Marglin SI, Butler J. 1986. Preservation of normal lung regions in the adult respiratory distress syndrome: Analysis by computed tomography. JAMA 255:2463–2465.

Mazzei MA, Guerrini S, Cioffi Squitieri N, Franchi F, Volterrani L, Genovese EA, Macarini L. 2012. [Role of computed tomography in the diagnosis of acute lung injury/acute respiratory distress syndrome]. Recenti Prog Med 103:459–464.

Mead J, Takishima T, Leith D. 1970. Stress distribution in lungs: a model of pulmonary elasticity. J Appl Physiol 28:596–608.

Melo MFV, Winkler T, Harris RS, Musch G, Greene RE, Venegas JG. 2010. Spatial Heterogeneity of Lung Perfusion Assessed with 13N PET as a Vascular Biomarker in Chronic Obstructive Pulmonary Disease. J Nucl Med 51:57–65.

Muscedere JG, Mullen JB, Gan K, Slutsky AS. 1994. Tidal ventilation at low airway pressures can augment lung injury. Am J Respir Crit Care Med 149:1327–1334.

Musch G. 2011. Positron emission tomography: a tool for better understanding of ventilator-induced and acute lung injury. Curr Opin Crit Care 17:7–12.

Musch G, Layfield JDH, Harris RS, Melo MFV, Winkler T, Callahan RJ, Fischman AJ, Venegas JG. 2002. Topographical distribution of pulmonary perfusion and ventilation, assessed by PET in supine and prone humans. J Appl Physiol 93:1841–1851.

Musch G, Venegas JG, Bellani G, Winkler T, Schroeder T, Petersen B, Harris RS, Melo MFV. 2007. Regional gas exchange and cellular metabolic activity in ventilator-induced lung injury. Anesthesiology 106:723–735.

Nash G, Blennerhassett JB, Pontoppidan H. 1967. Pulmonary Lesions Associated with Oxygen Therapy and Artificial Ventilation. N Engl J Med 276:368–374.

Obi T, Matej S, Lewitt RM, Herman GT. 2000. 2.5-D simultaneous multislice reconstruction by series expansion methods from Fourier-rebinned PET data. IEEE Trans Med Imaging 19:474–484.

Oehme L, Zöphel K, Golgor E, Andreeff M, Wunderlich G, Brogsitter C, Abreu MG de, Kotzerke J. 2014. Quantitative analysis of regional lung ventilation and perfusion PET with 68Ga-labelled tracers: Nucl Med Commun 35:501–510.

Otto CM, Markstaller K, Kajikawa O, Karmrodt J, Syring RS, Pfeiffer B, Good VP, Frevert CW, Baumgardner JE. 2008. Spatial and temporal heterogeneity of ventilator-associated lung injury after surfactant depletion. J Appl Physiol Bethesda Md 1985 104:1485–1494.

Patlak CS, Blasberg RG, Fenstermacher JD. 1983. Graphical evaluation of blood-to-brain transfer constants from multiple-time uptake data. J Cereb Blood Flow Metab Off J Int Soc Cereb Blood Flow Metab 3:1–7.

Pepe PE, Potkin RT, Reus DH, Hudson LD, Carrico CJ. 1982. Clinical predictors of the adult respiratory distress syndrome. Am J Surg 144:124–130.

Pesenti A, Musch G, Lichtenstein D, Mojoli F, Amato MBP, Cinnella G, Gattinoni L, Quintel M. 2016. Imaging in acute respiratory distress syndrome. Intensive Care Med 42:686–698.

Phelps ME. 2000. Positron emission tomography provides molecular imaging of biological processes. Proc Natl Acad Sci U S A 97:9226–9233.

Prost N de, Costa EL, Wellman T, Musch G, Winkler T, Tucci MR, Harris RS, Venegas JG, Vidal Melo MF. 2011. Effects of surfactant depletion on regional pulmonary metabolic activity during mechanical ventilation. J Appl Physiol Bethesda Md 1985 111:1249–1258.

Prost N de, Tucci MR, Melo MFV. 2010. Assessment of lung inflammation with 18F-FDG PET during acute lung injury. AJR Am J Roentgenol 195:292–300.

Puybasset L, Cluzel P, Gusman P, Grenier P, Preteux F, Rouby JJ. 2000. Regional distribution of gas and tissue in acute respiratory distress syndrome. I. Consequences for lung morphology. CT Scan ARDS Study Group. Intensive Care Med 26:857–869.

Reivich M, Kuhl D, Wolf A, Greenberg J, Phelps M, Ido T, Casella V, Fowler J, Hoffman E, Alavi A, Som P, Sokoloff L. 1979. The [18F]fluorodeoxyglucose method for the measurement of local cerebral glucose utilization in man. Circ Res 44:127–137.

Reske AW, Busse H, Amato MBP, Jaekel M, Kahn T, Schwarzkopf P, Schreiter D, Gottschaldt U, Seiwerts M. 2008. Image reconstruction affects computer tomographic assessment of lung hyperinflation. Intensive Care Med 34:2044–2053.

Richard J-C, Janier M, Decailliot F, Bars DL, Lavenne F, Berthier V, Lionnet M, Cinotti L, Annat G, Guérin C. 2002. Comparison of PET with Radioactive Microspheres to Assess Pulmonary Blood Flow. J Nucl Med 43:1063–1071.

Richter T, Bellani G, Scott Harris R, Vidal Melo MF, Winkler T, Venegas JG, Musch G. 2005. Effect of prone position on regional shunt, aeration, and perfusion in experimental acute lung injury. Am J Respir Crit Care Med 172:480–487.

Richter T, Bergmann R, Musch G, Pietzsch J, Koch T. 2015. Reduced pulmonary blood flow in regions of injury 2 hours after acid aspiration in rats. BMC Anesthesiol 15:36.

Richter T, Bergmann R, Pietzsch J, Közle I, Hofheinz F, Schiller E, Ragaller M, Hoff J van den. 2010. Effects of posture on regional pulmonary blood flow in rats as measured by PET. J Appl Physiol Bethesda Md 1985 108:422–429.

Robertson HT, Hlastala MP. 2007. Microsphere maps of regional blood flow and regional ventilation. J Appl Physiol Bethesda Md 1985 102:1265–1272.

Rodrigues RS, Miller PR, Bozza FA, Marchiori E, Zimmerman GA, Hoffman JM, Morton KA. 2008. FDG-PET in patients at risk for acute respiratory distress syndrome: a preliminary report. Intensive Care Med 34:2273–2278.

Rommelsheim K, Lackner K, Westhofen P, Distelmaier W, Hirt S. 1983. Das respiratorische Distress-Syndrom des Erwachsenen (ARDS) im Computertomogramm. AINS - Anästhesiol · Intensivmed · Notfallmedizin · Schmerzther 18:59–64.

Rosenthal C, Caronia C, Quinn C, Lugo N, Sagy M. 1998a. A comparison among animal models of acute lung injury. Crit Care Med 26:912–916.

Rosenthal C, Caronia C, Quinn C, Lugo N, Sagy M. 1998b. A comparison among animal models of acute lung injury. Crit Care Med 26:912–916.

ROTOP Pharmaka GmbH. 2016. Produktinformation ROTOP - HSA Mikrosphären. ROTOP Pharmaka GmbH Dresd Produktblatt GFI-B20-DE-deu-04:

Rudroff T, Kindred JH, Kalliokoski KK. 2015. [18F]-FDG positron emission tomography--an established clinical tool opening a new window into exercise physiology. J Appl Physiol Bethesda Md 1985 118:1181–1190.

Saha D, Takahashi K, Prost N de, Winkler T, Pinilla-Vera M, Baron RM, Vidal Melo MF. 2013. Micro-autoradiographic assessment of cell types contributing to 2-deoxy-2-[(18)F]fluoro-D-glucose uptake during ventilator-induced and endotoxemic lung injury. Mol Imaging Biol MIB Off Publ Acad Mol Imaging 15:19–27.

Schroeder T, Melo MFV, Venegas JG. 2011. Analysis of 2-[Fluorine-18]-Fluoro-2-deoxy-D-glucose uptake kinetics in PET studies of pulmonary inflammation. Acad Radiol 18:418–423.

Schroeder T, Vidal Melo MF, Musch G, Harris RS, Venegas JG, Winkler T. 2007. Image-derived input function for assessment of 18F-FDG uptake by the inflamed lung. J Nucl Med Off Publ Soc Nucl Med 48:1889–1896.

Schroeder T, Vidal Melo MF, Musch G, Harris RS, Venegas JG, Winkler T. 2008. Modeling pulmonary kinetics of 2-deoxy-2-[18F]fluoro-D-glucose during acute lung injury. Acad Radiol 15:763–775.

Sheard S, Rao P, Devaraj A. 2012. Imaging of Acute Respiratory Distress Syndrome. Respir Care 57:607–612.

Sokoloff L, Reivich M, Kennedy C, Des Rosiers MH, Patlak CS, Pettigrew KD, Sakurada O, Shinohara M. 1977. The [14C]deoxyglucose method for the measurement of local cerebral glucose utilization: theory, procedure, and normal values in the conscious and anesthetized albino rat. J Neurochem 28:897–916.

Terragni PP, Rosboch G, Tealdi A, Corno E, Menaldo E, Davini O, Gandini G, Herrmann P, Mascia L, Quintel M, Slutsky AS, Gattinoni L, et al. 2007. Tidal hyperinflation during low tidal volume ventilation in acute respiratory distress syndrome. Am J Respir Crit Care Med 175:160–166.

Tremblay L, Valenza F, Ribeiro SP, Li J, Slutsky AS. 1997. Injurious ventilatory strategies increase cytokines and c-fos m-RNA expression in an isolated rat lung model. J Clin Invest 99:944–952.

Tsuchida S, Engelberts D, Peltekova V, Hopkins N, Frndova H, Babyn P, McKerlie C, Post M, McLoughlin P, Kavanagh BP. 2006. Atelectasis causes alveolar injury in nonatelectatic lung regions. Am J Respir Crit Care Med 174:279–289.

Van Oosterhout MF, Prinzen FW, Sakurada S, Glenny RW, Hales JR. 1998. Fluorescent microspheres are superior to radioactive microspheres in chronic blood flow measurements. Am J Physiol 275:H110-115.

Venegas JG, Galletti GG. 2000. Low-pass filtering, a new method of fractal analysis: application to PET images of pulmonary blood flow. J Appl Physiol Bethesda Md 1985 88:1365–1373.

Venegas JG, Treppo S, Mijailovich S. 1994. Contributions of statistical noise to spatial heterogeneity of PET images of pulmonary function.

Wagner SJ, Welch MJ. 1979. Gallium-68 labeling of albumin and albumin microspheres. J Nucl Med Off Publ Soc Nucl Med 20:428–433.

Ware LB. 2006. Pathophysiology of acute lung injury and the acute respiratory distress syndrome. Semin Respir Crit Care Med 27:337–349.

Ware LB, Matthay MA. 2000. The Acute Respiratory Distress Syndrome. N Engl J Med 342:1334–1349.

Webb HH, Tierney DF. 1974. Experimental Pulmonary Edema due to Intermittent Positive Pressure Ventilation with High Inflation Pressures. Protection by Positive End-Expiratory Pressure. Am Rev Respir Dis 110:556–565.

Wellman TJ, Winkler T, Costa ELV, Musch G, Harris RS, Zheng H, Venegas JG, Vidal Melo MF. 2014. Effect of local tidal lung strain on inflammation in normal and lipopolysaccharide-exposed sheep*. Crit Care Med 42:e491-500.

West JB. 1978. Regional differences in the lung. Chest 74:426–437.

Wheeler AP, Bernard GR. 2007. Acute lung injury and the acute respiratory distress syndrome: a clinical review. The Lancet 369:1553–1564.

Willmott N, Chen Y, Goldberg J, Mcardle C, Florence AT. 1989. Biodegradation rate of embolized protein microspheres in lung, liver and kidney of rats. J Pharm Pharmacol 41:433–438.

Winkler T, Melo MFV, Degani-Costa LH, Harris RS, Correia JA, Musch G, Venegas JG. 2015. Estimation of noise-free variance to measure heterogeneity. PloS One 10:e0123417.

Wunderlich G, Schiller E, Bergmann R, Pietzsch H-J. 2010. Comparison of the stability of Y-90-, Lu-177- and Ga-68- labeled human serum albumin microspheres (DOTA-HSAM). Nucl Med Biol 37:861–867.

Xu, Moonen, Johansson, Bake. 2000. Distribution of ventilation-to-perfusion ratios analysed in planar scintigrams of emphysematous patients. Clin Physiol 20:89–94.

Young D, Lamb SE, Shah S, MacKenzie I, Tunnicliffe W, Lall R, Rowan K, Cuthbertson BH, OSCAR Study Group. 2013. High-frequency oscillation for acute respiratory distress syndrome. N Engl J Med 368:806–813.

Yushkevich PA, Piven J, Hazlett HC, Smith RG, Ho S, Gee JC, Gerig G. 2006. User-guided 3D active contour segmentation of anatomical structures: Significantly improved efficiency and reliability. NeuroImage 31:1116–1128.

Zhou X, Loran DB, Wang D, Hyde BR, Lick SD, Zwischenberger JB. 2005. Seventy-two hour gas exchange performance and hemodynamic properties of NOVALUNG iLA as a gas exchanger for arteriovenous carbon dioxide removal. Perfusion 20:303–308.

# List of Images

# List of Tables

# A Appendix

## A.1 Additional Results: Volutrauma and Atelectrauma in ARDS

**Appendix A.1.1:**

***Table A.5.1:*** *Bodyweight, number of lavages and fluids.*

| | **Volutrauma** | **Atelectrauma** |
|---|---|---|
| **Body weight [kg]** | 41.2 [37.7 – 46.8] | 38.2 [36.3 - 43.3] |
| **Number of lavages** | 10 [8 – 12] | 11 [10 – 12] |
| **Cumulative Cristalloid [mL/kg PBW]** | 137 [106 – 151] | 131 [110 – 142] |
| **Cumulative Colloid [mL/kg PBW]** | 25 [7 – 32] | 14 [0 – 24] |

***Table A.5.2:*** *Mean and standard deviation of respiratory mechanics variables.*

| Variable | Group | Baseline 1 | Injury | Time 1 | Time 2 | Time 3 | Time 4 | *group effect* | *time*group effects* |
|---|---|---|---|---|---|---|---|---|---|
| **MV [L/min]** | Volutrauma | 5.4±0.8 | 5.3±0.8 | 3.9±0.4 | 3.9±0.5 | 4.1±0.6 | 4.1±0.6 | *p = 0.203* | *p = 0.608* |
| | Atelectrauma | 4.7±0.4 | 4.7±0.4 | 3.3±0.8 | 3.2±0.8 | 3.2±0.7 | 3.1±0.8 | | |
| | | *p = 0.167* | *p = 0.177* | | | | | | |
| **$V_T$ [mL/kg PBW]** | Volutrauma | 8.1±0.3 | 8.0±0.2 | 3.2±0.4 | 3.2±0.4 | 3.2±0.3 | 3.2±0.3 | *p = 0.335* | *p = 0.770* |
| | Atelectrauma | 8.3±0.2 | 8.2±0.1 | 3.2±0.1 | 3.3±0.1 | 3.2±0.1 | 3.3±0.1 | | |
| | | *p = 0.115* | *p = 0.138* | | | | | | |
| **RR [breaths per minute]** | Volutrauma | 16.2±1.6 | 16.2±1.6 | 28.6±2.2 | 29.0±2.6 | 30.0±1.4 | 30.0±1.4 | *p = 0.401* | *p = 0.156* |
| | Atelectrauma | 15.0±0.0 | 15.0±0.0 | 28.6±1.9 | 26.8±3.0 | 26.4±4.3 | 26.0±4.2 | | |
| | | *p = 0.141* | *p = 0.178* | | | | | | |
| **$P_{aw,peak}$ [$cmH_2O$]** | Volutrauma | 20.5±1.3 | 27.1±2.9 | 54.6±4.1 | 54.0±4.0 | 52.9±3.5 | 52.2±3.5 | *p < 0.001* | *p = 0.001* |
| | Atelectrauma | 21.3±2.0 | 29.0±4.3 | 32.2±7.3 | 33.7±7.1 | 34.4±6.1 | 34.9±6.1 | | |
| | | *p = 0.445* | *p = 0.448* | | | | | | |
| **$P_{aw,mean}$ [$cmH_2O$]** | Volutrauma | 12.3±0.5 | 15.0±1.0 | 42.9±2.5 | 42.6±2.6 | 41.9±2.1 | 41.5±2.1 | *p < 0.001* | *p = 0.004* |
| | Atelectrauma | 12.6±1.0 | 15.6±1.7 | 15.3±4.3 | 16.7±4.6 | 17.1±4.2 | 17.4±4.1 | | |
| | | *p = 0.478* | *p = 0.483* | | | | | | |
| **PEEP [$cmH_2O$]** | Volutrauma | 8.0±0.0 | 8.0±0.0 | 32.4±2.2 | 32.4±2.2 | 32.0±2.0 | 32.0±2.0 | *p < 0.001* | *p = 0.219* |
| | Atelectrauma | 8.0±0.0 | 8.0±0.0 | 0.8±1.1 | 1.8±2.0 | 1.8±1.8 | 1.8±1.8 | | |
| | | *p = 1.000* | *p = 1.000* | | | | | | |
| **ΔP [$cmH_2O$]** | Volutrauma | 8.6±2.3 | 17.2±3.4 | 19.0±4.5 | 18.6±4.3 | 18.4±4.0 | 17.6±3.8 | *p = 0.003* | *p = 0.003* |
| | Atelectrauma | 10.0±3.0 | 19.0±6.1 | 26.8±5.3 | 28.2±5.4 | 29.4±4.9 | 30.2±4.2 | | |
| | | *p = 0.433* | *p = 0.291* | | | | *p = 0.001* | | |
| **$R_{rs}$ [$cmH_2O$/L/s]** | Volutrauma | 6.2±0.2 | 6.6±0.6 | 5.2±0.8 | 5.2±0.6 | 5.4±0.6 | 5.4±0.8 | *p = 0.003* | *p = 0.410* |
| | Atelectrauma | 7.0±0.4 | 7.1±1.1 | 10.4±4.2 | 10.3±5.5 | 11.7±5.5 | 12.6±3.5 | | |
| | | *p = 0.370* | *p = 0.378* | | | | | | |

| | | | | | | | | | |
|---|---|---|---|---|---|---|---|---|---|
| **$E_{rs}$ [$cmH_2O/L$]** | Volutrauma | 26.5±5.8 | 49.0±12.3 | 152.4±26.4 | 148.6±25.9 | 144.0±23.1 | 139.1±23.4 | *p < 0.001* | *p = 0.001* |
| | Atelectrauma | 29.4±2.8 | 55.1±8.4 | 237.8±49.7 | 242.8±51.1 | 255.9±40.3 | 261.7±36.3 | | |
| | | *p = 0.381* | *p = 0.385* | | | | | | |
| **%E2 [%]** | Volutrauma | 5.7±7.5 | 44.0±5.0 | 39.1±3.4 | 38.7±3.1 | 37.0±4.5 | 37.4±3.7 | *p = 0.003* | *p = 0.086* |
| | Atelectrauma | 7.9±8.2 | 38.6±10.1 | 21.2±15.9 | 18.5±16.6 | 13.5±8.1 | 2.3±8.7 | | |
| | | *p = 0.313* | *p = 0.324* | | | | | | |

*P-values indicate comparability of groups at specific time point. P-values are given below the respective columns. P-values of differences among groups after randomization are shown in column "group effect" and "time*group" effect.*

***Table A.5.3:*** *Mean and standard deviation of gas exchange and hemodynamics.*

| Variable | Group | Baseline 1 | Injury | Time 1 | Time 2 | Time 3 | Time 4 | *group effect* | *time*group effects* |
|---|---|---|---|---|---|---|---|---|---|
| ***Gas exchange*** | | | | | | | | | |
| **$PaO_2$ [mmHg]** | Volutrauma | 543.4±30.5 | 104.8±20.9 | 203.0±111.3 | 170.2±78.5 | 145.6±57.1 | 192.4±84.8 | *p = 0.360* | *p = 0.218* |
| | Atelectrauma | 556.8±52.7 | 107.8±33.1 | 106.0±100.1 | 130.0±113.8 | 132.8±99.1 | 124.4±73.6 | | |
| | | *p = 0.868* | *p = 0.869* | | | | | | |
| **$PaCO_2$ [mmHg]** | Volutrauma | 45.2±3.7 | 62.6±3.0 | 70.0±10.4 | 78.2±14.2 | 89.2±25.1 | 79.8±14.3 | *p = 0.073* | *p = 0.504* |
| | Atelectrauma | 40.4±4.3 | 67.8±15.9 | 57.4±10.2 | 59.8±12.5 | 62.6±10.3 | 62.2±10.7 | | |
| | | *p = 0.493* | *p = 0.501* | | | | | | |
| **pHa** | Volutrauma | 7.42±0.03 | 7.28±0.04 | 7.26±0.02 | 7.22±0.08 | 7.17±0.10 | 7.20±0.10 | *p = 0.102* | *p = 0.580* |
| | Atelectrauma | 7.46±0.03 | 7.26±0.09 | 7.34±0.07 | 7.33±0.11 | 7.31±0.12 | 7.32±0.12 | | |
| | | *p = 0.603* | *p = 0.601* | | | | | | |
| ***Hemodynamics*** | | | | | | | | | |
| **CO [L/min]** | Volutrauma | 4.3±1.2 | 4.8±1.3 | 5.9±0.6 | 6.1±0.8 | 5.6±0.6 | 5.2±0.8 | *p = 0.080* | *p = 0.759* |
| | Atelectrauma | 3.3±1.0 | 4.6±1.2 | 7.4±0.8 | 7.1±1.2 | 6.7±1.4 | 6.4±2.1 | | |
| | | *p = 0.839* | *p = 0.839* | | | | | | |
| **Mean arterial pressure [mmHg]** | Volutrauma | 93±18 | 90±12 | 91±11 | 82±31 | 85±14 | 81±12 | *p = 0.731* | *p = 0.922* |
| | Atelectrauma | 92±17 | 82±9 | 88±9 | 88±8 | 86±8 | 82±12 | | |
| | | *p = 0.315* | *p = 0.317* | | | | | | |
| **Mean pulmonary artery pressure [mmHg]** | Volutrauma | 26±6 | 34±2 | 43±5 | 44±3 | 44±5 | 44±6 | *p = 0.778* | *p = 0.111* |
| | Atelectrauma | 26±5 | 35±6 | 39±8 | 41±7 | 47±5 | 44±5 | | |
| | | *p = 0.885* | *p = 0.888* | | | | | | |

*P-values indicate comparability of groups at specific time point. P-values are given below the respective columns. P-values of differences among groups after randomization are shown in column "group effect" and "time*group" effect.*

**Anlage 1**

**Technische Universität Dresden**
**Medizinische Fakultät Carl Gustav Carus**
**Promotionsordnung vom 24. Juli 2011**

**Erklärungen zur Eröffnung des Promotionsverfahrens**

1. Hiermit versichere ich, dass ich die vorliegende Arbeit ohne unzulässige Hilfe Dritter und ohne Benutzung anderer als der angegebenen Hilfsmittel angefertigt habe; die aus fremden Quellen direkt oder indirekt übernommenen Gedanken sind als solche kenntlich gemacht.

2. Bei der Auswahl und Auswertung des Materials sowie bei der Herstellung des Manuskripts habe ich Unterstützungsleistungen von folgenden Personen erhalten:
Dr. med. Andreas Güldner, Prof. Dr. Marcelo Gama de Abreu, Dr. med. Lorenzo Ball, Dr. rer. medic. Liane Oehme, Dr. rer. medic. Michael Andreeff, Robert Huhle, Dr. rer. nat. Ines Rentzsch

3. Weitere Personen waren an der geistigen Herstellung der vorliegenden Arbeit nicht beteiligt. Insbesondere habe ich nicht die Hilfe eines kommerziellen Promotionsberaters in Anspruch genommen. Dritte haben von mir weder unmittelbar noch mittelbar geldwerte Leistungen für Arbeiten erhalten, die im Zusammenhang mit dem Inhalt der vorgelegten Dissertation stehen.

4. Die Arbeit wurde bisher weder im Inland noch im Ausland in gleicher oder ähnlicher Form einer anderen Prüfungsbehörde vorgelegt.

5. Die Inhalte dieser Dissertation wurden in folgender Form veröffentlicht:

**Original article:**
Critical Care Medicine: September 2016 - Volume 44 - Issue 9 - p e854–e865
Comparative Effects of Volutrauma and Atelectrauma on Lung Inflammation in Experimental Acute Respiratory Distress Syndrome.
Güldner A.*, Braune A.*, Ball L.*, Silva P.L., Samary C., Insorsi A., Huhle R., Rentzsch I., Becker C., Oehme L., Andreeff M., Vidal Melo M.F., et al. 2016.
** Dr. Güldner, Ms. Braune, and Dr. Ball equally contributed to this article.*

**Conference Contributions submitted and presented by Anja Braune:**

- Conference of the American Thoracic Society, May 2016, San Francisco, USA
  **Poster**: *"Distribution of regional lung perfusion in experimental ARDS: A comparison between ex-vivo fluorescence-labeled and in-vivo radionuclide-labeled microspheres"*
- 54. Jahrestagung der Deutschen Gesellschaft für Nuklearmedizin, April 2016, Dresden
  **Oral presentation**: *„PET/CT-Messung der regionalen, pulmonalen Inflammation, Belüftung und Perfusion im Rahmen einer tierexp. Forschung der Anästhesie"*
- 54. Jahrestagung der Deutschen Gesellschaft für Nuklearmedizin, April 2016, Dresden
  **Poster**: *„Vergleich von ex-vivo Perfusionsmessungen mittels Fluoreszenz-markierten Mikrosphären mit in-vivo Messungen mittels 68Ga-markierten Mikrosphären und PET/CT in geschädigten Schweinelungen"*
- Jahrestagung der Dt. Gesellschaft für Biomedizinische Technik, September 2015, Lübeck, Germany
  **Oral presentation**: *„Lung imaging for quantification of ventilator induced lung injury"*
- Deutscher Anästhesiecongress, May 2015, Dusseldorf, Germany
  **Poster**: *„Vergleichsanalyze von regionalen, pulmonalen Perfusionsmessungen mittels 68Ga-markierten und Fluoreszenz-markierten Mikrosphären im tierexperimentellen Modell des ARDS"*
- Conference of the American Thoracic Society, May 2014, San Diego, USA
  **Poster**: *"Comparative Analysis Of 68Ga-Labeled And Fluorescence-Labeled Microspheres For Assessment Of Pulmonary Blood Flow Distribution"*
- Deutscher Anästhesiecongress, May 2014, Leipzig, Germany
  **Oral presentation**: *„Quantifizierung der Effekte von Volutrauma und Atelektrauma auf die Verteilung der regionalen pulmonalen neutrophilischen Inflammation am Schwein mittels F-18-FDG-PET/CT Scans"*
- 29. Wissenschaftliche Arbeitstage der DGAI, February 2014, Würzburg, Germany
  **Oral presentation**: *„Quantifizierung der regionalen pulmonalen neutrophilischen Inflammation mittels Positronenemissionstomographie während Volutrauma und Atelektrauma am Schwein"*
- Conference of American Thoracic Society, May 2013, Philadelphia, USA
  **Poster**: *"Measurement of regional lung perfusion using 68Ga labelled- and fluorescence labelled- microshperes in experimental lung injury: A comparative analyzis"*
- Deutscher Anästhesiecongress, May 2013, Nürnberg, Germany
  ***Poster***: *„Vergleichsanalyze der Bestimmung von regionaler relativer Perfusion mittels 68Ga markierten- und Fluoreszenz-markierten Mikrosphären im experimentellen Lungenversagen am Schwein"*

6. Ich bestätige, dass es keine zurückliegenden erfolglosen Promotionsverfahren gab.

7. Ich bestätige, dass ich die Promotionsordnung der Medizinischen Fakultät der Technischen Universität Dresden anerkenne.

8. Ich habe die Zitierrichtlinien für Dissertationen an der Medizinischen Fakultät der Technischen Universität Dresden zur Kenntnis genommen und befolgt.

Dresden, 12. Juni 2017

Anja Braune

**Anlage 2**

**Hiermit bestätige ich die Einhaltung der folgenden aktuellen gesetzlichen Vorgaben im Rahmen meiner Dissertation**

das zustimmende Votum der Ethikkommission bei Klinischen Studien, epidemiologischen Untersuchungen mit Personenbezug oder Sachverhalten, die das Medizinproduktegesetz betreffen
*Aktenzeichen der zuständigen Ethikkommission* ……

☒ die Einhaltung der Bestimmungen des Tierschutzgesetzes
Aktenzeichen der Genehmigungsbehörde zum *Vorhaben/zur Mitwirkung*

24-9168.11-1/2012-42
24-9168.11-1/2009-36

die Einhaltung des Gentechnikgesetzes
*Projektnummer* ……..…….…….

die Einhaltung von Datenschutzbestimmungen der Medizinischen Fakultät und des Universitätsklinikums Carl Gustav Carus.

Dresden, 12. Juni 2017

Anja Braune